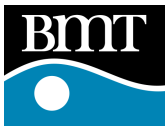

University of Southampton

Fluid Structure Interaction Research Group

Ship Science Report No 140

A Verification and Validation Study of the Application of Computational Fluid Dynamics to the Modelling of Lateral Sloshing

Bernhard Godderidge[1]

Mingyi Tan[1]

Stephen Turnock[1]

Chris Earl[2]

[1]University of Southampton

[2] BMT SeaTech

Southampton, 31 August 2006

Abstract

An understanding of liquid sloshing is of primary concern to the design and operation of Liquefied Natural Gas (LNG) carriers. Safe operation of LNG carriers requires the knowledge of global and local pressures imposed by the sloshing liquid. The most general method available to quantify such sloshing loads is the solution of the Navier Stokes system of equations using Computational Fluid Dynamics (CFD). Given the wide variety of modelling options available, as yet there is no consensus on the best modelling practice for such sloshing flows.

This report seeks to address this issue, examining various models and identifying the most suitable combination. The work uses the commercial CFD code ANSYS^{TM} CFX-10.0^{TM} but most of the findings are also relevant for similar other commercial codes. The physics of the sloshing problem are considered in order to identify the key modelling aspects. The correct application of CFD and how it can be used to model sloshing is considered. A suitable experimental dataset is described for use as a validation test case. The sloshing problem simulated is in a 1.2 m long and 0.6 m high tank with a 60 % filling level; excited at 95% of the first natural frequency with a maximum displacement of 1.25 % of the tank length.

A space and time discretisation independence study is carried out to ascertain the applicability of the results. Subsequently, the effect of including either a $k - \epsilon$ or Reynolds stress turbulence model as opposed to forcing laminar flow is examined. The choice of fluid (water and air) compressibility is investigated to determine its effects on model accuracy as well as the associated computational cost. Results are compared to experimental data and a computational reference case.

It is found that a grid of 6000-7000 elements with an initial node wall offset of 1 mm is sufficient to achieve effective grid independence for sloshing in . The necessary time discretisaton scheme was determined to be second order with a dynamic timestep adaptation scheme controlled by a root mean square Courant Number of 0.2. The flow regime should be considered

as turbulent and the standard $k - \epsilon$ turbulence model is suitable. Finally it is observed that a compressible-incompressible model combination for air and water respectively gives a near identical result to a fully compressible model with a 20% reduction in computational time.

Acknowledgments

This work was carried out under the auspices of the Engineering Doctorate scheme at the University of Southampton with industrial sponsorship and support provided by BMT SeaTech Ltd.

The authors are grateful to Dr M Hinatsu of the National Maritime Research Institute of Japan for providing the detailed information about the sloshing experiment used for validating the computational results.

Table of Contents

List of Figures

List of Tables

1 Introduction

1.1 Overview

Sloshing poses a significant design challenge for numerous applications in the aerospace, automotive and marine fields. Ships with large ballast tanks and liquid bulk cargo carriers (e.g. oil tankers) are subjected to often significant sloshing loads during their operational life. The inclusion of structural members in the tanks dampens the sloshing liquid sufficiently in all but the most severe cases. Liquefied Natural Gas (LNG) carriers cannot use this approach and sloshing has thus evolved into a central design problem for this type of vessel. Attempts to model the problem in a fluid dynamics context can be traced back to *Hydrodynamics* by Sir Horace Lamb [1], first published in 1879. As modelling capabilities improved, previously experimental methods were incorporated in the design environment. The advent of Computational Fluid Dynamics (CFD) resulted in a third approach in addition to fundamental analysis and model scale experimentation for the evaluation of sloshing flows.

This report considers the suitability of a commercial Navier Stokes Computational Fluid Dynamics package for the simulation of lateral sloshing. As CFD is a relatively new method of simulating fluid dynamics problems, there is as yet no consensus as to the most suitable approach. Given the assortment of possible solution strategies available, it is necessary to study the influence of user choice on the accuracy of the obtained solution. This report seeks to establish the significance of model-specific computational parameters and develop guidelines for future CFD sloshing models. Computational solutions are compared to experimental data given by Hinatsu [2]. In this study the following are investigated:

- grid (mesh) independence,
- time marching schemes and their dynamic control,
- turbulence models,
- compressibility effects and
- global conservation.

Each of the above will be subjected to methodical variation and an error analysis is carried out subsequently. Thus appropriate modelling approximations giving the best accuracy with the least computational cost can be identified.

1.2 Liquefied Natural Gas (LNG) Shipping

Natural gas[1] has become a more popular solution to satisfy the world's energy needs, the requirements for gas shipping have similarly increased. While a large amount of gas is transported by pipeline, Liquefied Natural Gas (LNG) shipping is more cost effective over transoceanic distances [4]. In addition, LNG shipping is not as much at the mercy of pipeline host nations. The transportation of LNG by ship has its origins in the 1950s with the *Methane Pioneer* being the world's first LNG tanker [5]. Tanker size has progressed significantly from the 5000 m^3 capacity of the *Methane Pioneer* to today's LNG tankers with capacities in excess of 160 000 m^3. The *qmax* LNG tanker, built for the Qatar III LNG project, has a capacity of 266 000 m^3 [6].

When natural gas is liquefied, the specific volume decreases by a factor of 600 [3], making gas transport by ship economically attractive. As the liquefication temperature of natural gas is approximately $-163°$ C, the LNG cannot be stored in normal cargo tanks. LNG tanks, made of Invar[2] or aluminium are enclosed in up to 1.5 m of insulation to protect the ship from the extremely low temperatures of its cargo. There are two main types of cargo tanks in use today.

1. Moss-Rosenberg (or Spherical) tanks, which are insulated aluminium spheres supported by the ship structure. Figure 1.1 shows the arrangement of a Moss-Rosenberg tank. The loads exerted on the ship by the Moss-Rosenberg design are simple to calculate, but the space within the hull is not used very efficiently [7].

2. Membrane Tanks, with the main types being the Technigaz Mk III and the Gaz Trans-

[1]Natural gas consists of typically 90 % Methane with approximately 9% ethane and the remaining 1% consisting of other gases. The precisie composition depends on the origin of the gas [3]

[2]Invar is a steel with a 36 % Nickel content, giving it superior low-temperature characteristics compared to most other structural materials. Normal steels become brittle at the low temperatures LNG is transported and are thus unsuitable for an LNG tank [3].

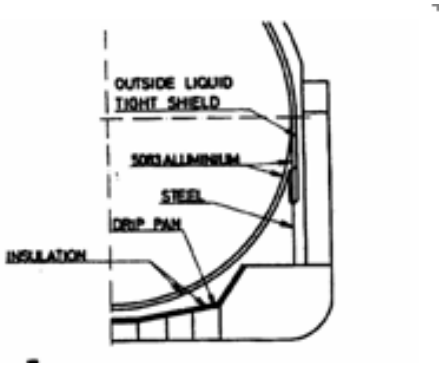

Figure 1.1: Moss Rosenberg LNG tank schematic [7]

port GT 96 design. Membrane tanks use the hull space far more efficiently as the inner hull is lined with insulation material and the tank wall, reducing the additional tank structural weight as well [7]. Figure 1.2 shows the arrangement of a typical membrane tank. However, the fluid sloshing loads are more complicated to calculated as the tank is a three-dimensional shape.

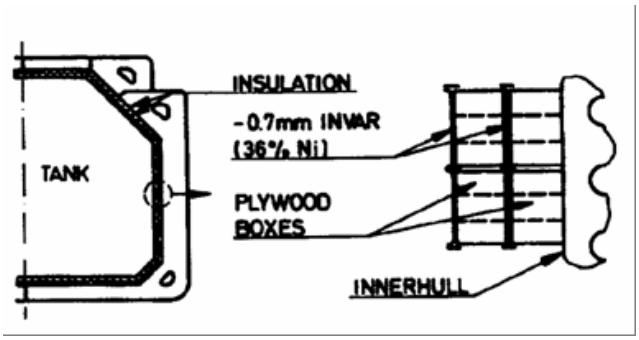

Figure 1.2: Membrane LNG tank schematic [7]

Figure 1.3 shows the general arrangement of a typical LNG membrane tanker, a design accounting for the majority of LNG tanker newbuilds.

Most membrane LNG tankers typically have five tanks instead of the four shown in figure 1.3. Several variants of the membrane design are established, with shipyards starting to introduce their own designs to avoid paying royalties to established designers. As some heat transfer between the tanks and the cargo is unavoidable, all LNG tanks contain natural gas in both liquid and gaseous states. This gives rise to a free surface in the tank, which when subjected to motions will result in sloshing. The tank filling level for most membrane tanks

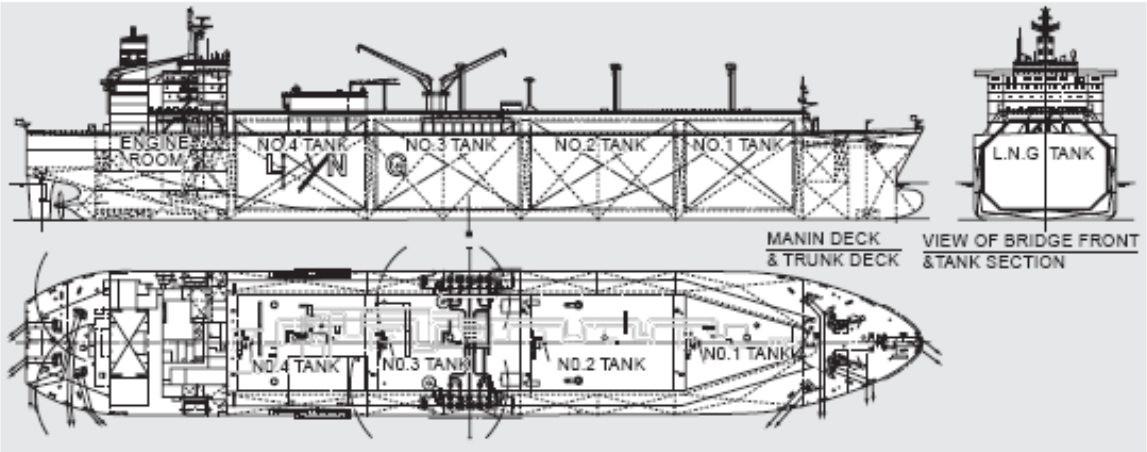

Figure 1.3: Arrangement of a membrane-type 137 000 m^3 Liquefied Natural Gas tanker (from Ishimaru *et al* [8]). Length is 276 m, beam 44 m, draught 12 m and deadweight 76 110 t. Typical speeds for LNG tankers are about 20 kts

is mandated by classification societies at below 10 % and above 90%, as the greater variation in filling levels permitted in the 1970s resulted in tank damage due to sloshing loads [9].

Following two decades of relatively slow growth since the LNG boom of the 1970s, the LNG market has benefited from greater investment in the last ten years. Royal Dutch Shell expects the LNG market to grow to the same size as the petroleum market by 2025 [10] as power generation and industry as well as households increase their reliance on natural gas. Recently commenced LNG projects in Qatar and Sakhalin require a considerable increase in LNG tanker availability and size. Moreover, in 2005 the Russian government gave a stark illustration of the weaknesses of pipelines when a quarrel with the Ukraine over piping fees escalated. Russia turned off the gas supply and consequently several Western European nations normally obtaining a large proportion of their gas supply from Russia were forced to compensate a near 30% supply shortfall [11]. Others, such as Spain, relying more heavily on LNG imports were able to deal with the supply impasse with less difficulty. Consequently, European energy policy has been adjusted to diversify gas supplies, implying an increased use of LNG shipping [12].

The current economic climate in the global gas market has thus precipitated two principal developments in the design of LNG carriers:

1. Increased Ship Size. The capacity of newbuild LNG carriers is set to increase in excess of 250 000 m^3. The LNG production & transport chains, commonly known as 'LNG trains', have increased in scale, requiring larger capacity vessels.

2. Flexible Filling Levels. This requirement is caused by a shift in the pattern of LNG trade. In the past, LNG ships were built for a certain LNG project with a fixed route. Today's gas market is considerably more flexible. Thus, energy companies seek to take advantage of local price variations. In fact Francisco Blanch of the brokerage Merrill Lynch has forecast a shortage of natural gas in the 2006/2007 Winter as Europe and the US compete for LNG supplies [13].

These developments have renewed interest in more detailed sloshing load assessments as well as real time information on actual sloshing loads imposed on the membrane tank walls.

1.3 Sloshing Load Assessment

Currently there are three distinct approaches available to assess sloshing loads. Arguably the oldest method is linear potential flow theory assuming small motion detailed by Graham and Rodriguez [14], with a useful summary given by Abramson [15]. The strength of this method is its simplicity, as it is possible to derive expressions for pressure, and hence wall force and tank turning moment, in terms of tank properties, acceleration and sloshing frequency. However, there are some considerable shortcomings. Firstly, the selection of potential flow may not be an accurate representation of the fluid. The assumption of small motions further restricts the range of validity of this approach. Finally, the more complex tank shapes found in membrane LNG carriers, unlike the cylindrical tank of a rocket, are not easily described using a standard coordinate system. This limitation can be overcome using the well known panel (boundary element) approach to discretise the more complex tank shapes.

In considering the shortcomings of linear theory as well as the development of more powerful computational resources, a non-linear theory was introduced by Faltinsen [16] and Abramson *et al* [15] to model sloshing loads more accurately over a wider range of motions. Non-linear theory continues to be developed, some recent examples include Faltinsen [17], a comprehensive review is given by Ibrahim in ref [18] and [19]. While non-linear theory overcomes some of

the limitations associated with linear theory, the inherent assumption of inviscid irrotational flow may not be sufficient for complex problems. Principally, potential theory does not permit the fragmentation and merging of fluids observed in violent sloshing flows.

Experimentation using scale models has become standard practice in the marine field. It is used, for example, by major classification societies such as Det Norske Veritas [20], Lloyd's Register [21] and the American Bureau of Shipping [22]. While experimentation gives reliable data at the experimental scale, the scaling procedures are far more contentious and less reliable [23] & [21]. As pointed out in the previous section 1.2, the size of LNG carriers has remained constant for some time. Hence there is no full scale data with which to calibrate the experimental results for the increase in tank volume required.

The advent of more powerful computers has given rise to the use of Computational Fluid Dynamics (CFD) to determine sloshing loads. The main commercial CFD packages are Star-CD, Fluent, Flow-3D and CFX. Fully viscous CFD is not subject to the same fluid modelling restrictions as potential flow. Thus, it is possible to include directly the effects of viscosity, compressibility as well as arbitrary tank shapes. However, CFD does not provide the flow solution in terms of any operational parameters such as acceleration or frequency. Thus, a large number of runs are required to fully assess the sloshing properties of a tank.

Unfortunately, no one method provides a reliable and accurate sloshing results in an acceptable timescale. Therefore, common practice is to use all three methods in conjunction with each other: simpler linear or nonlinear theory is used in the initial design phase to obtain a first estimate of the sloshing pressures involved. As a tank design is refined further, experimental and CFD studies are carried out to obtain more detailed information of the sloshing loads. It should be noted that while the above procedure is described for a design scenario, it can be applied to assess sloshing loads in the frequency domain when considering sloshing in a seakeeping context. However, this introduces further difficulties which are not within the context of this report.

1.4 Sloshing Dynamics

Even though the sloshing problem is challenging by itself, more detailed investigations need to consider the interaction between the sloshing fluid and the structure it is contained within. Sloshing has been addressed in this context recently by Gallarde *et al* [24] and Kim [25]. In mechanical engineering sloshing is considered coupled with the container motion when assessing vehicle dynamics, as carried out by Aston [26] and Kang [27]. As the experience with road tanker design indicates, it may be necessary to join sloshing and vehicle dynamics in one model when there is strong coupling between the motion of the tank and the sloshing fluid.

Figure 1.4(a) shows a schematic of the full sloshing problem: the ship is disturbed by the wave excitation E_{wave}, which in turn moves the tank resulting in sloshing. The sloshing and wave excitation forces act at the tank boundary. The traditional approach splits the system above into a pure sloshing problem shown in figure 1.4(b) and a seakeeping problem shown in figure 1.4(c). However, this approach does not take cross-coupling between ship motion and sloshing into account.

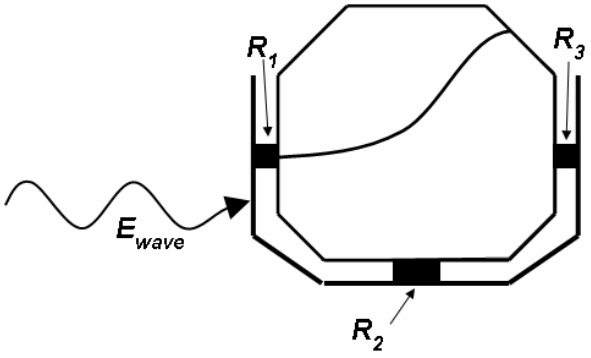

1.4(a): The full sloshing system

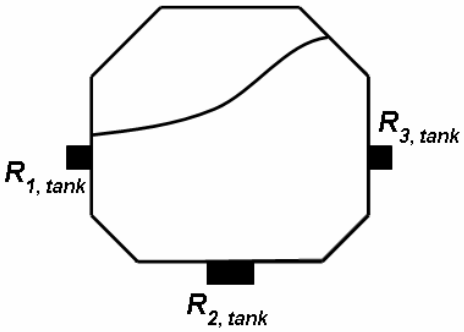

1.4(b): The sloshing problem

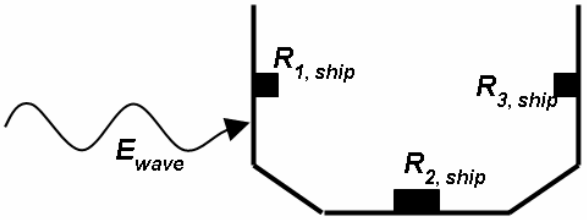

1.4(c): The seakeeping problem

Figure 1.4: The sloshing problem for LNG tankers

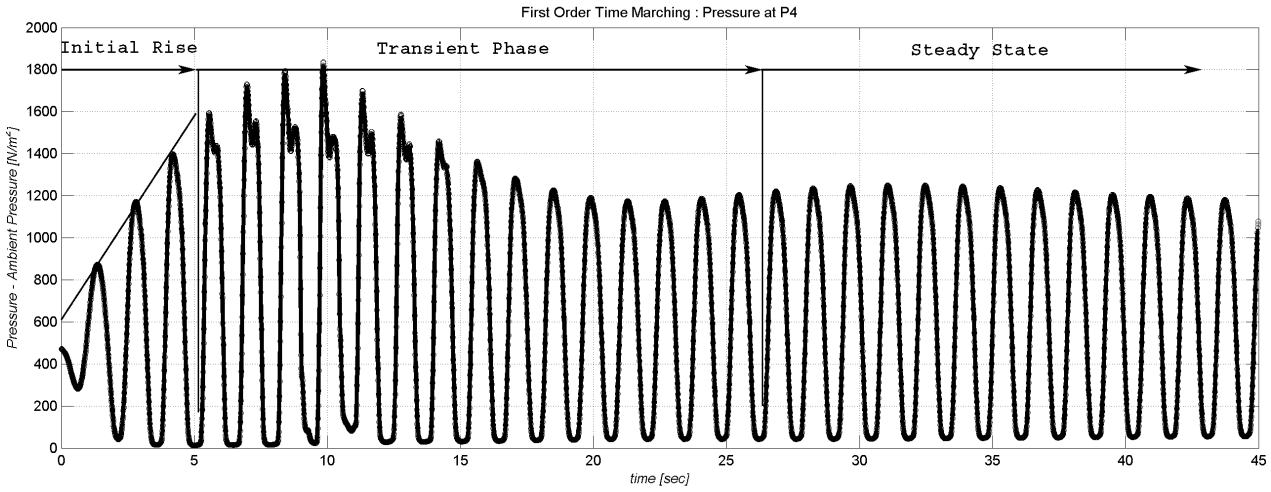

Figure 1.5: Transient and steady state sloshing response

A further complication is the transient nature of the sloshing flow. As can be seen in figure 1.5, an initial transient region is followed by the flow settling into a steady state. As LNG tankers rarely sail in regular seas, the sloshing load estimation procedure must take into account the irregular nature of the excitation force. The sloshing fluid will exert initial transient loads but the steady state data underestimates this load. Faltinsen *et al* [29] & [30] have studied this problem in considerable detail, observing up to five distinct transient phases. This has been confirmed by Landrini [31]. The transients became more pronounced, and a steady state solution takes longer to emerge as the tank excitation frequency approaches the natural sloshing frequency.

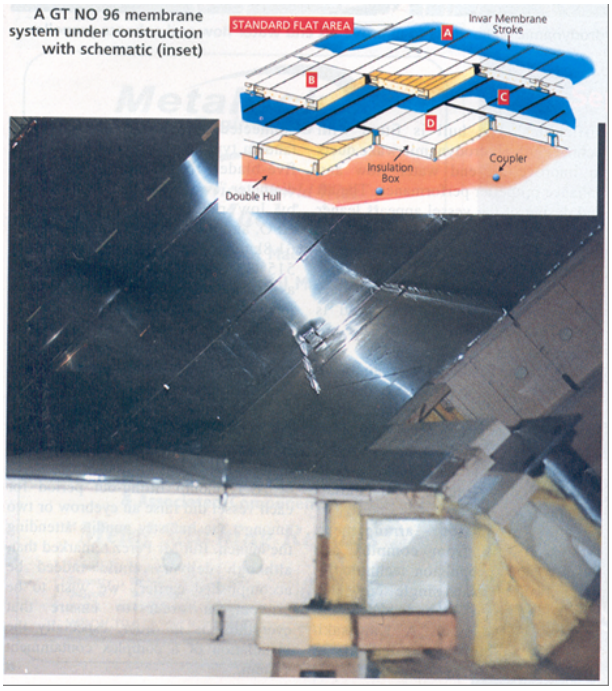

Figure 1.6: GT 96 membrane tank insulation [28]

Finally, the local interaction between fluid and tank structure is often considered separately [22], or neglected altogether. Especially membrane tanks, with multiple layers of insulation

with varying yield strength and structural support up to 1.5 m from the point of fluid impact (see figure 1.6) may be more susceptible to local deformation. Regardless of the modelling approaches described in section 1.3, the inclusion of structural considerations complicates the analysis and makes pressure scaling as well as assuring similarity in model tests significantly more complex. Fluid-structure interaction at this level of detail is achievable when coupling a CFD and a finite element code to obtain a solution [23], but increases the computational requirements further. Having briefly reviewed the sloshing system in a wider sense, section 2 will examine the physics of sloshing in more detail.

2 Physics of Sloshing

2.1 Sloshing Defined

A liquid with an unrestrained free surface may experience large displacements when excited by an external force [15]. This phenomenon is known as sloshing. Associated with the fluid motion are loads exerted on the containment vessel structure. Ships carrying liquid bulk cargo in partially filled tanks are subjected to sloshing loads, numerous cases of sloshing-induced damage have been identified in literature [9], [32] and [33]. The safety of a ship is readily compromised by a fluid sloshing uncontrollably, mandating a full assessment using the methods discussed in section 1.3 of the resultant structural loads as well as the impact on stability.

Before attempting to model a sloshing flow, the physics need to be identified to determine the key properties to be included in a mathematical model. The precise nature of the sloshing load is influenced by the tank geometry, fluid properties and the nature of the container excitation. The problem is complicated further if the interaction between the fluid and tank wall or mass transfer between the fluids are considered. This section gives an overview of the physics influencing the sloshing response of a liquid and hence points out the features to be included in a CFD model.

2.2 Sloshing Excitation

The significance of the sloshing excitation is best quantified using potential flow, as pressures and forces can be expressed in terms of the motion properties. A rectangular tank will be used as a representative example of a real LNG tank, potential flow is assumed as a fluid model. Analysis is then used to assess the effect of excitation amplitude and frequency on the sloshing load.

In the operational environment of a ship, the excitation will usually be of an irregular nature. However, Fourier analysis permits the decomposition of an irregular signal $e(t)$ into

a finite number of regular components as indicated in equation (2.1) below

$$e(t) = \sum_{n=0}^{\infty} \left[A_n \cos(nk\ t) + B_n \sin(nk\ t) \right], \tag{2.1}$$

where nk is the frequency of each component and A_n and B_n the corresponding amplitudes. The identification of the predominant modes then simplifies the analysis considerably. Olsen [34] identifies three main slosh modes.

1. Lateral sloshing, the most important kind of sloshing. It is generated by both lateral and angular tank movements.

2. Swirling, or rotational sloshing is a fully three dimensional phenomenon. Its occurrence depends on the tank shape as well as the motion. Simultaneous excitation of the fluid in orthogonal planes, such as surge and sway, will readily result in swirling.

3. Vertical sloshing can result in standing waves, but this is unlikely to occur in ship tanks. Rather, vertical sloshing tends to increase lateral sloshing loads.

2.2.1 Excitation Amplitude

The motion of a ship in a seaway is usually measured in terms of acceleration [35]. Newton's second law can, with certain restrictions, provide a relationship between applied force and acceleration. However at the global scale, that is considering the sloshing fluid as a lumped mass, this is insufficient to completely characterise the sloshing flow. Using linear potential flow and limiting the analysis to small displacements is a better approach. It can be shown that the pressure force of lateral two-dimensional liquid with density ρ sloshing in a rectangular container with length a in the sloshing direction, width b and filling level h is

$$\frac{F}{\rho g h a b} = \overbrace{\ddot{x}(t)}^{acceleration} \frac{1}{g} \left[1 + \sum_{n=0}^{\infty} \frac{\overbrace{8 \tanh\left\{(2n+1)\,\pi \frac{h}{a}\right\}}^{tank\ geometry\ \&\ filling\ level}}{\pi^3 (2n+1)^3 \frac{h}{a}} \frac{\overbrace{1}^{excitation\ frequency}}{\left(\frac{\omega_n}{\omega}\right)^2 - 1} \right], \tag{2.2}$$

where g is gravity, ω excitation frequency, ω_n the natural sloshing frequency defined in equation (2.4) and $\ddot{x}(t)$ an acceleration applied to the tank. It is apparent that sloshing pressure and hence force are directly related to acceleration.

When scaling sloshing loads, acceleration is used as a primary parameter [15] & [36]. However, once the flow becomes sufficiently violent so that the small displacement condition is violated, the direct correlation between acceleration and pressure breaks down. Local phenomena determine the pressure peaks which exist for very small timescales only, as shown in subsequent sections of this report.

2.2.2 Excitation Frequency

The influence of excitation frequency may be determined in a similar manner. Using the linear potential flow relation in equation (2.2) above one finds that

$$F_p \propto p \propto \frac{1}{\left(\frac{\omega_n}{\omega}\right)^2 - 1}, \tag{2.3}$$

where F_p is the pressure force, p the pressure, ω the excitation frequency, and the first ($n = 0$) natural frequency ω_n is given as

$$\omega_n^2 = \frac{\pi g}{a} \tanh\left(\pi \frac{h}{a}\right). \tag{2.4}$$

In the above expression, a is the tank length in the sloshing direction, g the gravitational constant and h is the filling level. Clearly, at $\omega = \omega_n$ equation (2.3) is singular, resulting in an unphysical, infinite force. While this limitation is overcome in the more complex nonlinear theory, the frequency dependency of sloshing is illustrated well. However, Faltinsen *et al* [37], [29] and [30] have found that the behaviour of the sloshing fluid becomes more irregular as the excitation frequency approaches the natural sloshing frequency.

Olsen [38] considers the first (lowest) natural frequency to be the most important for modelling. However, Faltinsen, using a modal approach, determined that higher modes can be influential on the time history as well [30]. As a CFD solution requires the explicit specification of a regular, or irregular excitation frequency, this is not an immediate concern. In a design environment, however, this may complicate the assessment of the sloshing properties considerably as more than one natural frequency needs to be taken into account when simulating the worst-case scenario.

2.3 Fluid Properties

The nature of the fluids in the sloshing tank determines the sloshing response as well. While most experimentation uses water and air with clearly defined properties, liquefied natural gas (LNG) is not a pure substance and the precise composition depends on the origin of the gas. Mann [3] gives a representative breakdown using Algerian Arzew LNG as 87-90% methane, 8-9% ethane and 0.5 to 1% nitrogen. Other component gases include propane, butane and isobutane, which account for less than 0.5% of the total. When approximating the properties of LNG with those of pure methane, any results need to be treated with caution as inaccuracies of up to 20 % have been reported [3]. Mann recommends the use of a rule of mixture model when greater accuracy is required. As the sloshing problem addressed as part of this study involves water rather than LNG, precise values for LNG properties are not required. However, as the behaviour of methane can be indicative of LNG, methane properties are often used in this section.

2.3.1 Viscosity

The influence of viscosity on a sloshing flow remains contentious. Faltinsen and Rognebakke [39] found that viscosity was especially important for small excitation amplitudes and high filling levels. Bass *et al* [36] state that

> ...viscous effects are secondary in the scaling of large amplitude nonlinear sloshing impact pressures.

This is confirmed by Olsen [38]. The Reynolds number

$$R_n = \frac{VL}{\nu}, \tag{2.5}$$

where V is a characteristic velocity, L a characteristic length and ν kinematic viscosity, characterizes viscous flows. Bass *et al* [36] give typical full scale sloshing, with a tank length of about 40 m and typical LNG viscosity [3] Reynolds Number as 10^9. Figure 2.1 shows the viscosity-temperature curves for methane, the primary constituent gas of LNG. A typical value for dynamic viscosity μ for liquefied methane is given by $12.4 \cdot 10^{-5}$N s/m^2. A comparison of LNG and water properties, along with a summary of common non dimensional coefficients describing the sloshing flow are given in section 2.3.4. The dynamic viscosity and density

change rapidly near the boiling temperature of 112 K, but once the methane has turned liquid, the slopes of viscosity and density are similar, indicating that the kinematic viscosity ν does not vary significantly in the temperature region of interest of below 110 K.

While the peak pressure does not appear to depend directly on fluid viscosity, the same cannot be said for the time evolution of the impact pressure. Preliminary studies using a collapsing water column with varying dynamic viscosity μ carried out at the initial stages of this project found that while the peak load remained fairly constant, the shape of the pressure peak was considerably sharper once the viscosity was decreased. Increased dynamic viscous fluid resulted in a prolonged pressure peak.

CFD Modelling Implications:
As the dynamic viscosity of Methane, the primary constituent gas of LNG, remains constant over a likely range of temperatures and pressures encountered during sloshing, the effect of flow-dependent viscosity is not included in the current study. However, the fluid model should reflect the influence of viscosity in the sloshing motion as time-dependent flow features tend to influence the flow evolution.

2.3.2 Compressibility

Fluid compressibility has been found to be more significant in the ullage gas than for the denser liquid phase. Figure 2.3 shows the speed of sound of methane. Note the rapid change at the liquefication temperature. The speed of sound for liquid methane of approximately 1320 m/s, is similar to the 1500 m/s observed in water. Once the methane is in its gaseous state the speed of sound is about 300 m/s, less than the speed of sound of air. This gives rise to a number of phenomena not expected when considering the gas as incompressible.

- The gas delays the impact pressure peak if located between the tank wall and sloshing liquid. This spreads the impact over a longer timescale, causing prolonged loading to the containing structure.

- As the sloshing is increasingly violent, the gaseous phase will become partially absorbed in the liquid phase. Provided the impact pressures are high enough, this will result in

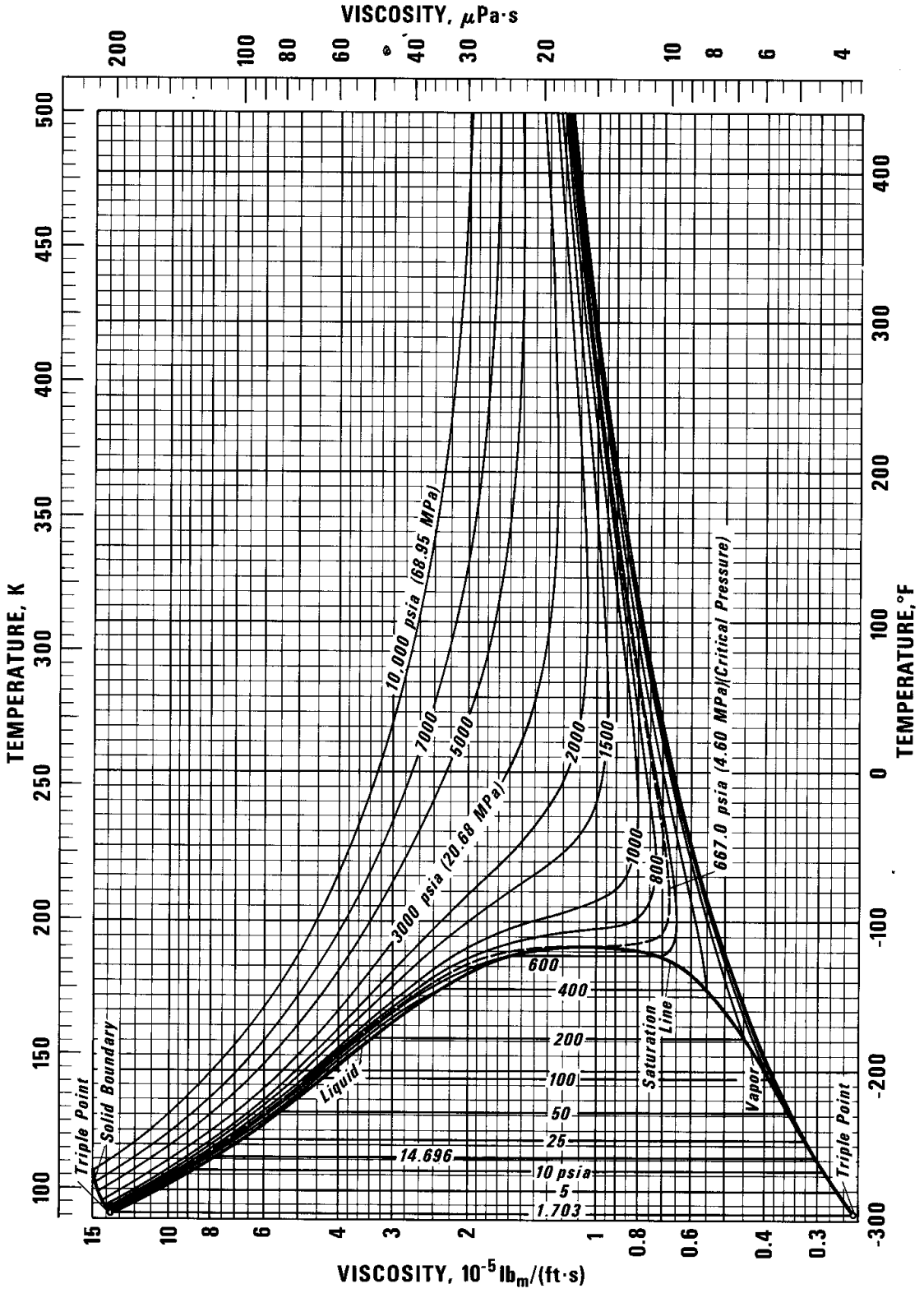

Figure 2.1: Methane viscosity-temperature curve [3]. Note that the transportation temperature of LNG, −163° C corresponds to ≈ 110 K. Indicated pressures include the atmospheric pressure, 1 atm corresponds to 14.696 psia

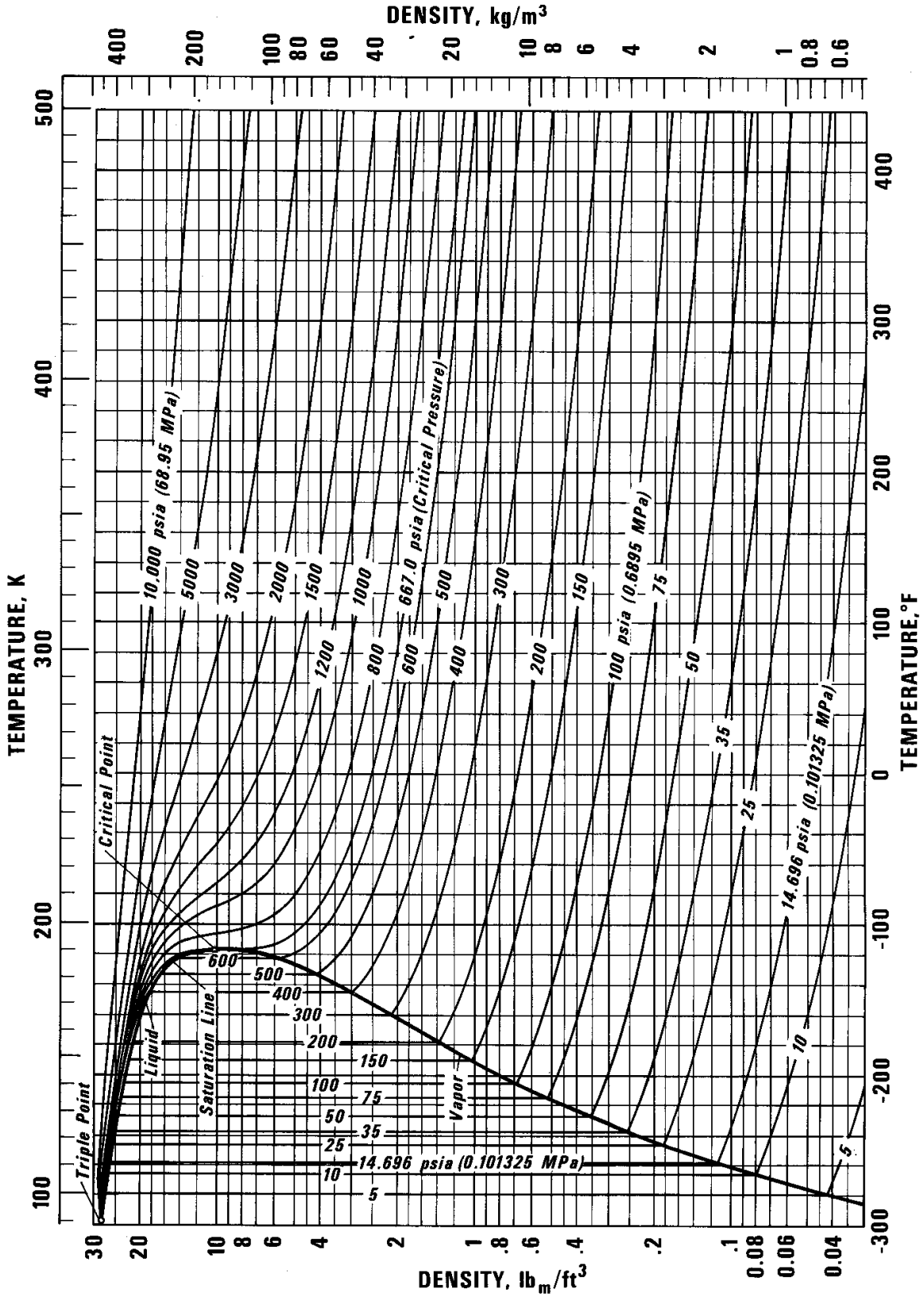

Figure 2.2: Methane density-temperature curve [3]. Note that the transportation temperature of LNG, $-163°$ C corresponds to ≈ 110 K. Indicated pressures include the atmospheric pressure, 1 atm corresponds to 14.696 psia

cavitation [9]. The subsequent collapse of cavitation, especially over longer durations, can cause severe damage to the containment structure.

CFD Modelling Implications:

The model will need to identify the onset of cavitation. As high fluid pressure is a prerequisite, a suitable threshold pressure needs to be determined. In addition, the pressure distribution on the wall must be modelled with sufficient accuracy to capture local pressure peaks. Olsen [38] reports that compressibility influences both scaling of experimental data as well as the sloshing response. Thus a compressible fluid model may be required to capture key flow features.

2.3.3 Ullage Gas Pressure

Corrignan [40] and Olsen [38] assign the ullage pressure significant influence on sloshing pressure and consequent force. Experiments referred to by Bass *et al* [41] as well as computational studies carried out by the author confirm that a lower ullage pressure will result in a higher impact pressures. The implications are more germane to the scaling of experimental data, as mathematical models generally consider the full scale problem.

CFD Modelling Implications:

LNG is carried at atmospheric pressure, thus eliminating any ambiguities when deciding the correct ambient pressure. As full-scale tanks are of interest, there is no need to scale the ullage gas pressure to maintain similitude. From an operational point of view, increasing the ullage gas pressure may alleviate sloshing to some extent, although the liquefaction temperature would be lower. From a design point of view this will be investigated further.

2.3.4 Flow Description

The following section lists some pertinent dimensionless parameters used to describe the sloshing flow. Results are given for the experiment and the corresponding CFD simulation carried out, a typical sloshing experiment used for LNG tank design and a sloshing flow in a full scale LNG tank. Note that in the latter cases some quantities are indicative only. The majority of formulations in this section has been obtained from Ibrahim [18]. Subscripts

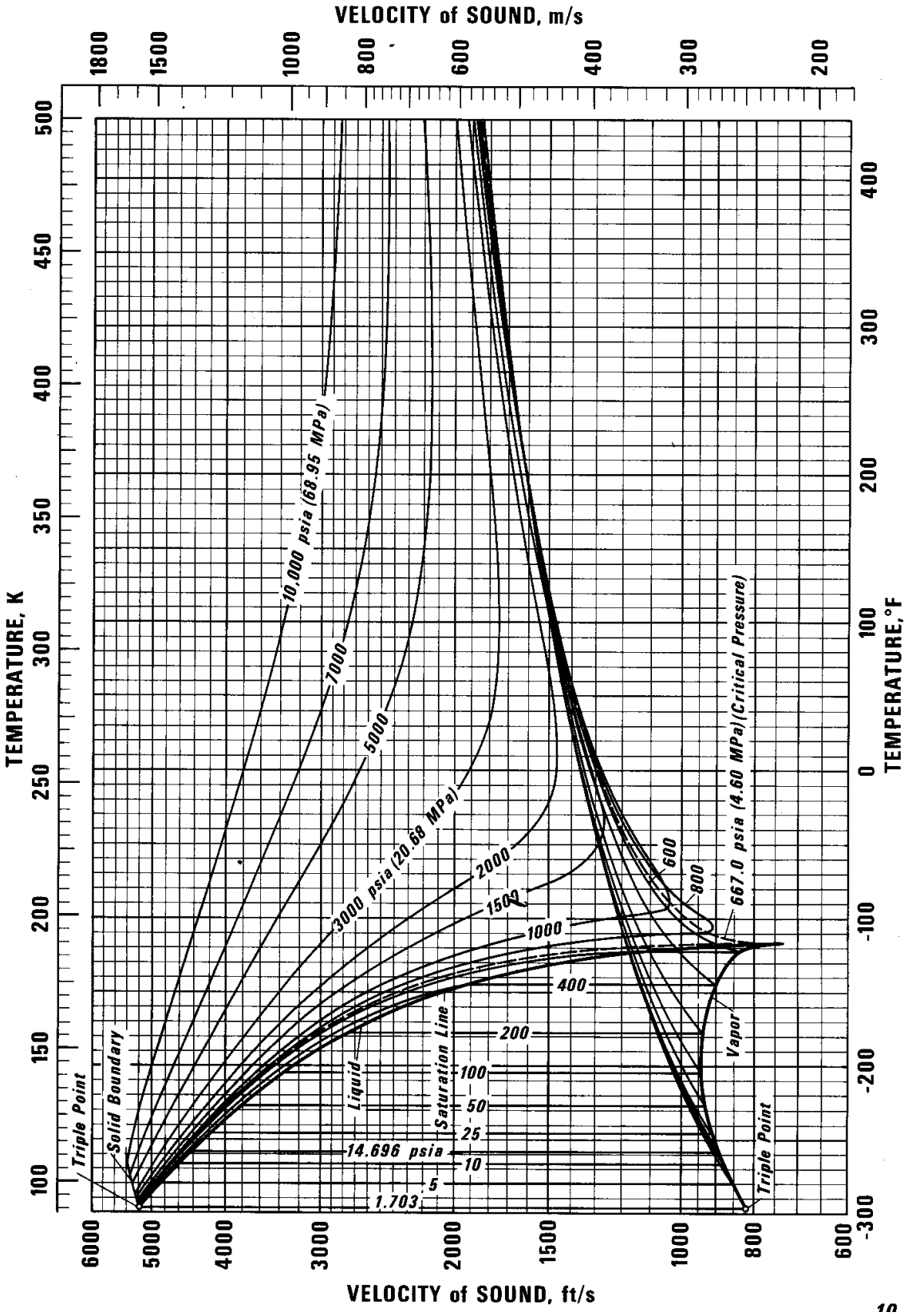

Figure 2.3: Methane viscosity-temperature curve [3]. Note that the transportation temperature of LNG, −163° C corresponds to ≈ 110 K. Indicated pressures include the atmospheric pressure, 1 atm corresponds to 14.696 psia

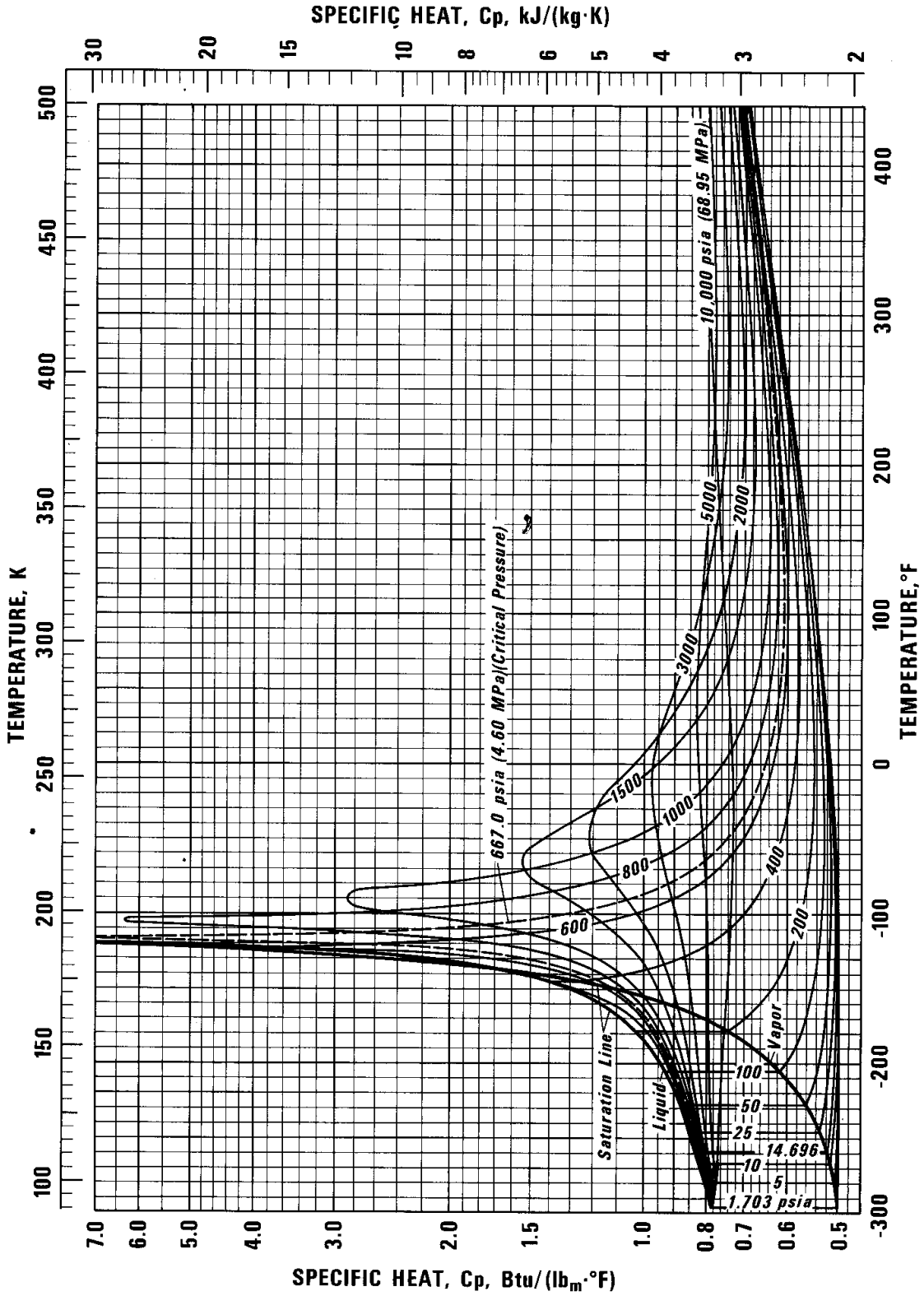

Figure 2.4: Methane specific heat (at constant pressure)-temperature curve [3]. Note that the transportation temperature of LNG, $-163°$ C corresponds to $\approx$ 110 K. Indicated pressures include the atmospheric pressure, 1 atm corresponds to 14.696 psia

indicate the fluid used, $_w$ indicates water, while $_{LNG}$ indicates LNG where the properties of a parameter ϕ are computed as $0.9\phi_{Methane} + 0.1\phi_{Ethane}$.

Bond Number The Bond number Bo compares gravitational and surface tension forces. It is defined as

$$Bo = \frac{\rho g L^2}{\sigma}, \tag{2.6}$$

where ρ is density, g gravity, L characteristic length and σ surface tension. It is useful as it indicates the importance of surface tension relative to the acceleration experienced by the sloshing tank. While in all dimensionless parameters gravity is taken as 9.81 m/s, another method would be to use the sloshing acceleration. LNG data for surface tension was obtained

Table 2.1: Bond number for the current experiment, a typical experiment for LNG tank design and full scale sloshing

Name	Experiment	LNG Experiment	LNG Full Scale
Bond Number	$0.194 \cdot 10^6$	$0.539 \cdot 10^6$	$699 \cdot 10^6$
Density ρ [kg/m^3]	1000	1000	470
Gravity g [m/s^2]	9.81	9.81	9.81
Length L [m]	1.2	2.0	50.0
Surface tension σ [N/m]	0.0728	0.0728	0.0165

from ref [42], 1 dyne = 10^{-5} N.

Froude Number The Froude number,

$$Fn = \frac{V}{\sqrt{gL}}, \tag{2.7}$$

is well known in naval architecture. In equation (2.7), V is a characteristic velocity. Most sloshing experiments are scaled on a Froude basis, giving this parameter additional importance. The characteristic velocity is taken as the maximum velocity of the sloshing container, which for an LNG tanker is taken to be 5 m/s. No data for typical LNG tank experimentation was available, the experimental velocity was scaled using the relation $V_{exp} = V_{LNG} \cdot (L_{exp}/L_{LNG})^{0.5}$.

Table 2.2: Froude number for the current experiment, a typical experiment for LNG tank design and full scale sloshing

Name	Experiment	LNG Experiment	LNG Full Scale
Froude Number	0.021	0.051	0.0045
Velocity V [m/s]	0.06	1*	5
Gravity g [m/s^2]	9.81	9.81	9.81
Length L [m]	1.2	2.0	50.0

Grashof Number The Grashof number relates bouyancy to viscous forces as

$$Gr = \frac{\beta g L^3 \Delta T}{\nu^2}, \tag{2.8}$$

with β, the volumetric thermal expansion coefficient, defined as

$$\beta = -\frac{1}{\rho}\frac{\partial \rho}{\partial T}. \tag{2.9}$$

T is the temperature in Kelvin and ν kinematic viscosity.

Table 2.3: Grashof number for the current experiment, a typical experiment for LNG tank design and full scale sloshing. *no numerical information was found in literature for β_{LNG}, so it was obtained using the slope of the density-temperature plot (see figure 2.2) at 110 K

Name	Experiment	LNG Experiment	LNG Full Scale
Grashof Number	$3.52 \cdot 10^8$	$1.63 \cdot 10^9$	$2.88 \cdot 10^{16}$
Thermal Expansion Coefficient β [1/K]	$210 \cdot 10^{-6}$	$210 \cdot 10^{-6}$	0.02*
Gravity g [m/s^2]	9.81	9.81	9.81
Length L [m]	1.2	2.0	50.0
ΔT [K]	0.1	0.1	2
Kinematic Viscosity ν [m^2/s]	$1.01 \cdot 10^{-6}$	$1.01 \cdot 10^{-6}$	$1.6 \cdot 10^{-6}$

Reynolds Number The Reynolds number is a key dimensionless parameter in fluid dynamics. It is given as

$$Rn = \frac{LV}{\nu}, \tag{2.10}$$

relating inertial and viscous forces. Here it serves as an indicator as to the importance of the inclusion of viscosity in a mathematical model. Other uses include determining the onset of turbulence, which is addressed in a later chapter. Bass [36] introduces a Froude-modified Reynolds number given as $Re_{Froude} = \rho g^{1/2} L^{3/2} \mu^{-1}$. In this case the Reynolds number defined in equation (2.10) above is used, however.

Table 2.4: Reynolds number for the current experiment, a typical experiment for LNG tank design and full scale sloshing. *Bass [36] quotes $2 \cdot 10^9$ as a Froude-modified Reynolds number.

Name	**Experiment**	**LNG Experiment**	**LNG Full Scale**
Reynolds Number	$7.16 \cdot 10^4$	$1.99 \cdot 10^6$	$1.56 \cdot 10^{8*}$
Length L [m]	1.2	2.0	50.0
Kinematic Viscosity ν [m^2/s]	$1.01 \cdot 10^{-6}$	$1.01 \cdot 10^{-6}$	$1.60 \cdot 10^{-6}$
Velocity V [m/s]	0.06	1	5.0

Strouhal Number The Strouhal number, given as

$$St = \frac{\omega L}{V}, \tag{2.11}$$

is used to analyse unsteady fluid dynamics problems. It is a measure of inertial forces induced by the unsteadiness of the flow. Considering the nature of the sloshing flow, the Strouhal number is a useful description.

Table 2.5: Strouhal number for the current experiment, a typical experiment for LNG tank design and full scale sloshing. *assumes a 10 second excitation period. *No meaningful LNG design experimental data available*

Name	**Experiment**	**LNG Full Scale**
Strouhal Number	14.24	1.00
Length L [m]	1.2	50
Characteristic oscillation frequency [rad/s]	0.712	0.1*
Velocity V [m/s]	0.06	5

Weber Number The Weber number relates surface tension and inertia forces, given as

$$We = \frac{\rho L V^2}{\sigma}, \tag{2.12}$$

indicates whether surface tension should be included in the computational model. Note that

Table 2.6: Weber number for the current experiment, a typical experiment for LNG tank design and full scale sloshing

Name	Experiment	LNG Experiment	LNG Full Scale
Weber Number	$5.93 \cdot 10^1$	$2.75 \cdot 10^4$	$3.56 \cdot 10^7$
Density ρ [kg/m^3]	1000	1000	470
Length L [m]	1.2	2.0	50.0
Surface tension σ [N/m]	0.0728	0.0728	0.0165
Velocity V [m/s]	0.06	1	5

the experimental Weber number is considerably lower than at full scale, indicating further experimental inaccuracies. For full-scale sloshing, the inertial forces are dominant. As surface tension may be related to the curvature to the free surface using linear potential flow, the significance of surface tension can be established once computational results are available.

2.4 Fluid Container

2.4.1 Filling Level

The filling level influences the natural frequency of sloshing given in equation (2.4) as well as the static pressure. As the typical boil-off rate for an LNG tanker is about 0.1% per day [43], a 21 day journey will have resulted in approximately 2% of the cargo boiling off. Due to the hopper space at the top of membrane tanks, and especially for the geometry of spherical LNG tanks, this will result in more significant reduction in filling level h. For a typical membrane LNG tank specified by [44] this would drop the filling level by 0.5 m - 0.6 m corrseponding to 3% of the total tank height.

CFD Modelling Implications:

As the filling level determines both the sloshing natural frequency and the inertia of the

system, the model must be able to represent the precise amount of primary fluid in the system. Finite volume CFD is well suited for this requirement, since numerical diffusion of mass and momentum should be so small as not to influence the result.

2.4.2 Flexible Tank Wall

The interaction between the tank structure and the impacting fluid is neglected in most sloshing analyses or split from the procedure determining the sloshing impact pressure [22]. As this problem is quite complex to consider in a unified mathematical model [45], no solution analogous to the linear sloshing model proposed by Abramson [15] or the more sophisticated nonlinear analysis by Faltinsen [46] exists. There have been no experimental or computational studies to date assessing the significance of hydroelasticity when determining sloshing impact loads for LNG tank sloshing. However, this is one area to be explored as part of this project.

3 Computational Fluid Dynamics

3.1 Introduction

Fluid dynamics has provided some of the most complex problems in engineering, especially when coupled with other fields such as structures or thermodynamics. Fortunately, a number of solution methods, outlined in section 1.3, are available to quantify the flows. One particular method is Computational Fluid Dynamics (CFD). This method is primarily associated with, but not limited to, the iterative solution of viscous flows. CFD has turned into a practical design tool with the advent of powerful computers. Still, CFD is often considered the sledge-hammer approach to solving fluid dynamics problems, and results tend to be deceptive due to colourful postprocessing.

As increased reliance is placed on CFD results in industry, it is vital to ensure the results are appropriate for the problem being addressed. The correct choice of mathematical model for the problem is an obvious prerequisite. The UK Health and Safety executive [47] as well as a the EU-wide MARNET [48] have developed guidelines to aid in this process. While these guides help the CFD practitioner to identify the most suitable model to solve a specific problem, a more rigorous approach will seek to assess the impact of various modelling assumptions. Especially when solving numerous variations of one specific problem, identifying the best trade-off between modelling complexity and speed is of considerable economic importance as well.

There are three main methods within CFD, each solving a fluid model of increasing complexity:

1. Panel Methods. These are the natural progression from closed-form solutions obtained from inviscid incompressible irrotational (potential) flow. The surfaces of complex shapes are represented using discrete panels, usually quadrilaterals, defined on the surface of interest. Although Hirsch [49] recommends that this approach be replaced by more sophisticated methods, panel methods continue to be used, both on their own and in combination with other methods. This may be explained by the fact that panel methods need only to discretise the boundaries of the fluid domain, a reduction in com-

putational cost of two to three orders of magnitude compared to the methods below.

2. Euler Equations. The Euler model still assumes inviscid flow, eliminating a second derivative. The conditions requiring irrotationality and incompressibility are lifted, permitting more realistic representation of fluid behaviour. However, the full fluid domain, as opposed to only the boundaries, has to be discretised.

3. Navier Stokes Equations. This is the most complex fluid model available to date, providing the most faithful representation of true fluid behaviour. This is offset by increased computational requirements due to the discretisation of nonlinear terms as well as the need to discretise the full fluid domain.

Sometimes, two models are combined in one problem to reduce computational cost, for example when using Euler equations or potential flow in the far-field region when solving the flow over a wing. However, this requires some prior knowledge of the problem and introduces an additional unknown into the solution.

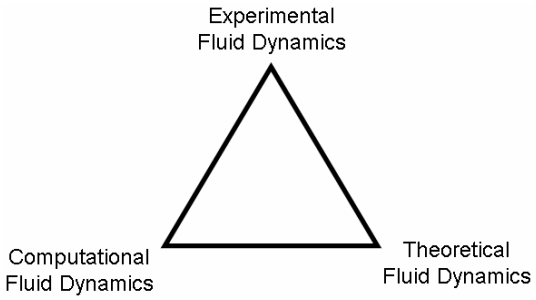

Figure 3.1: The solution methods in fluid dynamics

It should be emphasised that despite the realism implied by the complexity of the aforementioned models, they are no substitute for reality. A well-founded solution to a fluid dynamics problem will usually resort to more than one of the approaches shown in figure 3.1. Synthesising CFD, experimental methods and theoretical analysis will, in most cases, give the best overall result [50].

3.2 Viscous Fluid

3.2.1 Navier Stokes Equations

The Navier-Stokes Equations describe the behaviour of a viscous (usually Newtonian) fluid. This considerably more general model introduces nonlinearities rendering a closed-form solution for all but the simplest cases impossible. Unfortunately sloshing is not one of these. Strictly speaking, the Navier Stokes equations refer to the conservation of momentum equations, which when coupled with a continuity and other applicable equations yield a solvable system. However, in the field of CFD the term 'Navier-Stokes equations' is often used to refer to the full set of equations used, this terminology will be adopted here as well. Two main variations are used for flow modelling:

1. Incompressible Flow. This introduces the assumption that all fluids incompressible (i.e. $\rho = \text{const}$), a satisfactory simplification for most marine applications. The incompressible Navier Stokes equation may be written in cartesian tensor notation as

$$\frac{\partial u_i}{\partial x_i} = 0, \tag{3.1a}$$

$$\frac{\partial u_i}{\partial t} + u_j \cdot \frac{\partial u_i}{\partial x_j} = -\frac{1}{\rho}\frac{\partial p}{\partial x_i} + \nu \frac{\partial^2 u_i}{\partial x_j \partial x_j} + b_i, \tag{3.1b}$$

   where b_i is the body force, ν kinematic viscosity, ρ fluid density, p pressure, t time and u_i the velocity vector.

2. Compressible Flow. Here density is allowed to vary, but the introduction of density as an additional variable requires a further equation to complete the system - in this case an ideal gas equation of state (3.2d). This additional complication is often necessary when a fluid is subjected to violent motions or interphase transfer is significant, as is the case in an LNG tank:

$$\frac{\partial \rho}{\partial t} + \frac{\partial}{\partial x_i}(\rho u_i) = 0, \tag{3.2a}$$

$$\frac{\partial}{\partial t}(\rho u_i) + \frac{\partial}{\partial x_j}(\rho\ u_j\ u_i) = -\frac{\partial p}{\partial x_i} + \mu \frac{\partial^2 u_i}{\partial x_j \partial x_j} + b_i \tag{3.2b}$$

$$\frac{\partial}{\partial t}(\rho I) + \frac{\partial}{\partial x_i}(\rho\ I\ u_i) = -p\frac{\partial u_i}{\partial x_i} + k\frac{\partial^2 T}{\partial x_i \partial x_i} + \Phi + T_{ext} \tag{3.2c}$$

   with

$$p = \rho R T \tag{3.2d}$$

and

$$I = C_v T, \tag{3.2e}$$

where C_v is the specific heat at constant volume, I internal energy, k thermal conductivity, μ dynamic viscosity, Φ viscous dissipation (heat generated by fluid viscosity), R the Boltzmann constant, T absolute temperature and T_{ext} external heat sources. Note the vast increase in complexity introduced when considering compressibility. However, compressibility reduces the 'stiffness' of the numerical system and often improves the speed of convergence for iterative solution techniques. The problem is complicated further when introducing multiphase flow. In that case, the governing equations (3.1) or (3.2) are solved for each fluid, with the appropriate boundary conditions (usually continuity of pressure and shear stress as well as ideally interfluid surface tension) applied at the fluid interface.

3.2.2 Spatial and Temporal Boundary Conditions

The solution of any differential equation requires boundary conditions to define a specific problem, the Navier Stokes equations (3.1) and (3.2) are no exception. If the problem is time-dependent the initial conditions need to be specified as well. The two main types of boundary conditions used in CFD are the Dirichlet and Neumann conditions. The Dirichlet boundary condition implies the direct specification of boundary values known as part of the problem, or, if the value is unknown the gradient $\frac{\partial}{\partial x_i}$ has to be specified. This is the Neumann boundary condition.

The boundary conditions required for the sloshing problem are straightforward. The sloshing takes place in an enclosed container. Therefore, the velocity and temperature can be specified explicitly on the tank walls. However, an absolute reference pressure value needs to be specified at some location within the fluid domain. The temporal boundary, or initial condition, was implemented by specifying zero fluid motion at $t = 0$ and applying the sloshing motion to the container. The methods available to do so are considered in greater detail in section 3.4.

The absolute pressure in the domain was set by either specifying the pressure at a particular node or leaving one node on the top (North) wall as an outlet. Note that the second method requires a check on conservation of mass, as water could in theory exit the domain. However, this second method of specifying the pressure resulted in instabilities with the single phase models analysed in this report. Multiphase solutions, given in section 6.4.2, were considerably more stable with a single node outlet.

3.2.3 Introduction to ANSYS™ CFX-10.0™

CFX-10.0™ is a finite volume based CFD package using a variation of the SIMPLE algorithm for momentum-pressure decoupling [51]. The code features multiphase capability as well as advanced turbulence models. Interoperability with the structural finite element code ANSYS™ is made possible to allow simulation of fluid-structure interaction. The code is split into a preprocessor, where the problem is defined, a solver and a postprocessor, which outputs the solver results in a useful format[3]. As with most commercial CFD codes, CFX™ offers a multitude of modelling options for a given problem. Identifying the most suitable combination is, depending on the range of choices, a task of some complexity. A prerequisite to the presentation of any CFD result is a grid independence study, this is carried out in section 4. Other modelling aspects such as fluid compressibility must be addressed as well. While one may be tempted to use the most complex model, the time penalties associated with this course of action have become evident in the previous section 3.2.1.

CFX-10.0™, as well as its competitors Fluent and Star CD, are based on the finite volume method, essentially an integral version of the well-known finite difference method. The finite volume method attributes its popularity to two main factors:

1. Ease of Discretisation. This method may be applied to virtually any geometry, regardless of complexity. The limiting factors are cell density and aspect ratio, especially when modelling a turbulent flow.

2. Inherent Conservation of Physical Properties. The finite volume method, through the

[3]Screenshots of the CFX-10.0 preprocessor, solver and postprocessor, as well as an explanation of the selected input parameters is given in Appendix A

use of of Gauss' divergence theorem

$$\int_{CV} div\ a_i\ dV = \int_{A} n.a_i\ dA, \tag{3.3}$$

where A is the border enclosing the control volume CV, n a unit vector normal to A and a_i any physical quantity (multidimensional problems will result in $i > 1$), is conservative. Gauss' theorem is used to replace the divergence operator in the Navier Stokes equations, discretising the governing equations on the mesh. This discretisation scheme ensures that the exact same physical quantity (e.g. mass) leaving one control volume enters an adjacent control volume. While this approach works well for single-phase problems, multiphase solutions are considerably more susceptible to numerical diffusion of mass and momentum. A discussion of the foundations of finite-volume CFD is given by Ferziger & Peric [52] and Versteeg & Malalasekera [53].

3.3 Turbulence Modelling

The governing equations (3.1) and (3.2) are valid for all flow regimes satisfying the restrictions imposed by the assumptions made. The successful numerical solution depends on sufficient grid resolution to capture all flow features. Turbulence takes place at often very small spatial and time scales. In order to capture the effects of turbulence using the governing equations in their present form, grids with extremely high resolution and very small time steps would be required. As turbulence is a three-dimensional time-dependent phenomenon [54], no two-dimensional CFD would be permissible. Currently, there is a field within CFD, called Direct Numerical Solution (DNS), which attempts to model turbulent flows using the prerequisite grids and timescales [50]. However, this field is currently confined to problems of mainly academic interest, as no computers powerful enough exist to make DNS a practical reality.

The onset of turbulence occurs on a suitable Reynolds number (equation 2.5); for an internal flow this is $O\left(10^3\right)$, while an external flow is considered turbulent above a Reynolds number of $O\left(10^5 - 10^6\right)$. The actual onset of turbulence is governed by a variety of factors such as the geometry of a body and its surface properties; as well as the time history of the flow.

Since many engineering flows of interest are turbulent, there is a clear need to account for the effects of turbulence without the prohibitive computational aspects of DNS. This has given

rise to the field of turbulence modelling. Turbulence models vary greatly in their theoretical approach and complexity; a thorough discussion is given by Wilcox [55].

Numerous studies of sloshing use potential flow as well as Price and Chen [56] who used a laminar representation, assuming that the flow is not turbulent. Other recent computational sloshing simulations by Hadzic [57], Standing *et al* [58] and more recently Rhee [59] resort to a turbulence model. As there is no consensus as to the degree of turbulence in a sloshing flow a methodical analysis is given in section 6. At this stage it is useful to identify the significance of turbulence and give a brief overview of the two turbulence models used in this study.

3.3.1 Background

Turbulence models have evolved considerably from the early boundary layer approximations and are often designed for a particular flow regime and may be tuned using experimental data to give the 'best' computational results. Even today, turbulence modelling is considered to be one of the most demanding areas of fluid dynamics and mathematics. Experimental observations have greatly enhanced understanding of turbulence and are used to justify the underlying principles of most turbulence models. In 1937, von Karman defined turbulence as

> an irregular motion which in general makes its appearance in fluids, gaseous or liquid... [55]

Improved understanding of chaotic processes has permitted the refinement of this definition, introducing the concept of time-averaging. Thus, the random component of a turbulent signal (e.g. pressure or velocity) when averaged over time would equal zero. Defining the mean of a time dependent fluid property $\Omega(t)$ over the averaged time T as

$$\overline{\Omega} = \frac{1}{T}\int_0^T \Omega(t)\ dt, \tag{3.4}$$

so that

$$\Omega(t) = \overline{\Omega} + \Omega'(t), \tag{3.5}$$

with the rapidly varying component Ω'

$$\overline{\Omega'(t)} = 0. \tag{3.6}$$

The application of this procedure to the governing Navier Stokes equation (3.2) results in the Reynolds-Averaged Navier Stokes Equation (RANS)

$$\frac{\partial\left(\rho\overline{U}_i\right)}{\partial x_i} = 0, \tag{3.7a}$$

$$\frac{\partial\left(\rho\overline{U}_i\right)}{\partial t} + \frac{\partial}{\partial x_j}\left(\rho\overline{u}_i\overline{u}_j + \rho\overline{u_i'u_j'}\right) = -\frac{\partial\overline{P}}{\partial x_i} + \frac{\partial}{\partial x_j}\left[\mu\left(\frac{\partial\overline{U}_i}{\partial x_j} + \frac{\partial\overline{U}_j}{\partial x_i}\right)\right]. \tag{3.7b}$$

This procedure introduces, for a three dimensional problem, six additional unknowns to the momentum equation (3.7b). Alas there is no readily available exact formulation to close the system by expressing the Reynolds (or Turbulence) stress $\rho\overline{u_i'u_j'}$ in terms of quantities known from the flow field. The closure of the turbulence problem generated by Reynolds averaging is the starting point for turbulence models.

Given the variety of turbulence models available in CFX-10 [51], it is important to identify the turbulence model performance requirements and the flow regime expected. The required output from the CFD simulation will be the wall pressure distribution, with the correct near-wall velocity field being of secondary consideration. However, recalling the sensitivity of the flow to small disturbances near the natural sloshing frequency [17] as well as the different length scales expected in the sloshing flow, a simple zero-equation turbulence model is deemed unlikely to capture the physics with sufficient accuracy. The two equation $k-\epsilon$ model has been used in a variety of sloshing studies and its wide field of application makes it a useful initial choice. The Shear Stress Transport, SST, model was used as well. However its sensitivity to the the constantly changing y^+ caused significant difficulties and most runs diverged before completion. However El Moctar [23] reports the successful use of the SST model in a sloshing flow.

A second class of turbulence models, the Reynolds stress models provides more generality at much greater computational cost. The Speziale, Sarkar & Gatsi (SSG) model described below was included for more detailed study. More complicated methods such as Detached Eddy Simulation were not considered due to the massive computational costs. The same is true for Large Eddy Simulation, as for both a three-dimensional computational domain is required.

3.3.2 Turbulence Models - the $k-\epsilon$ Model

The Boussinesq assumption is used as the basis of a number of early turbulence models [55]. It relates the turbulence stress to mean flow properties through turbulent viscosity. Using k, the turbulence kinetic energy and ϵ, the eddy dissipation, all quantities defining turbulence, namely a length scale, time scale and a quantity of the same dimension as turbulent viscosity, can be obtained. Thus, the $k-\epsilon$ model is said to be complete as no flow-specific parameters are required [54].

The $k-\epsilon$ model is one of the most widely used turbulence models in CFD. It requires two additional transport equations, a notable increase in required computational effort. The Boussinesq assumption is implemented in the $k-\epsilon$ model as

$$\nu_t = C_\mu \frac{k_t^2}{\epsilon_t}, \tag{3.8}$$

where ν_t is turbulent viscosity, C_μ a constant typically taken as 0.09, k_t turbulence kinetic energy and ϵ_t turbulence kinetic energy dissipation. Both k_t and ϵ_t are solved throughout the computational domain with transport equations analogous to mass and momentum. A more rigorous introduction to the theoretical foundation of the $k-\epsilon$ model is given by Pope [54] and Wilcox [55].

The $k-\epsilon$ model has been used for a considerable time in industry with a large spectrum of applications. Its popularity is attributed to the comparative simplicity for a complete turbulence model [54] and robustness. However, there are several weaknesses of the $k-\epsilon$ model [60].

1. Inaccuracies in strong or adverse pressure gradients [54],
2. inability to model the law of the wall without viscous correction [55],
3. difficulties modelling problems more complex than simple shear [54] and
4. the specification of initial values throughout the domain. However, this problem can be overcome by starting the sloshing simulation from a zero velocity field, with clear implications for the consequent turbulence field.

In fact, Wilcox [55] does not consider the popularity of the $k-\epsilon$ model to be supported by its performance characteristics. The selection of a turbulence model is not straightforward, as modelling accuracy, computational requirements and most importantly the impact of turbulence on the final result need to be weighed against one another. It is instructive to vary the turbulence model for a given problem [48], as this permits the identification of effects particular to one turbulence model.

3.3.3 Turbulence Models - the Reynolds Stress Speziale, Sarkar & Gatsi (SSG) Model

Reynolds stress models do not rely on the Boussinesq assumption, instead the turbulence stresses are modelled directly. The advantage of this approach is a far greater level of generality, many of the drawbacks associated with $k-\epsilon$ models do not apply [51]. The Reynolds stress model used in this study was introduced by Speziale, Sarkar and Gatsi [61]. The strengths of this particular model are:

1. Better performance in complex flow regimes, especially in strongly curved streams [51]; and

2. Improved stability as the asymptotic solution attracts all initial conditions [61].

The main drawback of any Reynolds stress model is the introduction of five additional transport equations for a three dimensional problem. In addition, some convergence problems are identified in the CFX users' guide [51] when using the SSG model.

While one may be inclined to consider the more complex turbulence model as superior, there are several important points to note.

1. Most turbulence models are developed for aerospace applications with a different (transonic) flow regime. A premium is placed on obtaining the correct velocity gradient in the near wall region. The sloshing flow is dominated by pressure, with different demands on the turbulence modelling approach.

2. When comparing turbulence models it is not a foregone conclusion that the SSG model will obtain superior results. A model should include the key physics with the minimum

required effort [55], the most suitable turbulence model will thus be identified in section 6. Speziale *et al* arrive at a similar conclusion

> ...adding substantially more complex nonlinear terms containing the anisotropy tensor may be of questionable value in the modelling of the pressure-strain correlation [61].

3.4 Sloshing Motion

The physical sloshing problem is not suitable for traditional steady-state CFD, as it is inherently transient and, more significantly, the motion is caused by the movement of the fluid domain. The first issue can be dealt with effectively when quasi steady-state solutions, termed 'coefficient loop iterations' in CFX, are used in conjunction with a time marching scheme evolving the flow in time. However, this introduces another dimension to the problem, rendering the three dimensional sloshing problem computationally demanding. The second problem, the domain motion, is somewhat more complex. Two solutions are available: (1) a body force and (2) introducing a moving grid.

3.4.1 Body Force

Using a body force approach is far simpler, although not as intuitive as the moving grid. The tank displacement described in an inertial (X, Z) coordinate system with origin O is given by equation (3.9) as

$$x_{X,Z} = \sin(\omega t), \tag{3.9}$$

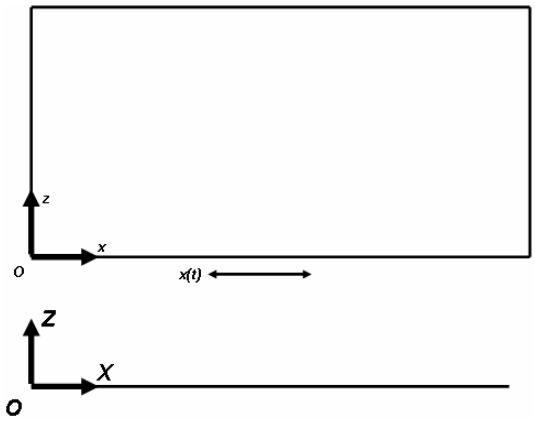

Figure 3.2: Inertial system with periodic tank motion

assuming the displacement of the tank is sinusoidal with origin o and axis system (x, z). Therefore the acceleration of the tank at o relative to (X, Z) is given by

$$\ddot{x}_{X,Z} = -\omega^2 \sin(\omega t). \tag{3.10}$$

Keeping the same notation, the displacement of the tank observed at O relative to o is

$$X_{x,z} = -\sin(\omega t)\,. \tag{3.11}$$

Similarly, the acceleration is given as

$$\ddot{X}_{x,z} = \omega^2 \sin(\omega t)\,. \tag{3.12}$$

Therefore, the same motion, a periodically oscillating tank, can be described both within the problem, as shown in equation (3.11), as well as using an external reference system. This is the essence of the body force approach. By applying an additional acceleration to the domain it is possible to simulate the sloshing motion without having to move the grid relative to an inertial reference system. Equation (3.12) uses a sinusoidal motion, but any arbitrary motion can be simulated by splitting the accelerations into their Cartesian components and using Fourier series. Recalling the incompressible Navier Stokes momentum equation (3.1b) for simplicity

$$\frac{\partial u_i}{\partial t} + u_j \cdot \frac{\partial u_i}{\partial x_j} = -\frac{1}{\rho}\frac{\partial p}{\partial x_i} + \nu \frac{\partial^2 u_i}{\partial x_j \partial x_j} + b_i, \tag{3.13}$$

the last vector component b_i contains the body forces, e.g. gravity $\mathbf{g} = (0, 0, 9.81)$ applied to the system governed by equation (3.1b). For the present case, the momentum equation would then be modelled as

$$\frac{\partial u_i}{\partial t} + u_j \cdot \frac{\partial u_i}{\partial x_j} = -\frac{1}{\rho}\frac{\partial p}{\partial x_i} + \nu \frac{\partial^2 u_i}{\partial x_j \partial x_j} + \left(\ddot{X}_{x,z}, 0, 9.81\right), \tag{3.14}$$

with $\ddot{X}_{x,z}$ having been derived in equation (3.12). Thus, the simplicity of the body force approach becomes apparent, especially when one considers the complications introduced by the moving grid approach discussed in section 3.4.2. A further benefit of the body force approach is that accelerations, more readily measurable on a moving body than velocities or displacements, are required as inputs.

3.4.2 Moving Grid

While the body force approach outlined previously is somewhat counter-intuitive yet very simple to implement in a numerical sloshing model, the moving grid approach is the opposite. It involves moving a body (in the present case the sloshing tank) by applying equation (3.9) to the geometry. The Navier Stokes equations, irrespective of the degree of simplification,

contain partial derivatives in space and time. While the two are separate when using a stationary grid, for a moving mesh in the one dimensional case

$$\frac{\partial u}{\partial t} = \frac{\partial u}{\partial t} + \frac{\partial u}{\partial x}\frac{\partial x}{\partial t}, \tag{3.15}$$

as $u = u(x,t)$ and $x = x(t)$, so that $u = u(x(t),t)$.

In other words, the simple time derivative $\frac{\partial u}{\partial t}$ becomes a much more involved total derivative $\frac{Du}{Dt}$. Another problem more of a numerical nature emerges when the grid is moved, the dependent variables being solved (velocity, pressure, etc.) are not known on the new grid locations. Therefore an interpolation scheme is required to determine the fluid properties at the new grid locations with a consequent loss in accuracy. A moving grid approach is sometimes necessary, but its use implies a penalty in required computational time and numerical accuracy.

Hadzic *et al* [57] examined the results for the same problem using either procedure. The authors determined that both approaches give the same pressure data after a brief transient period of disagreement. Given that information along with the fact that both approaches describe the same motion (albeit from a different reference frame), one may arrive at the conclusion that both are valid. However, due its simplicity, all subsequent investigations will use the body force approach for discretising the sloshing motion. Nonetheless, the moving grid may well need to be used to simulate hydroelasticity at a later time.

3.5 Test Problem

The computational results are compared to experimental data to confirm the validity of the modelling assumptions. Hinatsu [2] has carried out a series of sloshing experiments at the National Maritime Research Institute of Japan. The experiments involve pure lateral and angular motion, there are no results for combined motions. Olsen [34] observed that

> the predominant and most important kind of sloshing is the lateral sloshing, generated primarily by lateral and angular tank movements.

Therefore, the current study will be restricted to the lateral sloshing problem. Experiments were carried out for $0.95T_{11}$ and T_{11}, where T_{11} is the first natural sloshing period. As this

study is attempting to identify the most suitable CFD analysis methodology, making no attempt to isolate the most significant natural sloshing frequencies, it is not necessary to take the conclusions of section 2.2.2 into account.

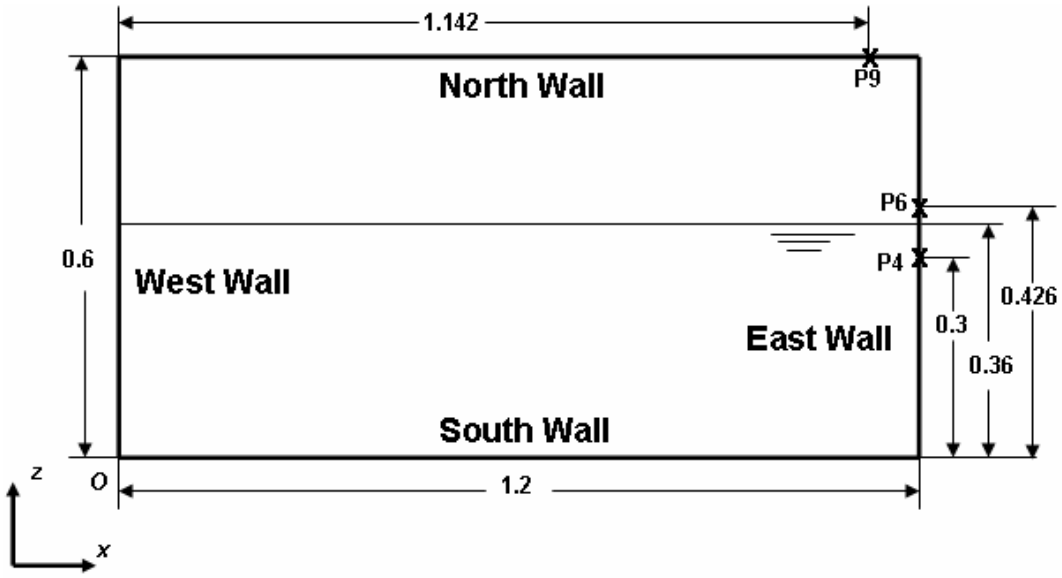

Figure 3.3: The sloshing tank used in all test problems. *All dimensions in m*

The validation problem chosen is lateral sloshing at $0.95T_{11}$ in a rectangular container depicted in figure 3.3. The tank is moved along the x axis only (as shown in figure 3.3), with displacement being given as a function of time

$$x = A \sin\left(\frac{2\pi}{T}\, t\right), \tag{3.16}$$

where $A = 0.015$ m is the displacement amplitude, $T = 1.404$ s the sloshing period and t the elapsed time. Pressure readings are taken at sensors P4, P6 and P9, located near the tank East wall.

3.5.1 Experimental Results

The experimental results are shown in figure 3.4. These pressure histories for seven sloshing oscillations, measured with respect to external atmospheric pressure, are for steady state sloshing at the indicated positions. Note that the trough at P4 (shown in figure 3.4(a)) oscillates about a zero pressure, while P6 and P9 oscillate about a pressure of 200 N/m^2 during

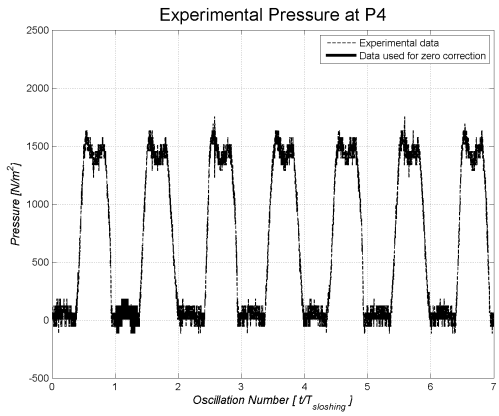

3.4(a): Raw Data - P4

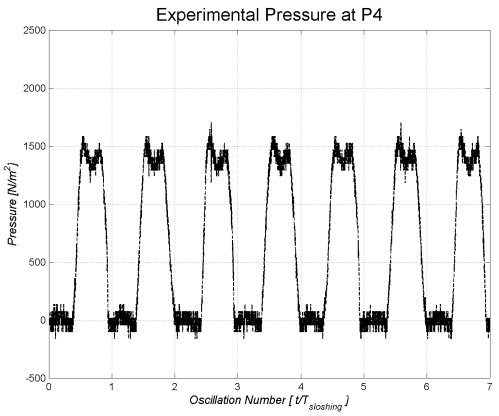

3.4(b): Corrected Data - P4

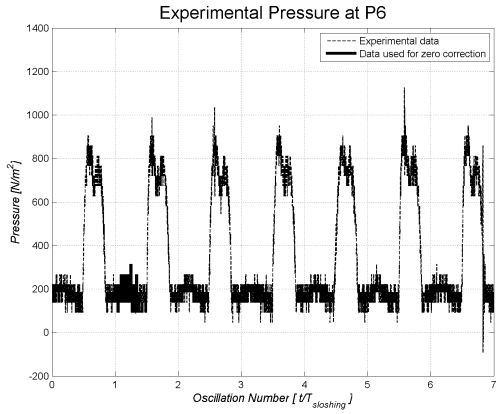

3.4(c): Raw Data - P6

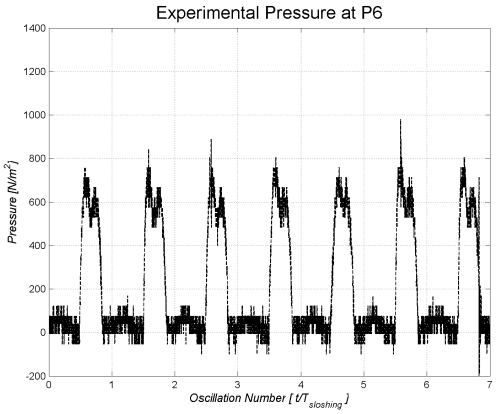

3.4(d): Corrected Data - P6

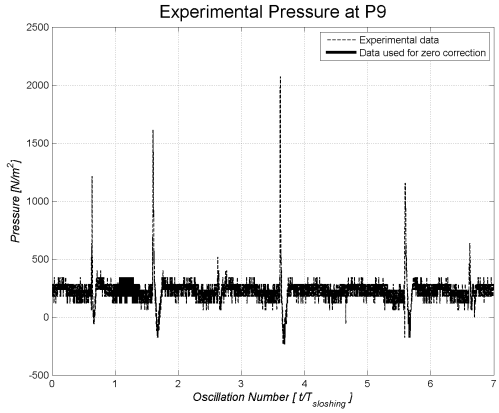

3.4(e): Raw Data - P9

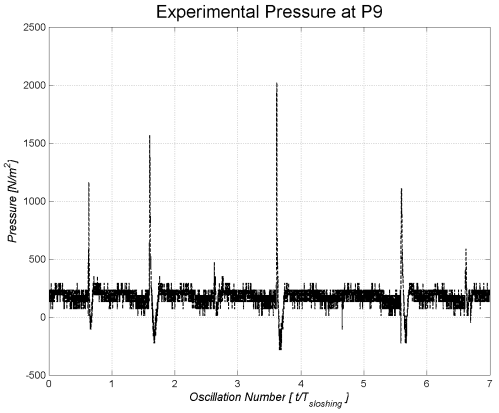

3.4(f): Corrected Data - P9

Figure 3.4: Pressure obtained from experiment, raw data [2] (left column) and corrected data (right column)

that period. During flow reversal, where the global velocity field is near-zero, the pressure is, according to Bernoulli's equation, dominated by the static contribution. Therefore, one would expect the pressure trough at P4 to be greater than or equal to the pressure at P6 and P9. This is taken into account in the right column of figure 3.4, using the assumptions that the reading at P4 is correct and the offset at P6 and P9 is a constant.

At this stage it is useful to consider a typical sloshing pressure peak as depicted in figure 3.5 in more detail. Using the CFD pressure and velocity fields as a basis for analysis, there are three distinct phases:

1. The primary (initial) peak occurs when the sum of static pressure and all dynamic pressure contributions are at the maximum. This is often the peak sloshing pressure.

2. The static pressure increases further, but the fluid velocity decreases with a consequent reduction in dynamic pressure. This second phase is the trough in the pressure peak shown in figure 3.5, only static pressure is observed.

3. The secondary peak occurs when the fluid velocity increases from its minimum in the previous phase. Static pressure is decreasing, but the sum of static and dynamic pressure increases for a limited amount of time until the sum of static and dynamic pressure starts to decrease.

The results may be validated further when considering the static pressure contribution. The sloshing liquid behaves similarly to a pendulum. It reaches the maximum displacement when the velocity field is effectively zero. Using potential flow and Bernoulli's equation as an approximation, one may assume that the pressure is dominated by the static term $p_{static} = \rho g h$ at flow reversal. Using the pressure at P4, the mainly static pressure (from the above assumptions) is 1375 N/m^2, which relates to a pressure head of

$$h = \frac{1375 N/m^2}{1000 kg/m^3 \cdot 9.81 m/s^2} = 0.143 m \tag{3.17}$$

above P4, or 0.44 m above the bottom of the tank. This corresponds well to the maximum water height of 0.435 m observed in the CFD simulations described in the grid independence study 4. However, when considering P6, which is nearer the free surface, the corresponding

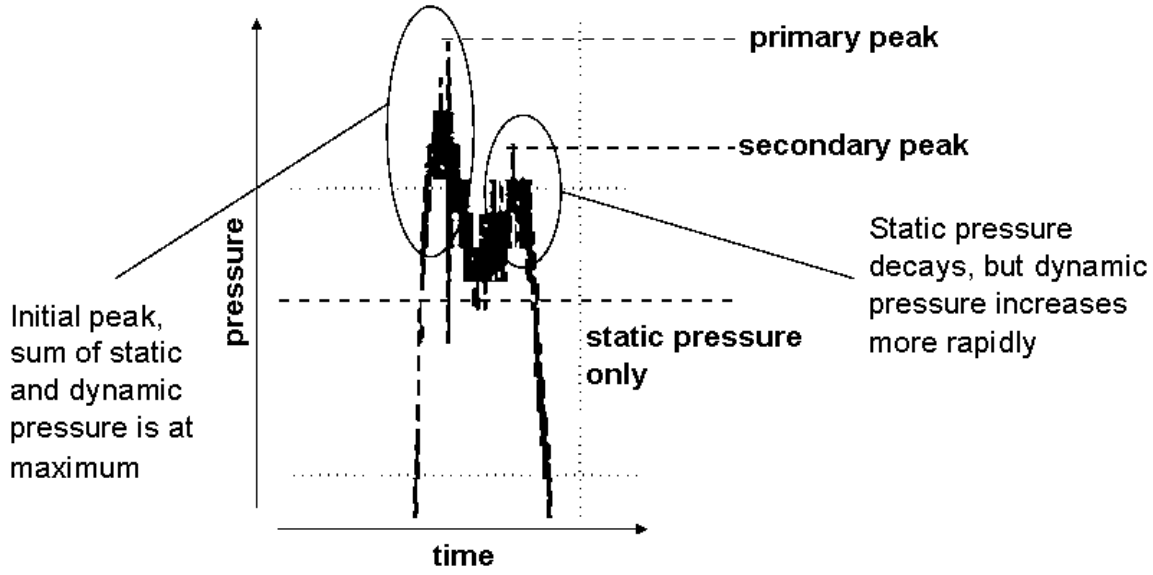

Figure 3.5: Typical sloshing pressure peak

static pressure is expected to be 165 N/m^2, compared to the reading of 600 N/m^2. Clearly this discrepancy requires further explanation.

1. Static Pressure. The assumption of static pressure dominating the entire flow field may not be valid near the free surface, where surface tension and fluid curvature influence the pressure as well. This is confirmed when considering the CFD results in later sections: the pressure at P6 (see figure 5.2(b), for example) peaks near 350 N/m^2, well in excess of the static pressure.

2. Pressure Sensor Error. Given the previous discussion, there may be a steady state error in the pressure sensor, distorting the results. A method of addressing this has been suggested previously, but a more careful investigation may be required to ascertain the validity of the experimental results.

3.5.2 Motion Analysis

While the pressure results were discussed in the previous section, this section considers the method of discretising the motion of the tank as indicated in equation (3.16). The acceleration applied by the body force approach is given by the second derivative of equation (3.16) as

$$\ddot{x} = a = -A\frac{(2\pi)^2}{T^2}\sin\left(\frac{2\pi}{T}\ t\right). \tag{3.18}$$

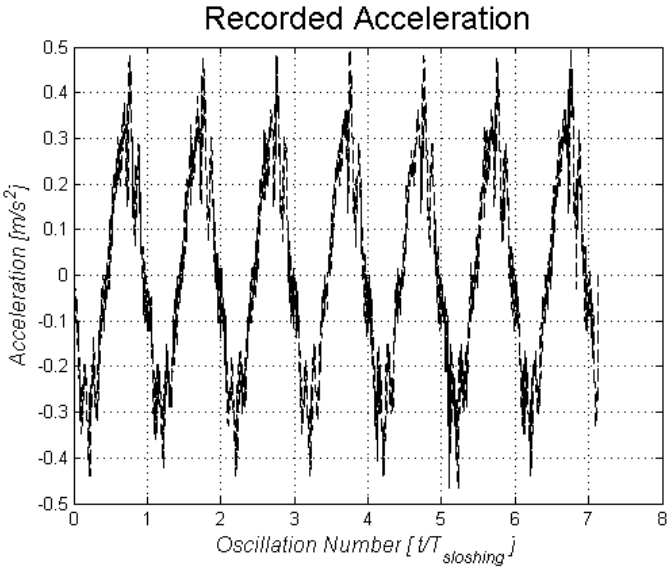

3.6(a): Recorded acceleration from experiment [2]

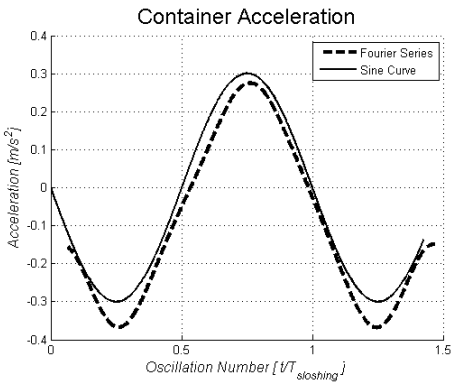

3.6(b): Reconstructed acceleration using 5 Fourier series components

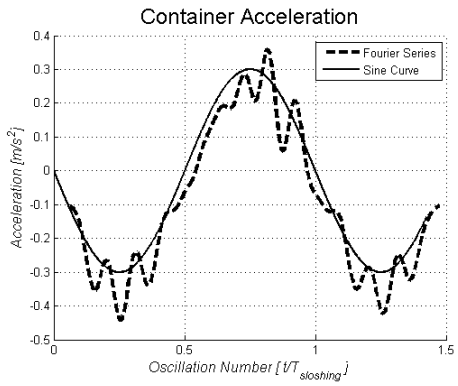

3.6(c): Reconstructed acceleration using 20 Fourier series components

Figure 3.6: Fourier analysis of tank acceleration

The tank acceleration recorded during the experiments is shown in figure 3.6(a). Clearly this plot bears little resemblance to a sine curve. However, using the Fourier series given by equation (2.1) it is possible to isolate the most significant components. Figures 3.6(b) and 3.6(c) show the plots reconstructed with Fourier transforms. In figure 3.6(b), only the first five terms of the series are used. One may observe that equation (3.16) represents the low frequency properties of the actual tank acceleration very well, with only a small offset in the positive y-axis. However, as higher frequency terms are introduced the Fourier transform plot resembles the observed data, as shown in figure 3.6(c).

While the experimental data available is not fully consistent, it is suitable for validation of the CFD results. Further confidence is given by the fact that they have been used previously in literature (e.g. ref [23], [57] and [59]) for validation of other CFD studies. Finally, it is confirmed that the acceleration the sloshing tank is subjected to can be approximated using a sinusoidal function.

4 Grid Independence

4.1 Background

Because of the complexity attributable to the nonlinear terms in the Navier Stokes momentum and energy equations most viscous flow problems have to be solved numerically. A grid (or mesh, the terms are often used interchangeably) is used to represent the problem in computational fluid dynamics usually as a set of finite volume elements. Expertise in the generation of high-quality computational grids has developed alongside CFD and a wide range of literature is available [62]. Section 3.2.3 drew attention to the finite volume method used to discretise the problem in this study. The grid design process is centered around the following trade-offs.

1. Spacing. The grid needs to be sufficiently fine so as to sustain conservation of mass and momentum at an acceptable level. However, reducing grid size will increase the computational cost and memory requirements. The rate of increase depends on the type of solution algorithm used. The computational requirements of direct matrix inversion methods grow with $O\left(n_{cells}^3\right)$ but iterative algorithms are around $O\left(n_{cells}^2\right)$. In addition, when modelling a transient problem the time step needs to be adjusted according to grid size (smaller the mesh - smaller the timestep). This process is governed by the Courant number, discussed in more detail in the section 5.2.

2. Resolution. Grid spacing needs to be sufficiently small to resolve the flow in all regions of the computational domain. This is especially important when using a turbulence model, where the position of the first near-wall grid point can have a significant influence on the CFD output quality. This is discussed by Wilcox [55] in considerable detail. When the grid is too coarse, local flow features are smeared and, especially when considering a sloshing flow, pressure spikes are not resolved with sufficient detail.

3. Geometry. Although not an issue in the current study, the grid must provide a sufficiently accurate representation of the geometry used. This becomes very important when there are small changes (e.g. ripples) on a surface, or a body has particular details influencing the flow.

As the grid represents the problem in computational space, one should always ascertain that any CFD result is independent of the grid used. This has been considered by Roache [63] and the Maritime CFD best practice guidelines [48]. The UK Health and Safety Executive requires grid independence of critical CFD analyses [47], hence any result of practical interest should conform to this requirement. This section details the results obtained with four successively refined grids. A formal grid independence study is carried out in section 4.5.

The sloshing problem is modelled as a turbulent flow, a $k - \epsilon$ turbulence model is used. While the problem includes two fluids, only a single velocity field is computed. CFX offers three different spatial discretisation schemes. [51]

- First Order Upwind Scheme. This is numerically robust [51], but subject to numerical diffusion.
- Specified Blend Factor. Here, an 'Anti-Diffusive Flux' [51], governed by the scalar variable $0 \leq \beta \leq \sqrt{3}$, where $\beta = 0$ is the previous first order scheme and $\beta = 1$ formally second order accurate. While conservation properties are improved, it is numerically less stable than the first order scheme.
- High Resolution. The high resolution uses $\beta = 1$ in low variable gradient regions of the flow field, while the first order scheme is used where gradients are steeper. The governing variable β is computed throughout the flow field.

Spatial discretisation was implemented using the pure second order scheme as does not introduce uncertainties with respect to the order of accuracy as is the case with the high resolution scheme while the conservation properties are better than the first order scheme. Temporal discretisation, discussed in greater detail in section 5, is implemented using a first order backward Euler scheme. As the first order scheme is more susceptible to numerical diffusion and a finer grid requires a smaller timestep (see section 5.2), the improved conservation properties of the refined grids may be offset or even exceeded by the imbalances introduced by the time discretisation scheme. Note that the key aspects of each simulation of the grid independence study are summarised in a tabular format in their respective sections.

4.2 Grids Used

The grids were constructed using the grid generation package ICEM, developed by ANSYS for use with, but not limited to CFX. ICEM uses a top-down grid generation approach, starting with the rough outline of a geometry and subsequently refining it. As the current problem is a rectangular box, the geometry did not introduce any difficulties. Initially, a regular grid was constructed which was then converted into an unstructured grid consisting exclusively of hexahedral elements. The two-dimensionality of the problem was simulated by making the x_3 dimension one element deep. One weakness of ICEM can be the lack of computational stability when generating hybrid meshes, combining hexahedral and tetrahedral (or pyramid, for 2D problems) elements.

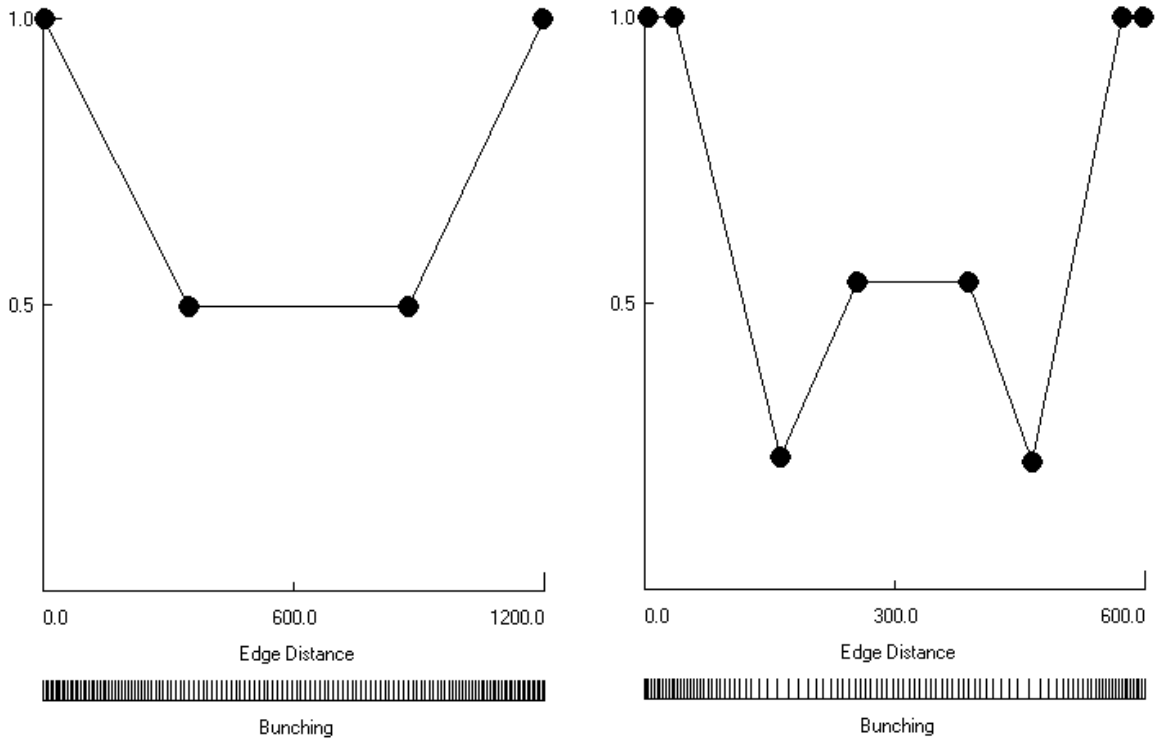

4.1(a): x-direction

4.1(b): z-direction

Figure 4.1: Non-dimensional grid density in container. *All dimensions in mm*

As shown in figure 3.3 in section 3.5, the tank is of rectangular box shape (1.2 m by 0.6 m), with a filling level of 0.36 m. The first grid point was chosen to be 1 mm from the wall, the distribution of grid points is varied using linear functions defined in ICEM. The

non-dimensional grid density in the x-direction is given in figure 4.1(a) and for the z-direction it is given in 4.1(b). The grid points are distributed so that they are concentrated near the walls and the initial free surface. The grid distributions defined in figure 4.1 are identical for all grids used in this study.

The current grid independence study employs four progressively finer spaced grids. The particulars of the grids are given in table 4.1. The four grids are shown in figure 4.2 with the

Table 4.1: Grid statistics for the grid independence study

Grid	**Nodes**			**Elements**		
	Total Nodes	x-dir	z-dir	Total Elements	x-dir	z-dir
1	5600	140	80	2691	69	39
2	12000	200	120	5841	99	59
3	28000	280	200	13761	139	99
4	56000	400	280	27661	199	139

initial free surface location illustrated as well. On all four grids, a sinusoidal sloshing motion given by equation (3.16) in section 3.5 was applied at $0.95T_{11}$. All computational and physical parameters were kept constant, as specified in table 4.2.

4.3 Error Analysis Theory

A procedure to determine grid independence is presented by Roache [63], this section summarises the key results used in this report. Other aspects of quantifying grid quality are given by Thompson [62] and MARNET CFD [48]. The following CFD results will be used in the grid independence study:

1. pressure,
2. force and
3. free surface position.

Finally, the order of convergence of the algorithm is calculated.

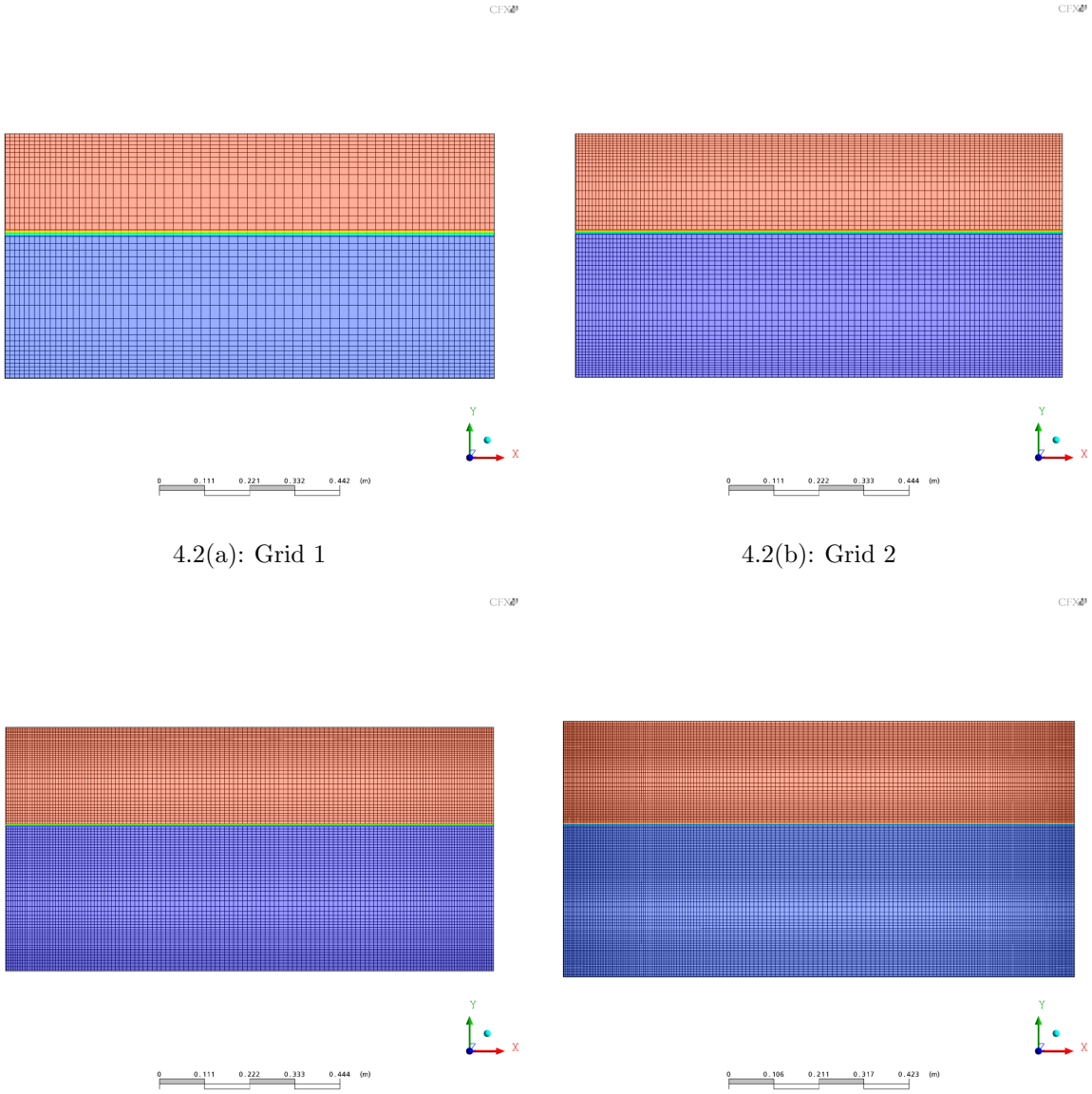

4.2(a): Grid 1

4.2(b): Grid 2

4.2(c): Grid 3

4.2(d): Grid 4

Figure 4.2: Grids used in the grid independence study

The study of grid independence is based on the theory introduced by Richardson (Roache, [63]). Assuming that an algorithm of order k is used on a grid with cell refinement ratio $r = n_2/n$, $r > 1$, one may write

$$I - I_n = C_n \cdot n^{-k}, \tag{4.1}$$

where I is the actual solution, I_n a solution obtained using n nodes and C_n a constant. Replacing n in equation (4.1) with rn provides an analogous expression for the fine grid with

refinement ratio r

$$I - I_{rn} = C_{rn} \cdot (rn)^{-k}\,. \tag{4.2}$$

The assumption inherent in this procedure is that $C_n \approx C_{rn}$ so that one can combine equations (4.1) and (4.2), eliminating C_n and write I_n and I_{rn} in terms of I

$$I \approx \frac{r^k I_{rn} - I_n}{r^k - 1}, \tag{4.3}$$

giving Richardson's extrapolated value ($I \approx R_{ext}$). Defining the error on the refined grid as

$$E_{rn} = \left| R_{ext} - I_{rn} \right|, \tag{4.4}$$

and replacing R_{ext} using equation (4.3) the Richardson error estimate is written as

$$E_{rn} = \left| \frac{I_n - I_{rn}}{r^k - 1} \right|. \tag{4.5}$$

Note that the Richardson error estimate can be applied to global (e.g. force, momentum) as well as local (e.g. pressure, velocity) quantities obtained in the solution. In equation (4.5) only the algorithm rate of convergence k cannot be directly obtained from the runs. Roache [63] provides a result to establish the rate of convergence of an algorithm using three grids with two grid refinement ratios r_1 and r_2:

$$\frac{\epsilon_{1,2}}{r_1^k - 1} = r_2^k \left[\frac{\epsilon_{2,3}}{r_2^k - 1} \right], \tag{4.6}$$

where refinement ratio $r_1 = \frac{n_2}{n_1}$, $r_2 = \frac{n_3}{n_2}$ with $r_1 \neq r_2$ and k is the algorithmic rate of convergence. In this notation grid 1 is the coarsest and grid 3 the finest. Equation (4.7) defines ϵ

$$\epsilon_{i,i+1} = \phi_{i+1} - \phi_i, \tag{4.7}$$

where $i = 1, 2$ for the global or local flow property ϕ. Equation (4.6) does not lend itself to a direct solution, so the following iterative procedure proposed by Roache [63] is used:

$$k = \omega\rho + (1 - \omega)\,\frac{\ln \beta}{\ln r_2} \tag{4.8a}$$

$$\beta = \frac{r_2^\rho - 1}{r_1^\rho - 1} \left(\frac{\epsilon_{1,2}}{\epsilon_{2,3}} \right) \tag{4.8b}$$

where $\rho = k_{previous}$ and $\omega = 0.5$ is a relaxation parameter. Upon implementation of the procedure defined by equation (4.8) with the software package *MATLAB*, the mean order of convergence k of the algorithm was established as $k = 1.87$.

For the purpose of this study the error is nondimensionalised as

$$\epsilon' = \frac{\phi_{current} - \phi_{reference}}{\phi_{reference,max}}, \tag{4.9}$$

as the Richardson error estimate does not reflect the over- or underestimation of flow quantities. This information is of significance when determining the suitability of a grid for sloshing studies. The mean, rectified error for n pressure differences ΔP_i is defined as

$$\overline{\epsilon}' = \frac{1}{n} \sum_{i=1}^{n} |\Delta P_i| \,, \tag{4.10}$$

so that there is no cancellation between over and underestimated data. In addition, the root mean square of the error, defined by

$$\overline{\epsilon}'_{rms} = \sqrt{\frac{1}{n} \sum_{i=1}^{n} (\Delta P_i)^2}, \tag{4.11}$$

is used to focus more severe error regions.

4.4 Results

4.4.1 Grid 1

Figure 4.3 shows the pressure histories at P4, P6 and P9 for grid 1. Even though grid 1 was the coarsest, the results appear consistent with the physics of the problem. In the transient phase lasting about ten sloshing oscillations, the pressure at P4 is consistent with the water striking the north wall. After 20 sloshing periods the flow has reached a steady periodic state. The peak pressure in figure 4.3(a) remains close to 1200 N/m^2, while P6 settles at around 350 N/m^2.

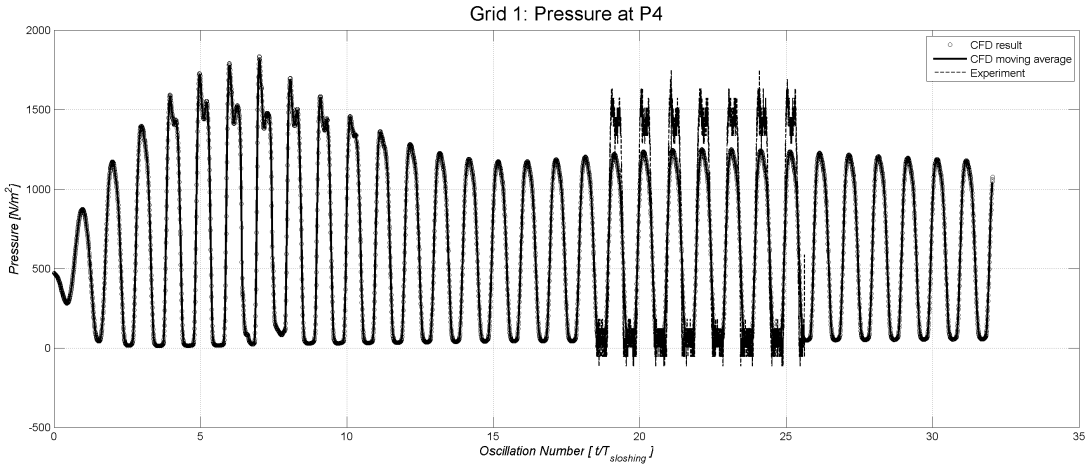

4.3(a): Pressure at P4

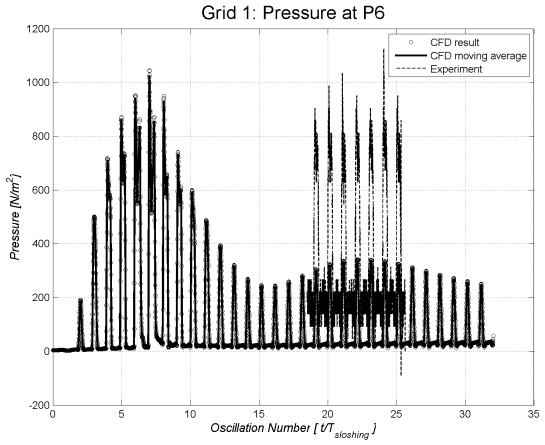

4.3(b): Pressure at P6

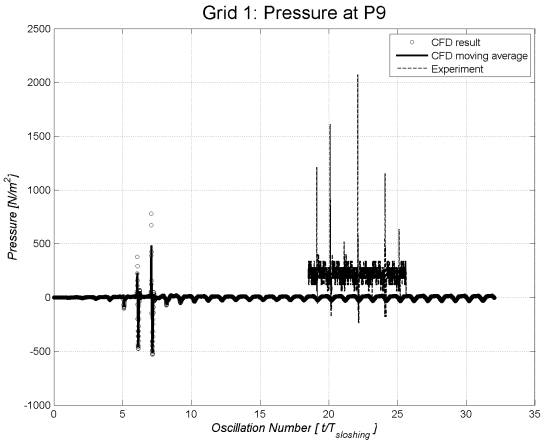

4.3(c): Pressure at P9

Figure 4.3: Pressure [N/m^2] at control points using grid 1

The computational data compares rather poorly with the steady-state experimental data, even when considering the discussion in section 3.5.2. The best correlation is observable at P4, the pressure at P6 is underestimated by about 50%. Comparing the computational result with the experimental result at P9, one finds little agreement between the data. In the CFD results, the water does not reach the North wall in the steady state phase, while the experimental results indicate very short-term pressure peaks. The period of oscillation is maintained throughout the CFD simulation, as shown in figure 4.3(a).

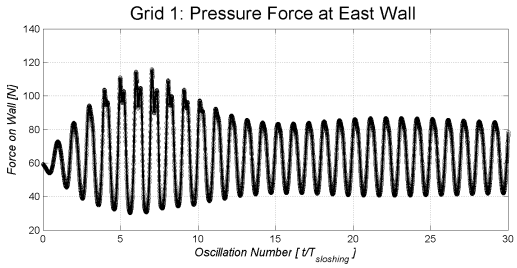

4.4(a): Force at East Wall

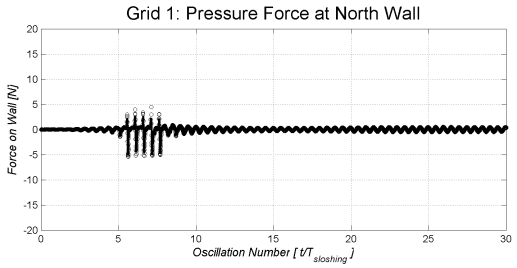

4.4(b): Force at North Wall

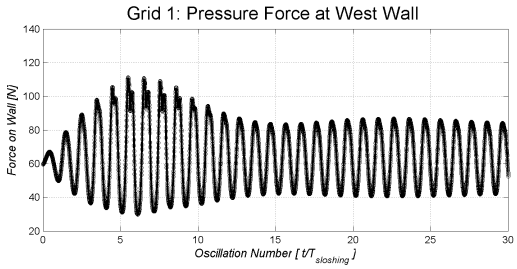

4.4(c): Force at West Wall

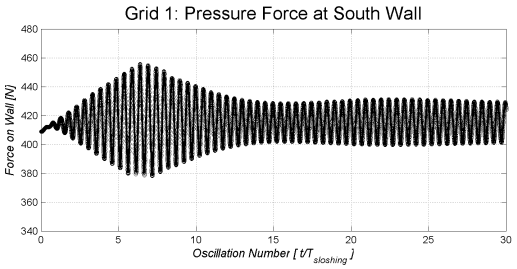

4.4(d): Force at South Wall

Figure 4.4: Pressure force on sloshing container [N] using grid 1

As can be seen in figure 4.4, the force plots reach a steady state as well. The forces at the East and West walls, given in figures 4.4(a) and 4.4(c) respectively, are anti-symmetric as expected. The conservation properties of this simulation are quite acceptable, as the mass and momentum imbalances are less than 1%. The maintenance of the correct amount of fluid in the tank is crucial to the success of the simulation, as natural sloshing frequency and hence wall pressure are directly influenced by the filling level. Precise numerical values as well as a summary of the parameters used are given in table 4.2. The imbalance rates are sufficiently low to permit further continuation of the run.

Table 4.2: Summary of grid convergence study, grid 1

Grid Independence Run 1: Summary	
Run Setup	
Grid Nodes	6000
Transient Time [s]	45.0
Required Computational Time [hrs]	41.33
Simulation time per hour CPU* $[\frac{sec}{hr}]$	1.089
*2.2 GHz, 64 bit processor with 2 GB RAM	
CFX Settings	
Fluid Models	Air ... Compressible
	Water ... Incompressible
Flow Type	Turbulent ($k-\epsilon$ turbulence model)
Spatial Discretisation	Second Order Upwind
Transient Scheme	First Order Euler
Convergence Criteria	Residual RMS $5 \cdot 10^{-5}$
Numerical Precision	Double
Conservation of Mass	
Imbalance, % of original	-0.1603
Imbalance per Simulated Second $[\frac{kg}{sec}]$	$-4.38 \cdot 10^{-3}$ (mean)
Conservation of Momentum	
X-dir Imbalance, % of original	$-3.447 \cdot 10^{-3}$
Imbalance per Simulated Second $[\frac{kg \cdot m \cdot sec^{-1}}{sec}]$	$-1.348 \cdot 10^{-4}$ (mean)
Z-dir Imbalance, % of original	$2.573 \cdot 10^{-3}$
Imbalance per Simulated Second $[\frac{kg \cdot m \cdot sec^{-1}}{sec}]$	$6.775 \cdot 10^{-5}$ (mean)

4.4.2 Grid 2

Grid 2 is more than double the total number nodes of grid 1 and it increases the required computational resources by a factor of approximately two. The transient pressure phase at P4, delineated in figure 4.5(a) is similar to the one observed in the coarse grid 1, shown in figure 4.3(a). However, the pressure peaks at P6 and P9, given in figures 4.5(b) and 4.5(c)

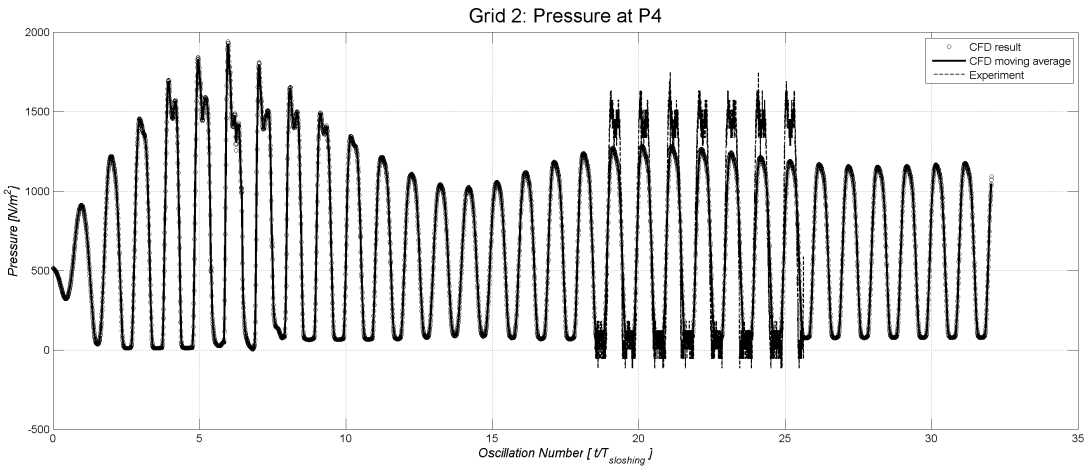

4.5(a): Pressure at P4

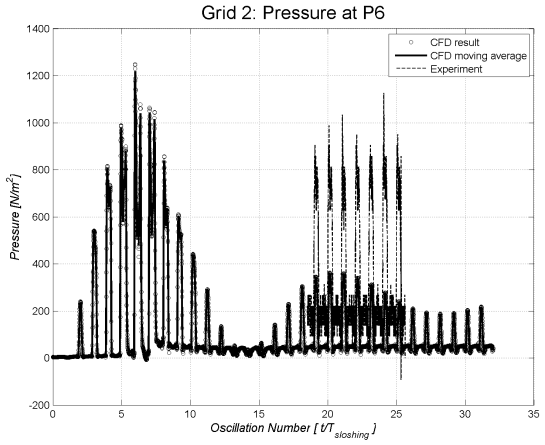

4.5(b): Pressure at P6

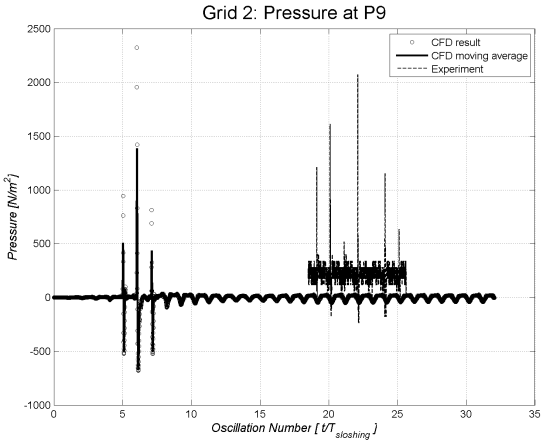

4.5(c): Pressure at P9

Figure 4.5: Pressure [N/m^2] at control points using grid 2

respectively, are significantly higher with grid 2. Further, the transition from transient to steady state is more pronounced in the present case as seen in the trough in peak pressure at oscillation 12 and 13. The comparison with experimental data is again rather poor, with qualitative differences similar to the previous grid 1. The pressures in the transient phase (the first 10 oscillations) are higher than in figure 4.3, with an increase at P6 of about 20% of the peak pressure at oscillation six. This makes the grid-dependence of the solution obtained in grid 1 apparent, indicating that grid 1 is unsuitable for further use.

The force plots in figure 4.6 are similar to the previous case, reaching a steady state once the flow has progressed past 20 oscillations. Grid 2 takes longer to progress to a steady state

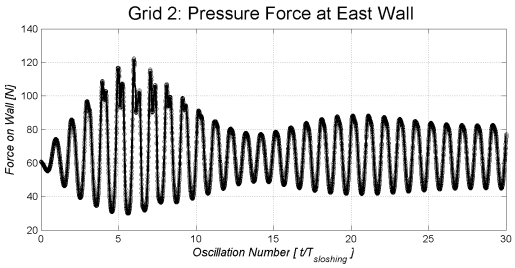

4.6(a): Force at East Wall

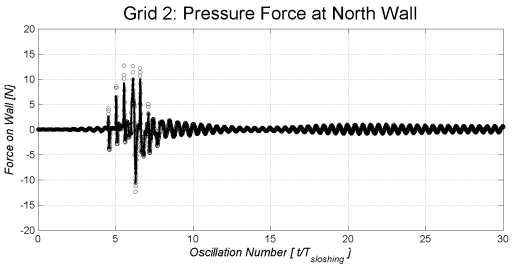

4.6(b): Force at North Wall

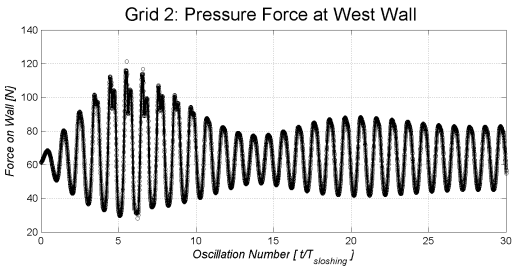

4.6(c): Force at West Wall

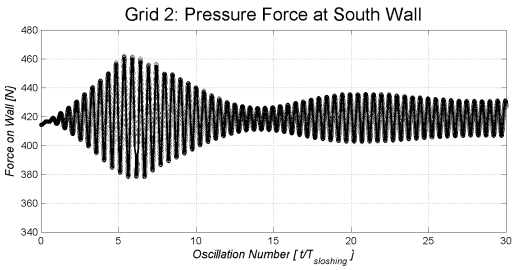

4.6(d): Force at South Wall

Figure 4.6: Pressure force on sloshing container [N] using grid 2

than the previous grid 1 and the second transient phase is well defined. The transient sloshing force is higher than with grid 1, as might be expected from the previous pressure observations. The conservation properties given in table 4.3 are similar to the previous grid 1, indicating that despite the coarse discretisation the numerical methods used are sufficiently accurate to maintain conservation of mass and momentum.

Table 4.3: Summary of grid convergence study, Grid 2

Grid Independence Run 2: Summary	
Run Setup	
Grid Nodes	12000
Transient Time $[sec]$	45.0
Required Computational Time $[hrs]$	99.26
Simulation time per hour CPU* $[\frac{sec}{hr}]$	0.456
*2.2 GHz, 64 bit processor with 2 GB RAM	
CFX Settings	
Fluid Models	Air ... Compressible
	Water ... Incompressible
Flow Type	Turbulent ($k-\epsilon$ turbulence model)
Spatial Discretisation	Second Order Upwind
Transient Scheme	First Order Euler
Convergence Criteria	Residual RMS $5 \cdot 10^{-5}$
Numerical Precision	Double
Conservation of Mass	
Imbalance, % of original	-0.1619
Imbalance per Simulated Second $[\frac{kg}{sec}]$	$-3.633 \cdot 10^{-3}$ (mean)
Conservation of Momentum	
X-dir Imbalance, % of original	$-1.801 \cdot 10^{-2}$
Imbalance per Simulated Second $[\frac{kg \cdot m \cdot sec^{-1}}{sec}]$	$-4.778 \cdot 10^{-4}$ (mean)
Z-dir Imbalance, % of original	$-3.031 \cdot 10^{-2}$
Imbalance per Simulated Second $[\frac{kg \cdot m \cdot sec^{-1}}{sec}]$	$7.111 \cdot 10^{-4}$ (mean)

4.4.3 Grid 3

Grid 3, encompassing 28000 nodes, provides additional spatial resolution. However, the increase in required time steps due to reduction in grid spacing reduces the conservation properties of mass and momentum, given in table 4.4 considerably. The steady state pressure at P4 depicted in figure 4.7(a) shows the split peak observed in experimental studies. The

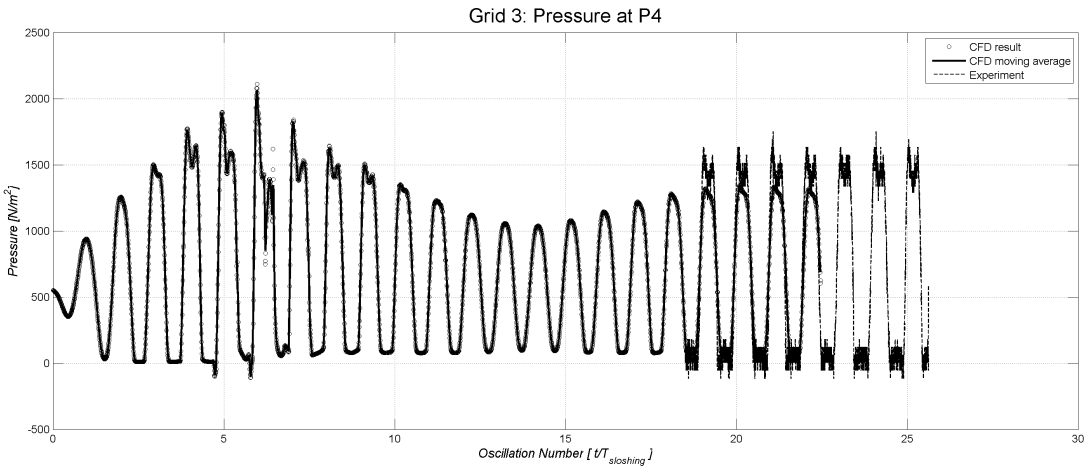

4.7(a): Pressure at P4

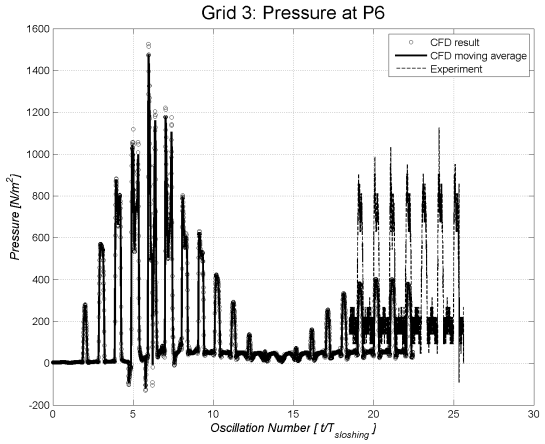

4.7(b): Pressure at P6

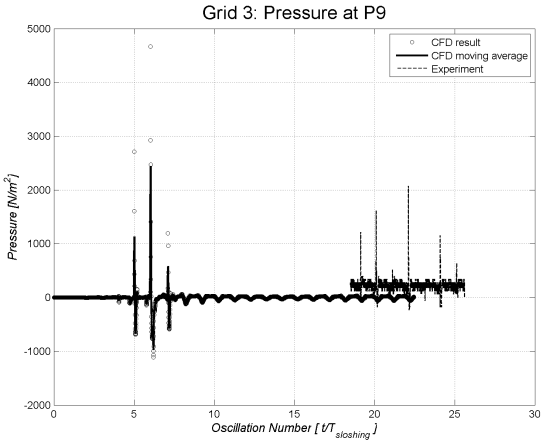

4.7(c): Pressure at P9

Figure 4.7: Pressure [N/m^2] at control points using grid 3

transient peaks at P4 and P6, shown in figure 4.7(b) are about 10% higher than with grid 2. Note the large spike in the pressure history of P9 between oscillations 5 to 7 displayed in figure 4.7(c). Further, one may note the absence of the secondary peak at oscillation 15, the pressure obtained with grid 3 progresses directly to the steady state. Considering the experimental data in figure 4.7(a), there is better agreement than with previous grids, as the pressure disagreement at P4 is in the regions of oscillating experimental data. Again, the pressures at locations P6 and P9 do not match the experimental data any better. The pressure peak in the transient region has increased again compared to grid 2, the steady-state solution is similar in grids 2 and 3. The pressure and force histories obtained with grid 3

match those from grid 2 better than those from grid 1, indicating the result is now less grid dependent.

The force plots in figure 4.8 are slightly higher than in the previous grid 2 (figure 4.6). Also note the typical sloshing peaks shown at the anti-symmetric East and West walls illustrated in figures 4.8(a) and 4.8(c) respectively. Mass and momentum conservation are satisfactory for this run. However, the mass residual given in table 4.4 appears slightly larger than expected. The computational requirements have increased significantly compared to grids 1 and 2, with the simulated second per CPU hour decreasing by about 90% to nearly 0.12 sec/hr. Shown later in figure 4.11 is the free surface position throughout the simulation. The free surface elevation correlates well to the pressure graphs, illustrating the significance of the static pressure component.

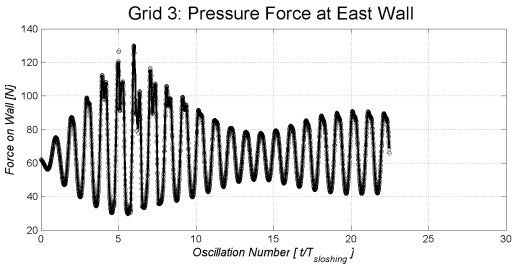

4.8(a): Force at East Wall

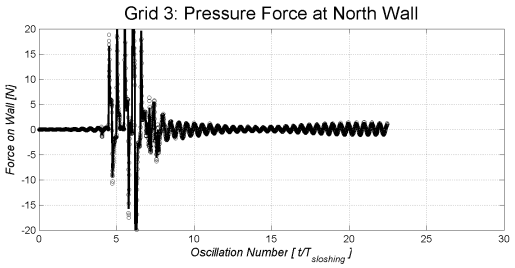

4.8(b): Force at North Wall

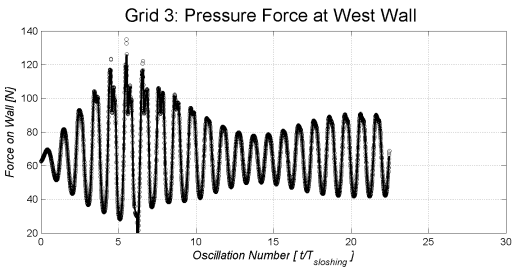

4.8(c): Force at West Wall

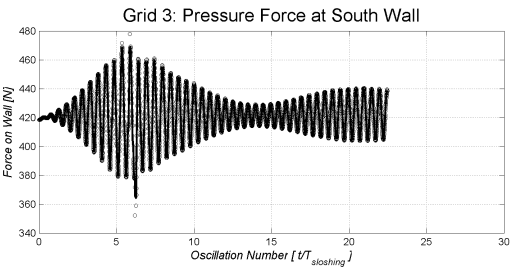

4.8(d): Force at South Wall

Figure 4.8: Pressure force on sloshing container [N] using grid 3

Table 4.4: Summary grid convergence study, grid 3

Grid Independence Run 3: Summary	
Run Setup	
Grid Cells	28000
Transient Time $[sec]$	32.0
Required Computational Time $[hrs]$	260.53
Simulation time per hour CPU* $[\frac{sec}{hr}]$	0.123
*2.2 GHz, 64 bit processor with 2 GB RAM	
CFX Settings	
Fluid Models	Air ... Compressible
	Water ... Incompressible
Flow Type	Turbulent ($k-\epsilon$ turbulence model)
Spatial Discretisation	Second Order Upwind
Transient Scheme	First Order Euler
Convergence Criteria	Residual RMS $5 \cdot 10^{-5}$
Numerical Precision	Double
Conservation of Mass	
Imbalance, % of original	5.234
Imbalance per Simulated Second $[\frac{kg}{sec}]$	$1.636 \cdot 10^{-1}$ (mean)
Conservation of Momentum	
X-dir Imbalance, % of original	$-8.987 \cdot 10^{-3}$
Imbalance per Simulated Second $[\frac{kg \cdot m \cdot sec^{-1}}{sec}]$	$-2.808 \cdot 10^{-4}$ (mean)
Z-dir Imbalance, % of original	$4.083 \cdot 10^{-3}$
Imbalance per Simulated Second $[\frac{kg \cdot m \cdot sec^{-1}}{sec}]$	$1.276 \cdot 10^{-4}$ (mean)

4.4.4 Grid 4

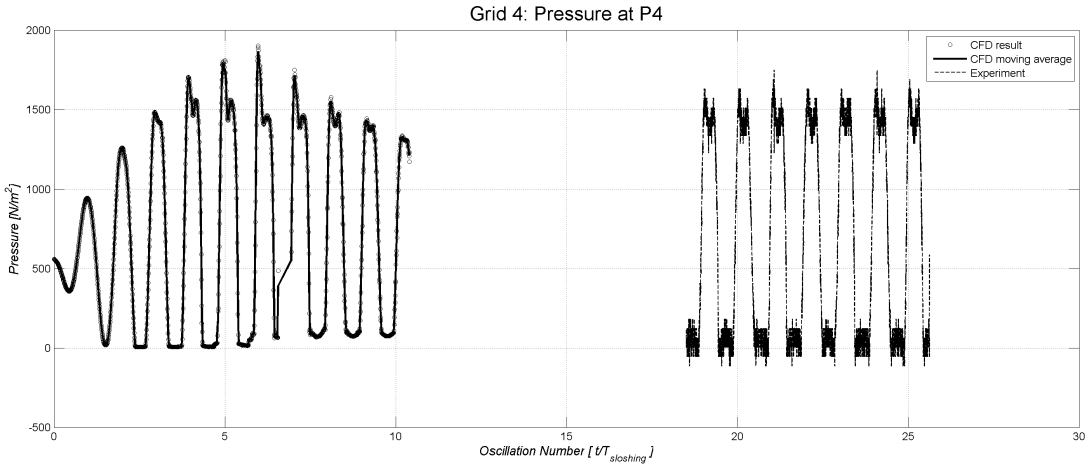

4.9(a): Pressure at P4

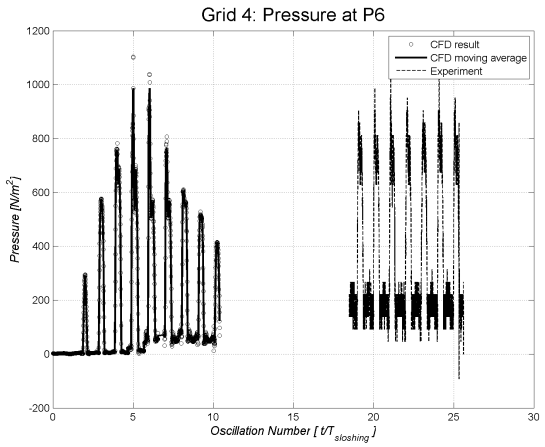

4.9(b): Pressure at P6

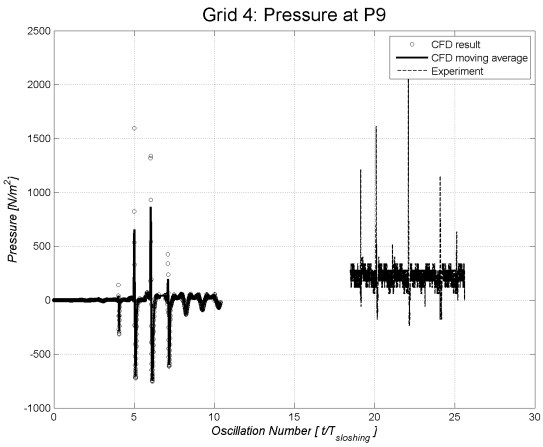

4.9(c): Pressure at P9

Figure 4.9: Pressure [N/m^2] at control points using grid 4

Grid 4 is the finest grid used for the grid independence study, and it is evident that it is not suitable for practical applications due to the significant computational requirements. Thus only a limited time history is available. Nonetheless, the transient region can still be used as a basis for assessment. It compares well, both when considering the pressure peaks given in figure 4.9 as well as the local negative pressures observable in the transient regions between oscillations 4 and 6, to the previous grid 3. Note that the transient peaks at P6, shown in figure 4.9(b), are lower than those observed using grid 3.

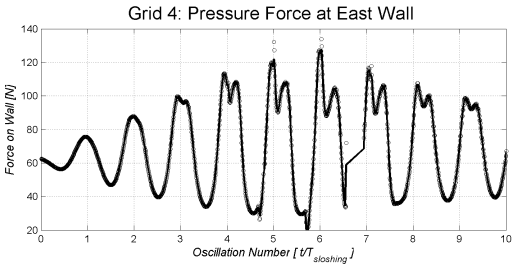

4.10(a): Force at East Wall

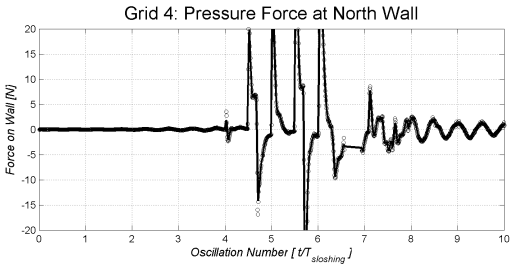

4.10(b): Force at North Wall

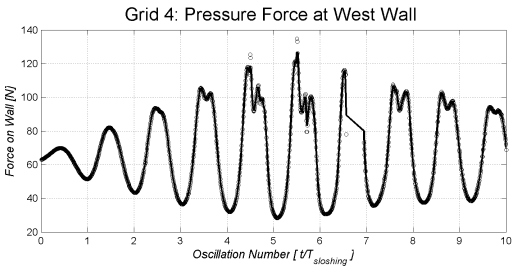

4.10(c): Force at West Wall

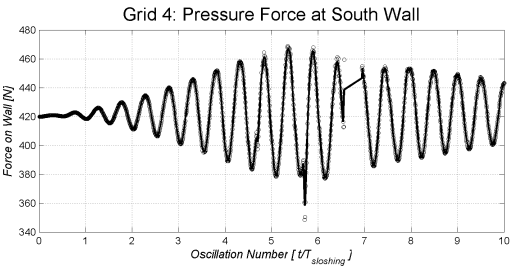

4.10(d): Force at South Wall

Figure 4.10: Pressure force on sloshing container [N] using grid 4

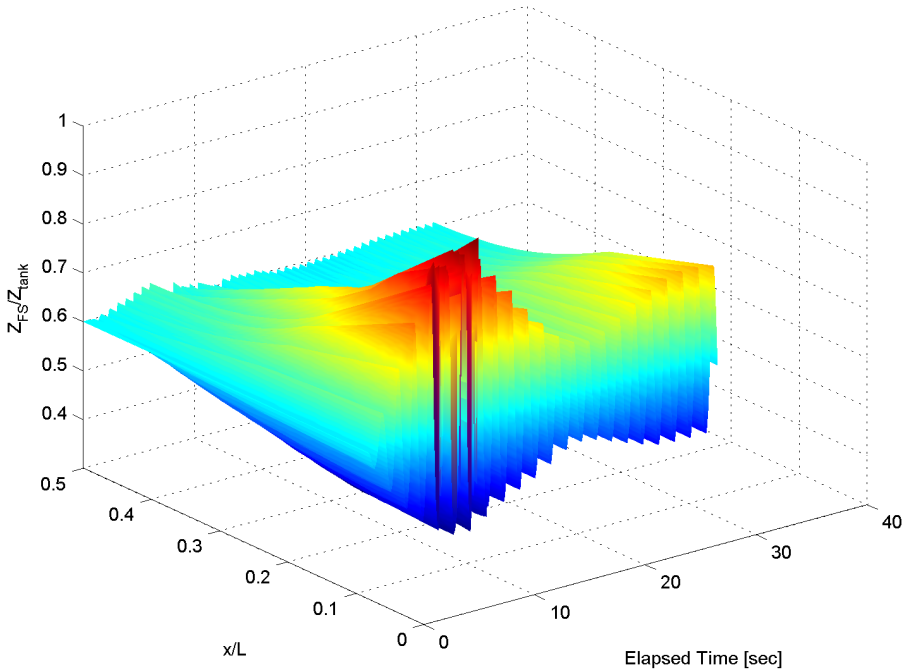

Figure 4.11: Typical free surface time evolution

Table 4.5: Settings for grid convergence study, grid 4. *Residual data not available due to short run*

Grid Independence Run 4: Summary	
Run Setup	
Grid Cells	56000
Transient Time $[sec]$	9
Required Computational Time $[hrs]$	140.15
Simulation time per hour CPU* $[\frac{sec}{hr}]$	0.064
*2.2 GHz, 64 bit processor with 2 GB RAM	
CFX Settings	
Fluid Models	Air ... Compressible
	Water ... Incompressible
Flow Type	Turbulent ($k-\epsilon$ turbulence model)
Spatial Discretisation	Second Order Upwind
Transient Scheme	First Order Euler
Convergence Criteria	Residual RMS $5 \cdot 10^{-5}$
Numerical Precision	Double

Comparing the computational results to the experimental data, it is apparent that they do not match in the steady state. The static pressure appears to be predicted correctly when comparing the water surface elevation to the discussion in section 3.5.1. However, the experimental pressure readings indicate water impacting the North wall but this is not observed in the computational study. In summary, the results do not match the experimental data as well as one would expect, but the results appear to be independent of the computational grid. Therefore, the current combination of parameters is not sufficient for simulating violent sloshing. This is considered in greater detail in section 8. The next section gives an analysis of the results using the theory outlined in section 4.3 to formally establish grid independence

4.5 Analysis

4.5.1 Error Results: Reference Grid 4

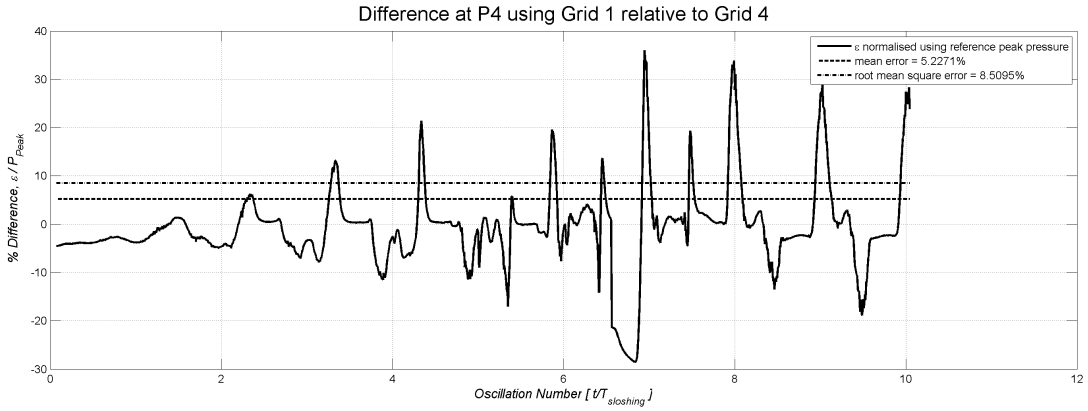

4.12(a): Pressure difference observed with grid 1

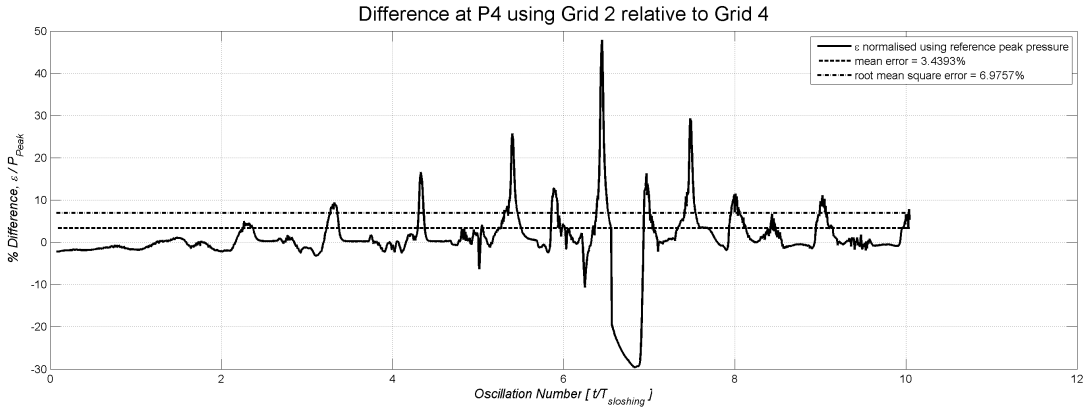

4.12(b): Pressure difference observed with grid 2

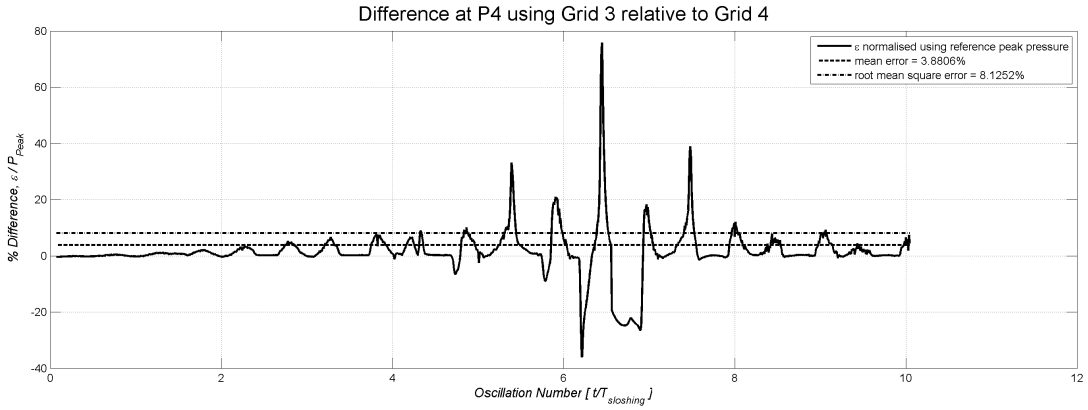

4.12(c): Pressure difference observed with grid 3

Figure 4.12: Pressure difference at P4 using increasing grids relative to grid 4

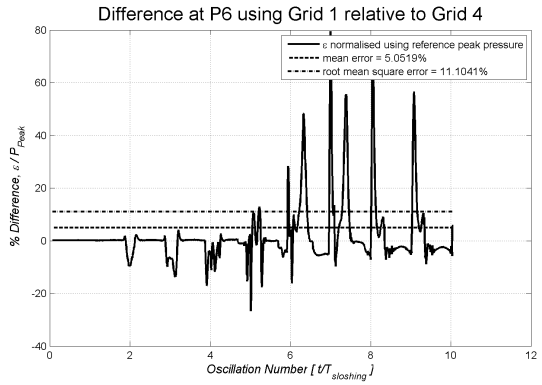

4.13(a): Pressure difference at P6 with grid 1

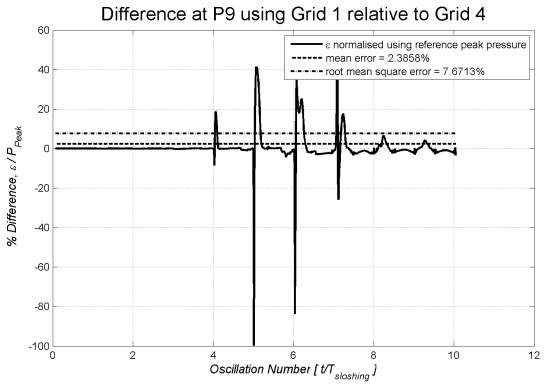

4.13(b): Pressure difference at P9 with grid 1

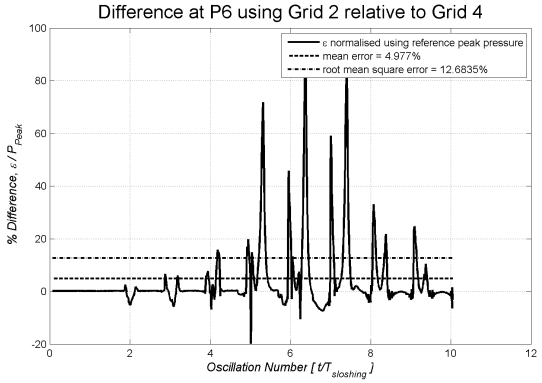

4.13(c): Pressure difference at P6 with grid 2

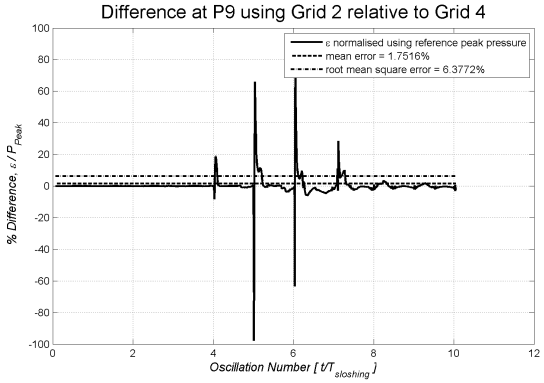

4.13(d): Pressure difference at P9 with grid 2

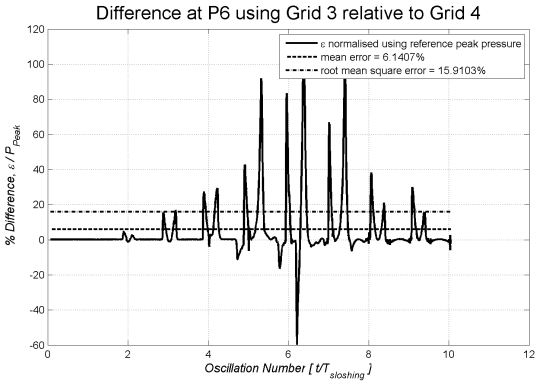

4.13(e): Pressure difference at P6 with grid 3

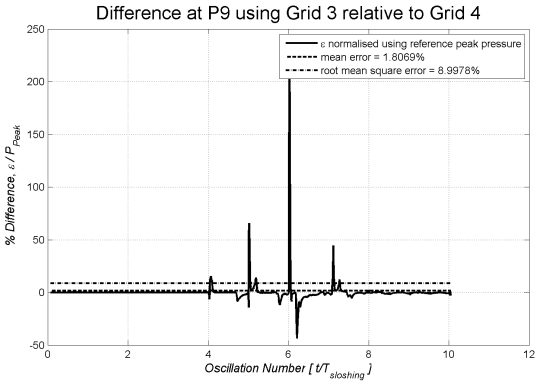

4.13(f): Pressure difference at P9 with grid 3

Figure 4.13: Pressure difference at P6 (left column) and P9 (right column) using increasing grids relative to grid 4

As noted previously, the order of convergence of the present algorithm was established as $k = 1.87$ using grids 2, 3 and 4 (specified in table 4.1, section 4.2). The computed convergence

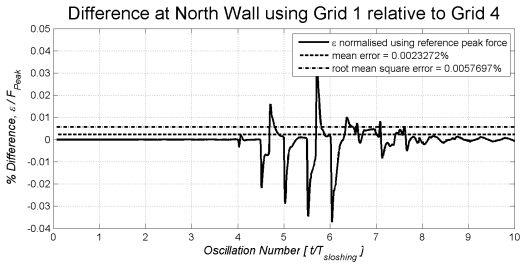

4.14(a): % Difference at North Wall with grid 1

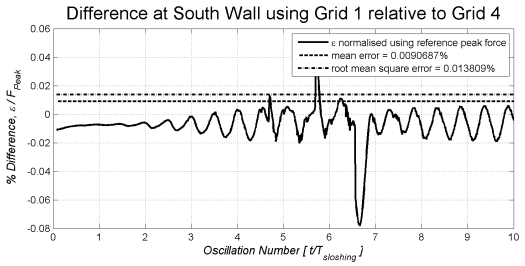

4.14(b): % Difference at South Wall with grid 1

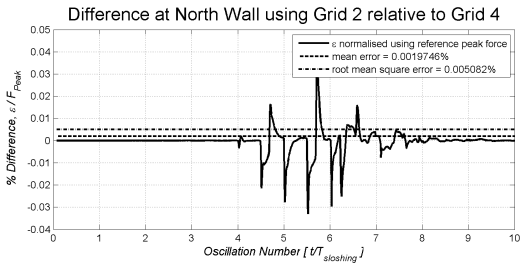

4.14(c): % Difference at North Wall with grid 2

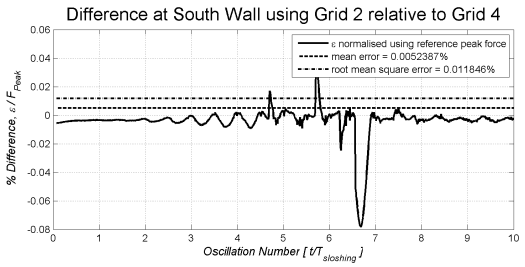

4.14(d): % Difference at South Wall with grid 2

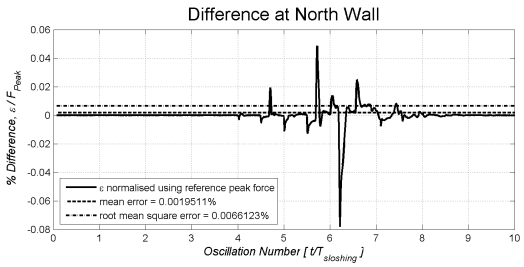

4.14(e): % Difference at North Wall with grid 3

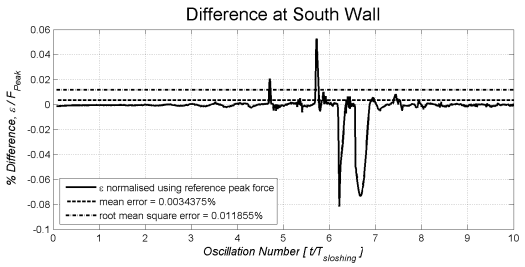

4.14(f): % Difference at South Wall with grid 3

Figure 4.14: Pressure force differences with reduced grid spacing at North (left column) and South (right column) wall

rate compares well to the typically expected value of $k \approx 2$. However, this result should be treated with some caution, as the current procedure is intended primarily for steady state solutions.

When solving an unsteady problem small changes in the solution may be amplified over time, depending on the specific problem and fluid models [64]. The direct comparison between pressure and force histories is more conclusive, as differences between individual simulations are readily identified. In the current case the pressure force is used to compare integral quantities on the boundaries of the solution.

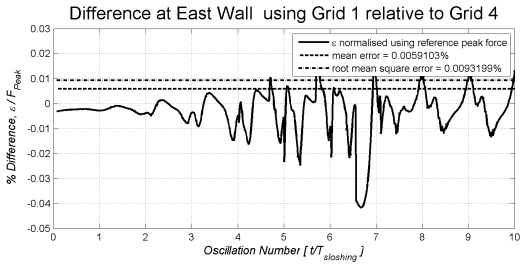

4.15(a): % Difference at East Wall with grid 1

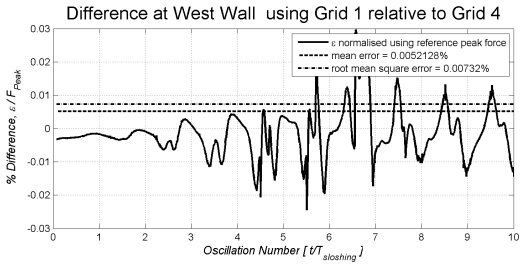

4.15(b): % Difference at West Wall with grid 1

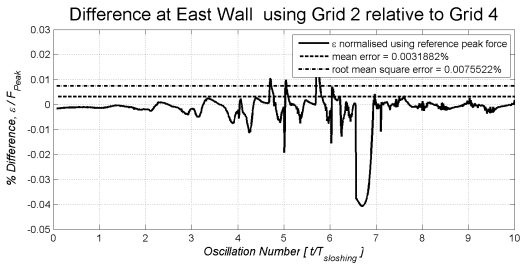

4.15(c): % Difference at East Wall with grid 2

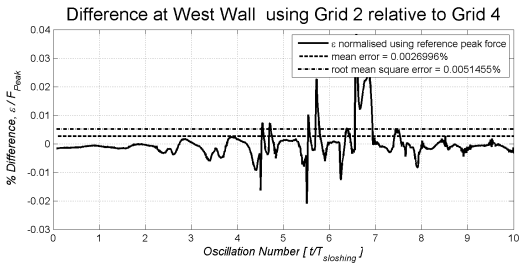

4.15(d): % Difference at West Wall with grid 2

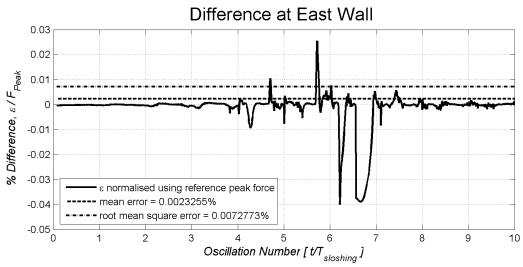

4.15(e): % Difference at East Wall with grid 3

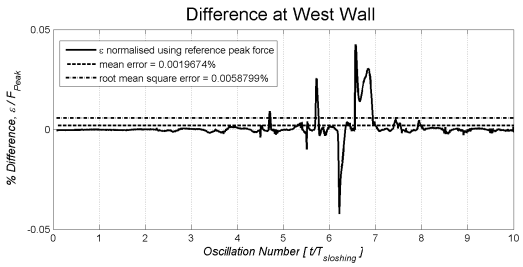

4.15(f): % Difference at West Wall with grid 3

Figure 4.15: Pressure force difference with reduced grid spacing at East (left column) and West (right column) wall

Considering the differences at P4 relative to grid 4 in figure 4.12 it is apparent that the result converges satisfactorily as the number of grid cells is increased. While the difference between grid 1 and grid 4 illustrated in figure 4.12(a) often exceeds 10% for periods of up to 1 sec, the same error is reduced when employing grid 3 to peaks generally not exceeding 5% in figure 4.12(c). While the RMS error for grid 3 in figure 4.12(c) is greater than for grid 1, the differences become sharper and are confined to the period of the most violent sloshing between oscillations 5 to 8. Similar behaviour is observed at P6 in figure 4.13. The mean error is about 5%, depending on the observation point. However, the errors at P9 are not very suitable for comparison. Note that the peak pressure at P9 is $O\,(10N)$ while at P4 it is $O\,(1000N)$. The mean error between grids 1 and 4 is in excess of 5%, while grid 2 or 3

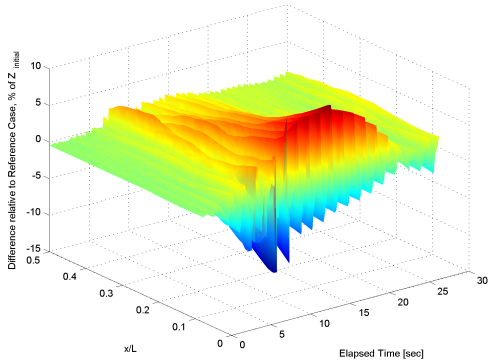

4.16(a): Difference in free surface observed using grid 1 relative to grid 3: mean error 1.452%

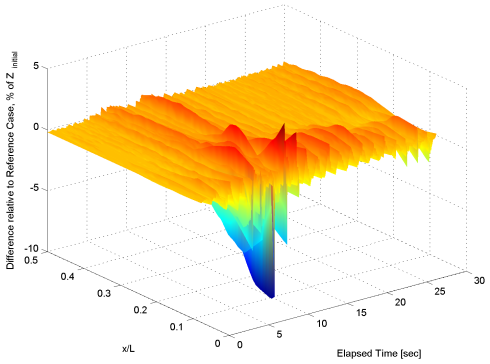

4.16(b): Difference in free surface observed using grid 2 relative to grid 3: mean error 0.405 %

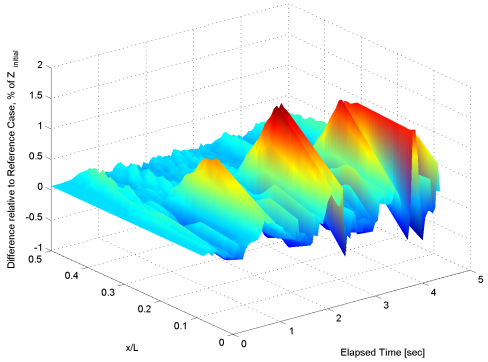

4.16(c): Difference in free surface observed using grid 3 relative to grid 4: mean error 0.204 %

Figure 4.16: Difference in free surface relative to grid 4

differ by a mean of approximately 3.5% at P4. A similar trend is observed at P9, and to a lesser extent at P6. One may note that the most significant error is in the transient phase. Once the solution progresses towards the steady state, the error is reduced as grid spacing is reduced.

When considering the pressure integral, grid convergence becomes more readily apparent. While the mean error decreases between grids 1 and 2 significantly (a reduction of approximately 50% may be observed), there is very little change between grids 2 and 3. One may again note that the error is confined to a short interval, with decreasing error once the solution progresses past the transient phase.

Grid number 2 is significantly better than the previous grid, as both the magnitude and summations of errors are reduced considerably. The most noticeable improvement is on the East and West walls, given in figures 4.15(c) and 4.15(d) respectively. The error does not exceed 0.05% except for a few spikes. The error periods are shorter than in the previous figure 4.14. The same may be observed at the South wall in figure 4.14(d), while the North wall difference remains inconclusive for reasons stated earlier. The difference in wall force between grids 3 and 4 is similar to that obtained between grids 2 and 4. A similar trend is delineated in figure 4.14(f) for the South wall.

The free surface locations, illustrated in figures 4.16(a) to 4.16(c) are more suitable for assessing the convergence of the algorithm. Note that only half the region $0.0 \leq x/L \leq 0.5$ is displayed. In figure 4.16(a) there is a considerable difference in free surface between grid 1 and 3, with a peak of $\pm 10\%$. There is a marked improvement when using grid 2 as depicted in figure 4.16(b), with good agreement in the steady state region. Finally, comparing grid 3 and 4, there is very little difference between the two grids, with a mean error of 0.204%.

4.5.2 Error Results: Reference Grid 3

Given the reduced time history with grid 4 and the generally good correlation between grids 3 and 4, a comparison relative to grid 3 over a longer period is carried out as well. However, only the pressure data will be considered as the pressures appeared to be more sensitive to grid variations than the wall force in the previous section.

Considering the data over a longer timescale, one may observe better convergence once the simulation progresses past 10 oscillations. For such long time simulations, the conservation of mass and momentum is important. As this was confirmed earlier, the result obtained using grid 2 with a mean error of 1.5% is superior to that of grid 1 with a mean error of 5%. The root mean square error is reduced as well.

As the steady state region is the basis for comparison, a larger transient error may be more acceptable than the persistent error in the steady state. Note that the steady state error past 19 oscillations is of similar shape in both grids, but the magnitude is reduced by a constant

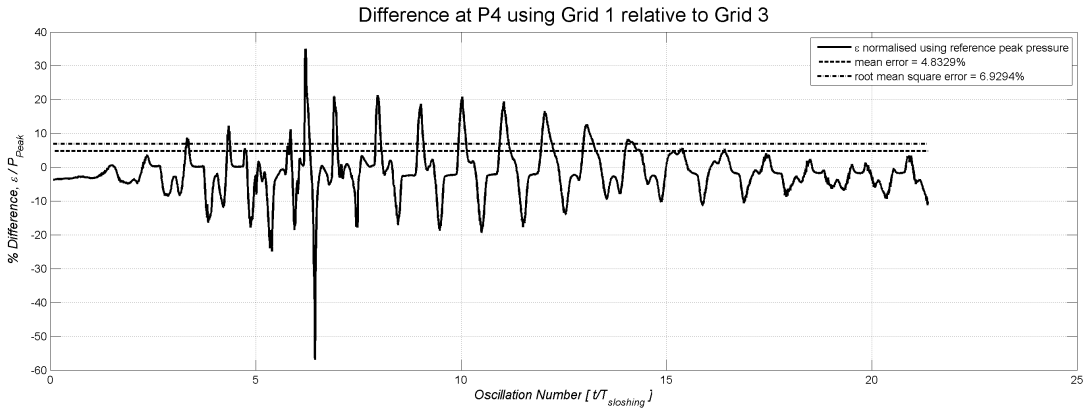

4.17(a): Grid 1 relative to Grid 3

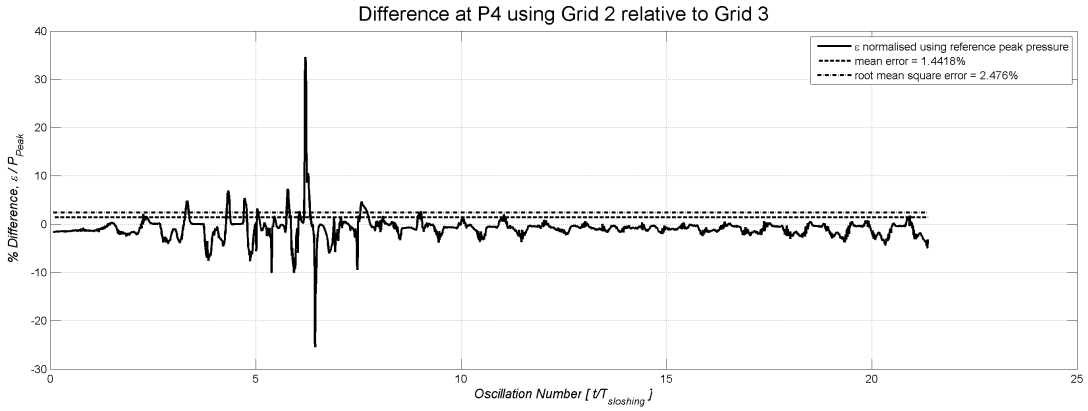

4.17(b): Grid 2 relative to Grid 3

Figure 4.17: Pressure differences at P4 relative to grid 3

- as expected from equation (4.5). The trend of a reduced error in the steady state phase shown in the previous analysis is confirmed in this section.

Figure 4.18 shows a similar trend to the pressure history at P4, a larger transient error and good agreement between the grids once a steady state is reached. The constant error reduction once the time history has moved past 15 oscillations is again observable. Finally, the pressure at P9 shows the same trend, with a comparatively small mean error, especially in the steady state.

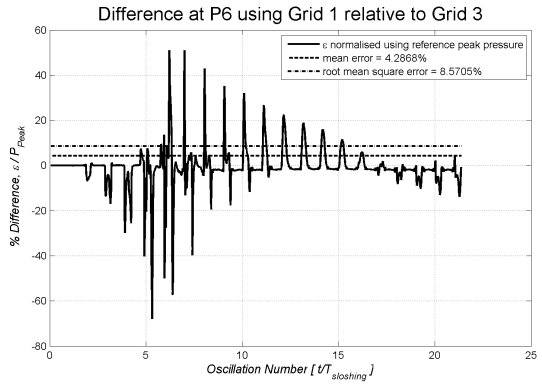

4.18(a): Grid 1 relative to Grid 3

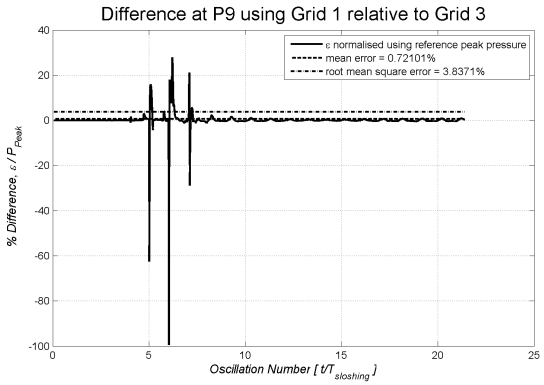

4.18(b): Grid 1 relative to Grid 3

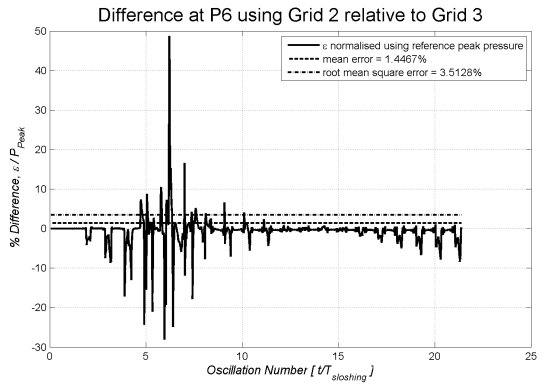

4.18(c): Grid 2 relative to Grid 3

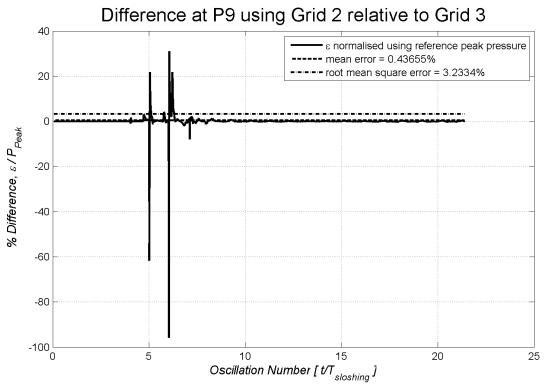

4.18(d): Grid 2 relative to Grid 3

Figure 4.18: Pressure differences at P6 (left column) and P9 (right column) relative to grid 3

4.6 Grid Generation Recommendations

The two preceding sections 4.5.1 and 4.5.2 have been very instructive in assessing the grid independence of this particular sloshing flow. One can conclude that from grid 2 onwards the discretisation errors are sufficiently small to be negligible. Grid 4 gives more physically consistent peaks than grid 2, however the computational penalty is huge - the same run would take more than ten times as long and take up correspondingly more storage space. Thus, the bulk of required CFD simulations for this problem should be carried out on grid 2, with occasional confirmation on grid 3. Table 4.6 summarises the computed errors between grids. The pressure force, in particular, shows less grid dependence as the grid resolution is increased.

It should be emphasised at this point that a more severe sloshing flow, or any significant change in geometry requires another grid independence study. Further, one should note that the transient region by itself is a poor basis for predicting the convergence properties of a CFD sloshing simulation. Given the chaotic nature of sloshing when the excitation frequency is near the natural frequency [29], the effect of random disturbances induced by finite numerical precision may require further consideration.

Table 4.6: Summary of results analysis for grid independence. * Force error data not available

Model	**Reference**	**Pressure**			**Wall Pressure Force**			
		P4 [%]	P6 [%]	P9 [%]	North [%]	East [%]	South [%]	West [%]
Grid 1	Grid 4	5.23	5.05	2.39	0.0023	0.0059	0.0091	0.0052
	(RMS)	8.51	11.1	7.67	0.0057	0.0093	0.0138	0.0073
Grid 2	Grid 4	3.44	4.98	1.75	0.0020	0.0032	0.0052	0.0027
	(RMS)	6.98	12.7	6.38	0.0051	0.0076	0.0118	0.0051
Grid 3	Grid 4	3.88	6.14	1.81	0.0019	0.0023	0.0034	0.0020
	(RMS)	8.13	15.9	9.00	0.0066	0.0072	0.0119	0.0059
Grid 1*	Grid 3	4.83	4.29	0.72				
	(RMS)	6.93	8.57	3.84				
Grid 2*	Grid 3	1.44	1.45	0.44				
	(RMS)	2.48	3.51	3.23				

Despite grid independence having been demonstrated, the sloshing pressures were consistently underestimated when compared to the experimental data from Hinatsu[2]. It is noteworthy that the disagreement between the computational and experimental results grows as the influence of the gaseous phase becomes more important. However, given that air is already modelled as the more complex compressible fluid, there may be other error sources as well.

The best compromise between computational cost and result quality appears to be grid 2. Thus, for a problem of comparable size, a grid of about 6000 elements, with an initial wall

spacing of 1 mm appears appropriate. It should be noted that one cannot directly scale the grid when considering a larger geometry. Nonetheless, the preceding grid independence study offers useful guidance for grid generation of sloshing grids.

1. The offset of the first grid point from the wall is sufficiently small at 1 mm. Later studies, using an 0.3 mm offset in section 6.3.1, confirm this. The limiting factor is usually the aspect ratio of the near-wall cells.

2. The full range of sloshing motion was captured well with a 100 by 80 cell grid. Provided the sloshing fluid is geometrically similar at larger scales, this may give an indication as to the grid refinement within the tank, but not near the walls.

3. Spatial and second order temporal discretisation is accurate on a coarse grid, indicating that for full-scale sloshing applications a hybrid grid may be the best-suited design compromise

5 Timestep

5.1 Background

The nature of the sloshing problem requires transient modelling as the flow will not attain a steady state as is the case for most CFD problems [50]. Thus, the time derivative in the governing equations (3.1) or (3.2) has to be discretised as well. Including time as a variable adds another dimension to the problem and increases the computational requirements accordingly. Finally, it is an additional source for mass and momentum dissipation, mandating the thorough examination of any results to ascertain the conservation properties.

CFX-10 offers two different time discretisation schemes [51], a first order and second order backward Euler scheme. The first order scheme approximates the time derivatives in integral form,

$$\frac{\partial}{\partial t}\int_V \rho\phi \; dV, \tag{5.1}$$

using a first order scheme for the time derivative given by

$$\frac{\partial \phi}{\partial t} = \frac{\phi_i - \phi_{i-1}}{\Delta t}, \tag{5.2}$$

where i is the current timestep, $i-1$ the previous timestep, Δt the timestep and ϕ any physical quantity often considered in conjunction with density ρ, as

$$\frac{\partial}{\partial t}\int_V \rho\phi \; dV = V\left(\frac{\rho_i\phi_i - \rho_{i-1}\phi_{i-1}}{\Delta t}\right) \tag{5.3}$$

While this scheme is robust [51], it does induce numerical diffusion. Therefore, a second order approximation of the time derivative, given as

$$\frac{\partial \phi}{\partial t} = \frac{1}{\Delta t}\left(\frac{3}{2}\phi_i - 2\phi_{i-1} + \frac{1}{2}\phi_{i-2}\right), \tag{5.4}$$

is made available as well.

The second order discretisation is conservative. However it may give nonphysical solutions when the flow experiences severe changes in the time domain. An advantage of the second order model is the extrapolation of an initial guess for the current timestep i based on previous timesteps. As fewer iterations are required to determine the new solution, computational times

are significantly reduced. The current investigation will assess the difference between the two time marching schemes, considering pressure, force and free surface data as well as required computational resources and conservation of mass and momentum.

5.2 Timestep Control

As the velocity of the flow varies throughout the simulation, it is useful to adjust the timestep according to the flow velocity. This is governed using the Courant number, which is the rate of flow speed with which numerical disturbances propagate. The Courant number at node i is defined by Hirsch [49] for finite volume CFD as

$$C_n = u_i \frac{\Delta t}{\Delta x_i}, \tag{5.5}$$

where u_i is the flow velocity, Δt the time step and Δx_i the grid spacing at node i. As mesh size and flow velocity vary throughout the flow field, so will the Courant number. The timestep may be controlled dynamically using either the maximum Courant number or the root mean square of the Courant number (C_N, $_{rms}$) calculated over the entire flow field.

Typically, it is recommended that $C_N \leq 1.0$ to maintain a stable solution if the flow field is not known *a priori* [50]. If the grid spacing Δx were to be halved, the Courant number may be kept constant only by halving the time step as well. This illustrates the interaction between grid size and time discretisation, underlining the importance of considering the time step size when generating the grid. Transient computational studies including grid refinement are thus subject to additional computational penalties. For a two dimensional problem with double the elements in each spatial dimension relative to a reference case, assuming the number of elements is proportional to the computational time, the cost would increase by a factor of four. However, if the problem is transient and the simulated time kept constant, the Courant number would double the computational time further, implying an eight-fold increase from the reference case. This was observed in the run times of the grid independence studies, demonstrating the importance of considering time as an additional dimension in a transient problem.

Systematic time step variations for sloshing flows have been carried out by Hadzic et al [57], Rhee [59] uses a timestep of 0.001 sec. For this time independence study a root mean square

$C_N \leq 0.1$ criterion was applied for timestep adaptation to compare the first and second order schemes. The second order scheme was investigated further using a $C_N \leq 0.05$, $C_N \leq 0.3$ and $C_N \leq 0.5$ timestep criterion for 20 sloshing oscillations.

5.3 Results

5.3.1 Second Order Time Marching - Grid Independence

Grids 1 and 2 as specified in section 4.2, were used to evaluate the performance of the second order time marching scheme. The first order scheme given by equation (5.4) was used in the grid independence study presented in section 4. The second order time marching results obtained are compared with respect to grid spacing to identify any grid dependencies, the subsequent section compares the first and second order Euler time marching schemes.

Considering the pressure histories depicted in figures 5.1 and 5.2 for grids 1 and 2 respectively, one can observe good agreement, especially at P4. In fact, the grid-specific difference in pressure using the second order time marching scheme appears to be considerably less (2.3% at P4, compared to 3.8%) than with the first order scheme in the grid convergence study. The sloshing peaks observed at P9 in figure 5.2 in the transient region are consistent with the water impacting on the North wall.

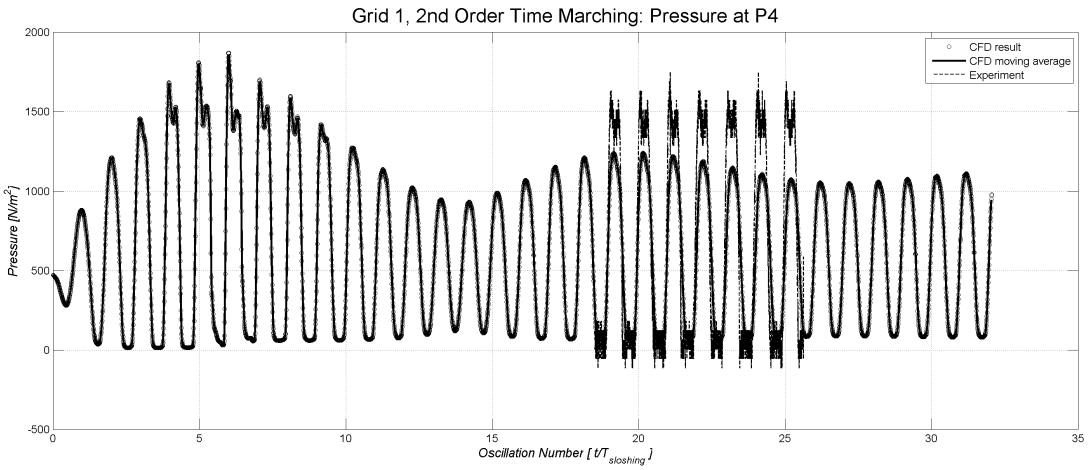

5.1(a): Pressure at P4

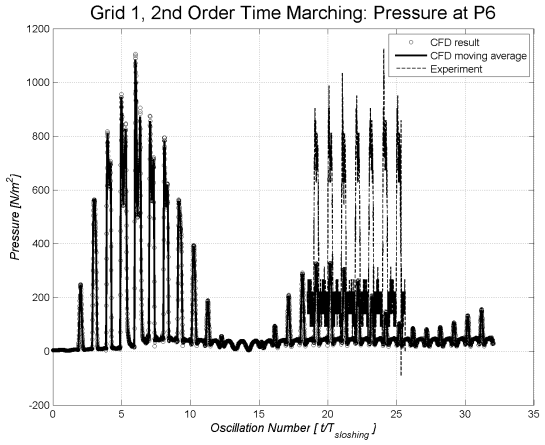

5.1(b): Pressure at P6

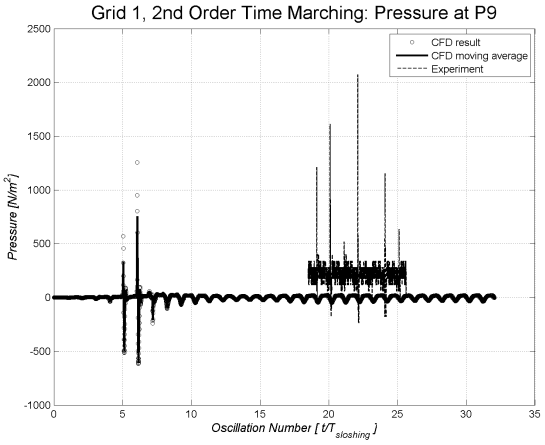

5.1(c): Pressure at P9

Figure 5.1: Pressures at P4, P6 and P9 observed on grid 1 using a second order time marching scheme

The force time histories for grid 1 (figure 5.3) and grid 2 (figure 5.4) agree very well. The East and West wall plots are anti-symmetric as expected, the variation between the force peaks is at a level similar to the grid independence study. Here, the two distinct transient phases are well defined, the first transient phase lasting to oscillation 10, a second reduced pressure phase between oscillations 11 to 20, leading to a near steady state solution from oscillation 20 onwards.

Finally, the free surface shapes, given in figures 5.5(a) for grid 1 and figure 5.5(b) for grid 2, do not depict any significant variations. Considering the above results in conjunction with

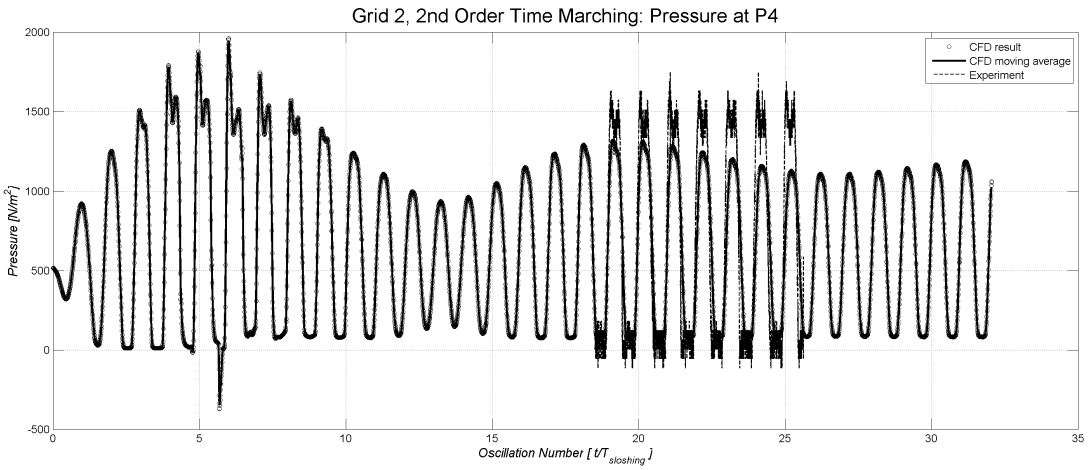

5.2(a): Pressure at P4

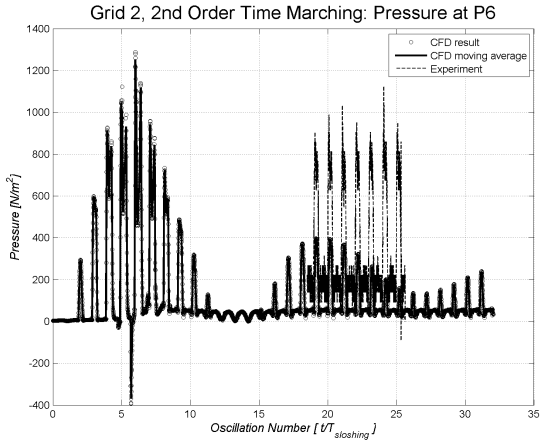

5.2(b): Pressure at P6

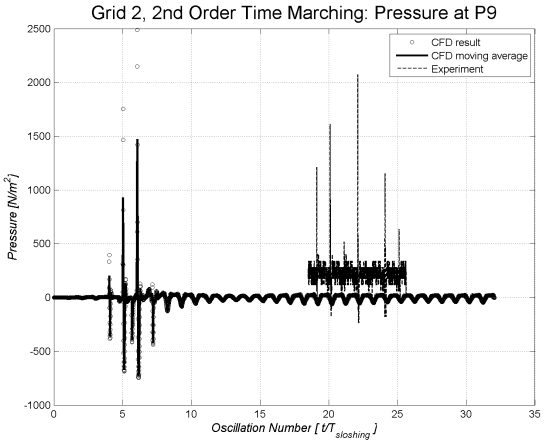

5.2(c): Pressure at P9

Figure 5.2: Pressures at P4, P6 and P9 observed on grid 2 using a second order time marching scheme

the grid independence study it is apparent that grid-dependent variations do not exceed the levels observed using the first order scheme. The difference in free surface position becomes smaller as the simulation progresses toward the steady state as shown in figure 5.6. Therefore, it is permissible to compare the results obtained from the second order scheme to those from the first order scheme.

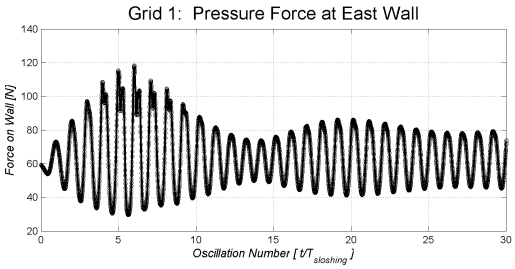

5.3(a): Force on East Wall

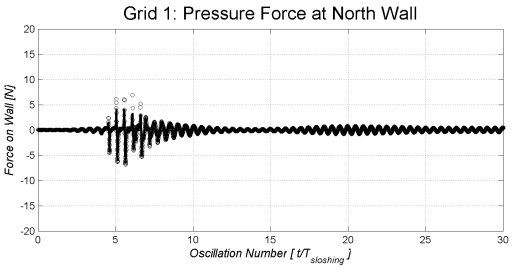

5.3(b): Force on North Wall

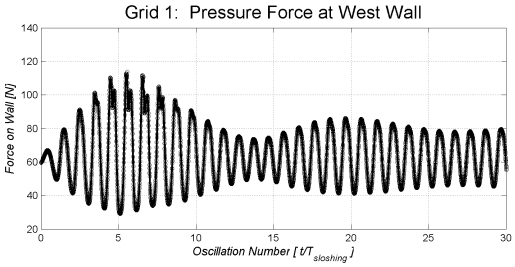

5.3(c): Force on West Wall

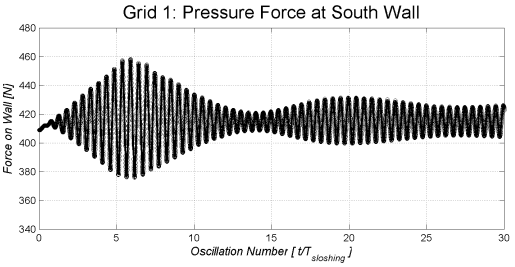

5.3(d): Force on South Wall

Figure 5.3: Force on Tank Walls on Grid 1 using second order time integration

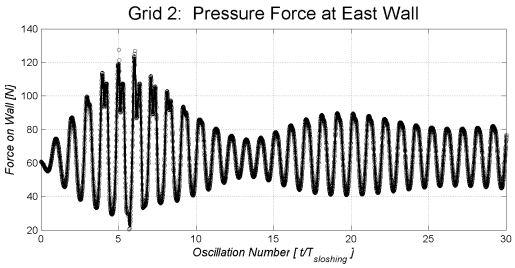

5.4(a): Force on East Wall

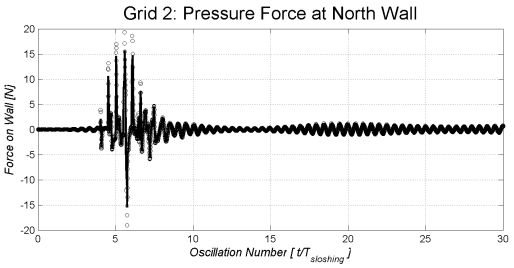

5.4(b): Force on North Wall

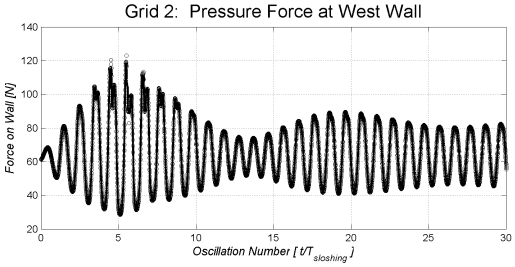

5.4(c): Force on West Wall

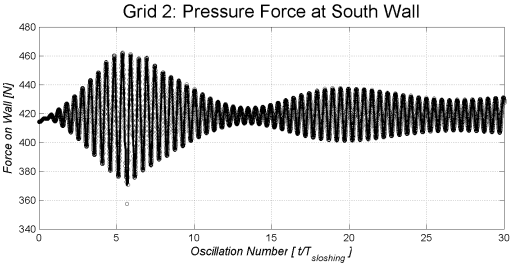

5.4(d): Force on South Wall

Figure 5.4: Force on Tank Walls on Grid 2 using second order time integration

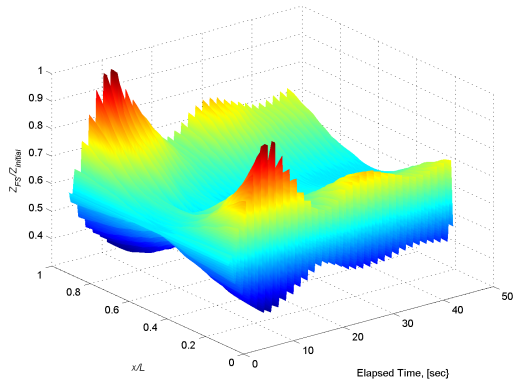

5.5(a): Free surface observed on grid 1

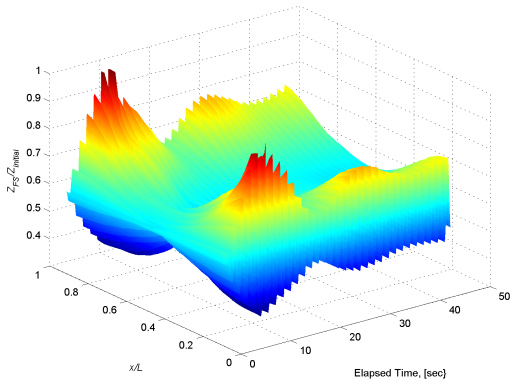

5.5(b): Free surface observed on grid 2

Figure 5.5: Free surface observed with the second order time marching scheme

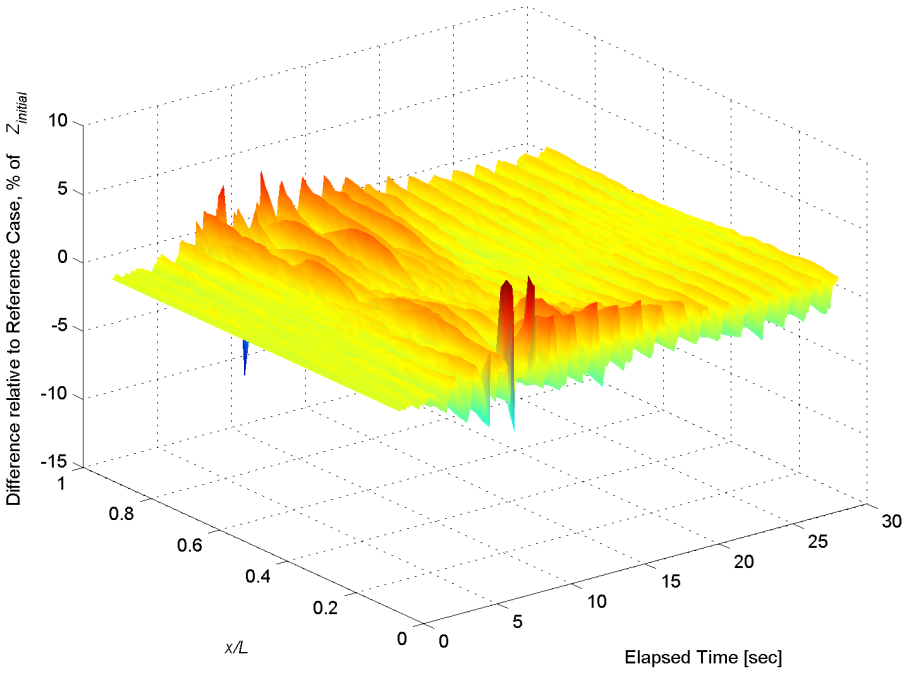

Figure 5.6: Difference of free surface on grid 1 relative to grid 2, both using second order time-marching

5.3.2 First Order v Second Order Time Marching Scheme

The pressure histories show some disagreement, especially in the first transient phase. As the simulation progresses toward the steady state solution, the error becomes less pronounced. The disagreement between first and second order time marching is reduced by approximately

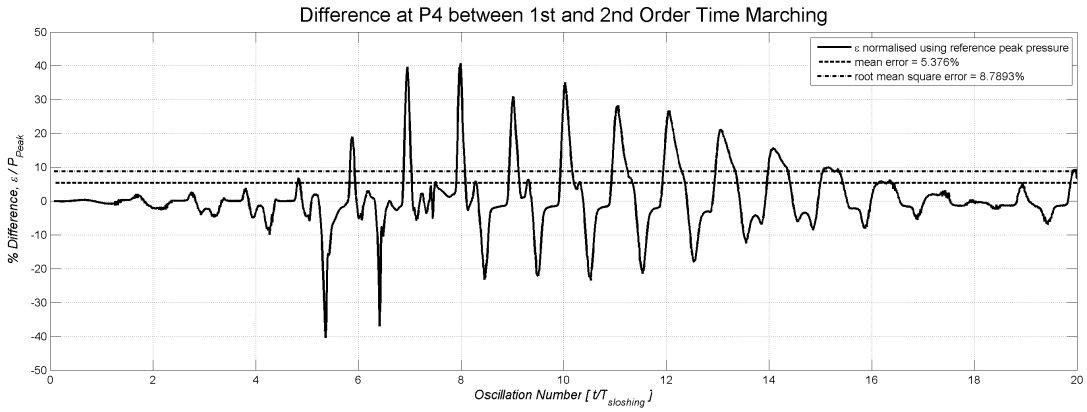

5.7(a): Grid 1

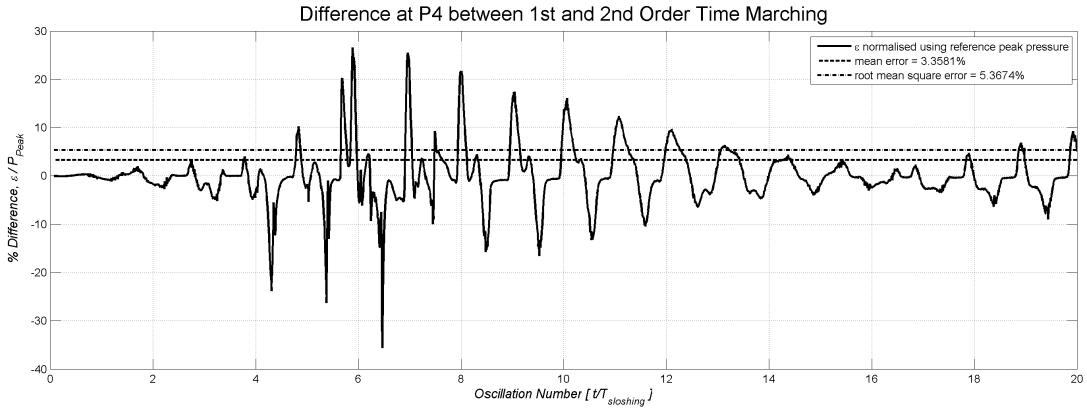

5.7(b): Grid 2

Figure 5.7: Difference between first and second order time marching schemes at P4

40 % when comparing the results obtained on grid 1 and 2. This error decay is observed for the pressure histories at all measured points. The reduction in error as the flow progresses towards a steady state is observed in the wall force comparisons in figure 5.9 as well. There is disagreement in the transient phase, with better agreement in the steady state. The mean error is similar to that found previously.

The second order scheme improved the conservation of mass and momentum considerably. For grid 1, the imbalance rates per second are $-1.52 \cdot 10^{-3}$ for mass, $-2.67 \cdot 10^{-5}$ for x-momentum and $-9.62 \cdot 10^{-5}$ for z-momentum using a second order time marching scheme. The imbalance rates for first order time marching scheme, used in the grid independence study in section 4.4.1, are $-4.38 \cdot 10^{-3}$ for mass, $-1.348 \cdot 10^{-4}$ for x-momentum and $-6.78 \cdot 10^{-5}$ for z-momentum. Note the improvement by nearly an order of magnitude in the x-momentum

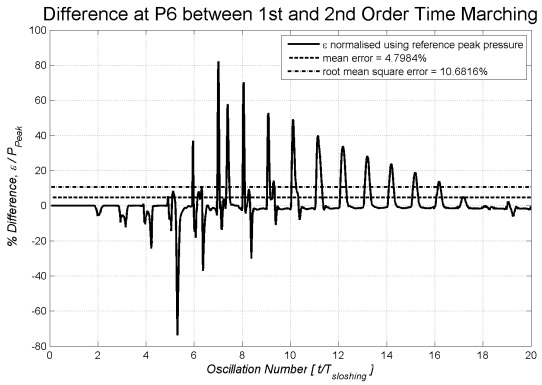

5.8(a): Difference at P6

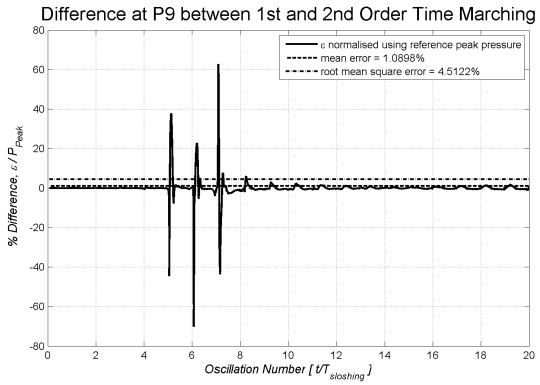

5.8(b): Difference at P9

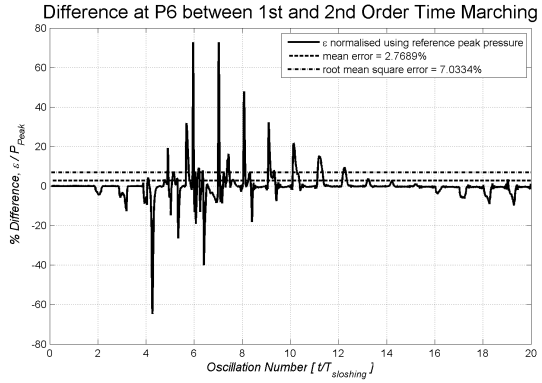

5.8(c): Difference at P6

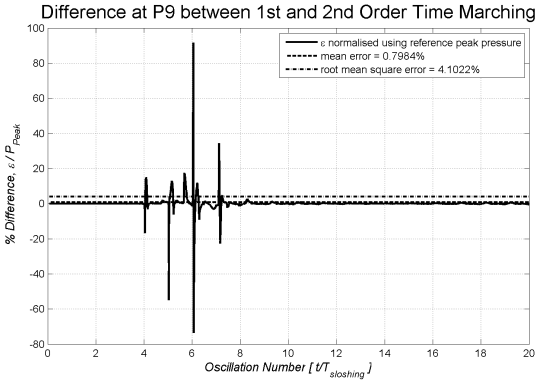

5.8(d): Difference at P9

Figure 5.8: Difference between first and second order time marching schemes at P6 (left column) and P9 (right column)

while mass conservation improves by a factor of three. The conservation of z-momentum is not as good as in the first order time marching scheme, however the overall magnitude of the z-momentum imbalance rate is small. As the convergence criteria for the coefficient loop iteration was set to be $5 \cdot 10^{-5}$, an imbalance rate at a similar order of magnitude is expected.

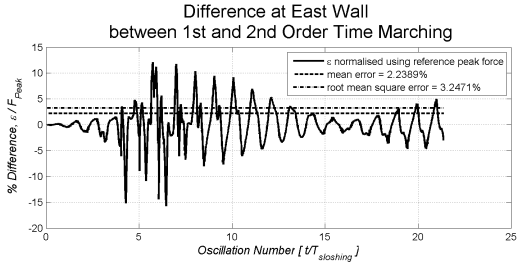

5.9(a): % Difference at East Wall

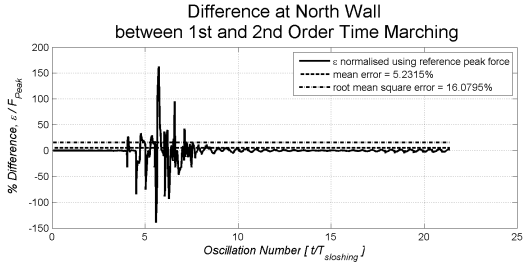

5.9(b): % Difference at North Wall

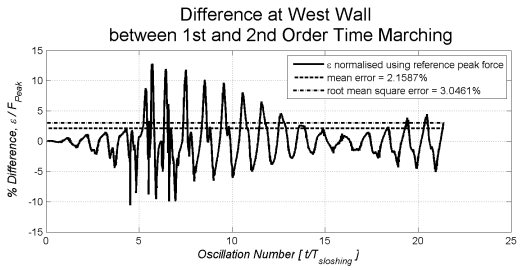

5.9(c): % Difference at West Wall

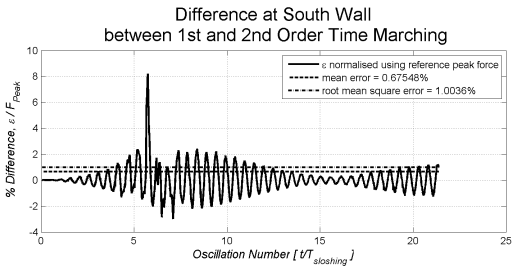

5.9(d): % Difference at South Wall

Figure 5.9: Difference between first and second order time integration using grid 2

5.3.3 Second Order Time Marching - Timestep Control Variation

Following the identification of the second order scheme as the most suitable for the current sloshing problem, a systematic variation of timestep control criteria was carried out. CFX-10 has three available options.

1. The fixed timestep, specifying the timestep explicitly. While this option may sometimes be necessary to force the solution along, it should not be used if the flow behaviour is not known.

2. Maximum Courant number (equation 5.5) control, which identifies the maximum Courant number in the flow field and adjusts the time step so that the maximum Courant number remains below a preset threshold.

3. Finally, the root mean square of the Courant number is calculated for the entire flow field and the time step adjusted as in the previous case.

The timestep in the current study was controlled dynamically using the root mean square Courant number as it is a compromise between methods 1 and 2 described above. Multi-

phase simulations in particular experience convergence problems [51] so the root mean square Courant number ($C_{N,\ rms}$) appears best suited for later use as well.

The cases tested were $C_{N,\ rms} = (0.05, 0.1, 0.3, 0.5)$. The simulation was carried out on grid 2, using a $k - \epsilon$ turbulence model and second-order spatial discretisation as in the grid independence study in section 4. Table 5.1 summarises the computational cost and required iterations to compute the flow over a period of 29 sec, or approximately 20 sloshing oscillations.

Table 5.1: Summary of timestep variation runs

Run	**CPU Time**	**Timesteps**
$C_{N,\ rms} \leq 0.05^*$	$1.49 \cdot 10^5$ [sec]	19231
	41.5 [hrs]	
$C_{N,\ rms} \leq 0.10^{**}$	$1.114 \cdot 10^5$ [sec]	9928
	ukn [hrs]	
$C_{N,\ rms} \leq 0.30^*$	$8.68 \cdot 10^4$ [sec]	3975
	24.1 [hrs]	
$C_{N,\ rms} \leq 0.50^{**}$	$7.55 \cdot 10^4$ [sec]	3117
	21.0 [hrs]	

*2.2 GHz, 64-bit processor with 2 GB RAM

*3.4 GHz, 32-bit processor with 2 GB RAM

When considering the computational cost alone it appears that the highest Courant number is the most effective. However, the quality of the computational results depends on the time step size as well. Analogous to the grid independence study, time discretisation independence needs to be confirmed as well. Hadzic *et al* [57] identify a dependence of wave breaking on the timestep size, albeit the error induced by the timestep is small compared to the spatial discretisation. While the pressure and force histories are omitted for the Courant number variations, the differences relative to the reference case of $C_{N,\ rms} \leq 0.05$ are shown below.

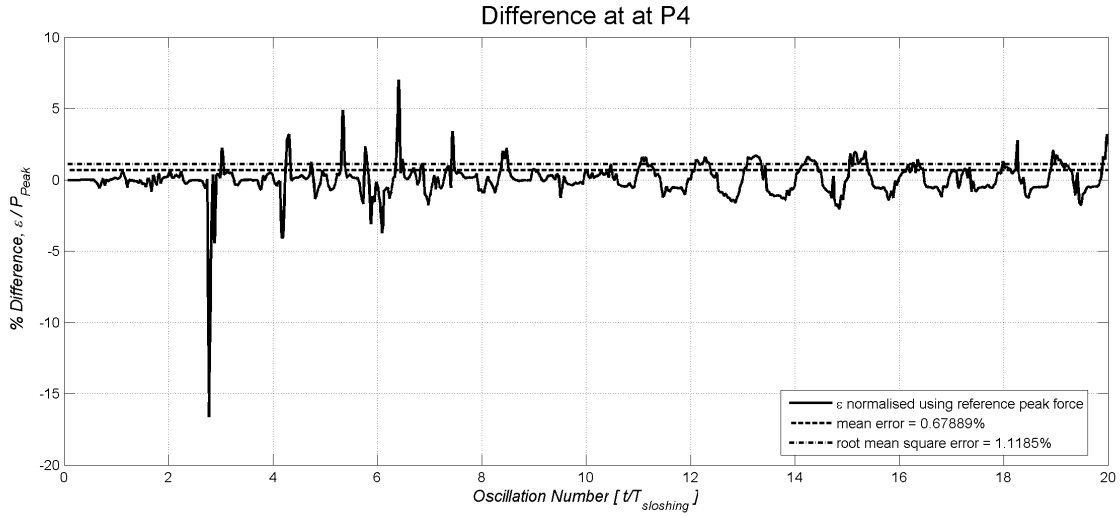

5.10(a): Root Mean Square C_N, $_{rms} \leq 0.10$

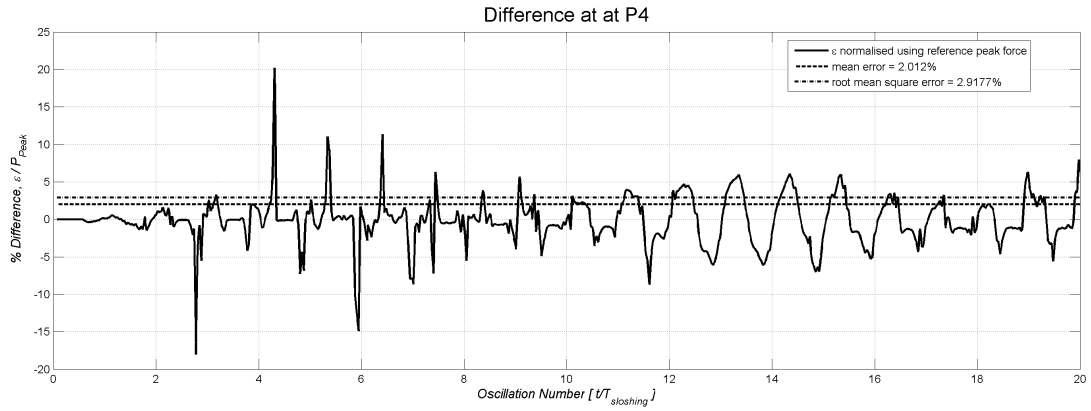

5.10(b): Root Mean Square C_N, $_{rms} \leq 0.30$

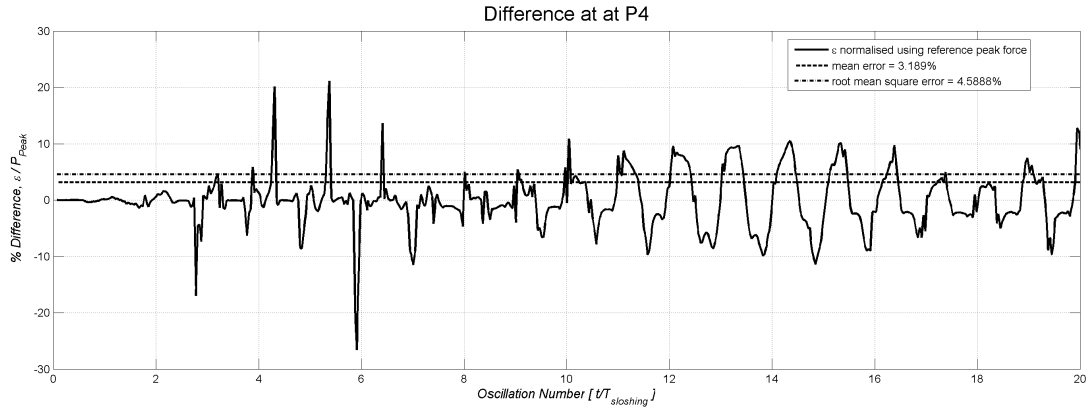

5.10(c): Root Mean Square C_N, $_{rms} \leq 0.50$

Figure 5.10: Pressure differences at P4 with C_N, $_{rms} \leq 0.05$ as reference

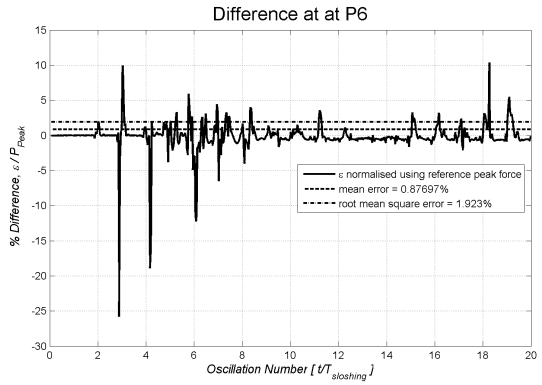

5.11(a): Root Mean Square C_N, $_{rms} \leq 0.10$

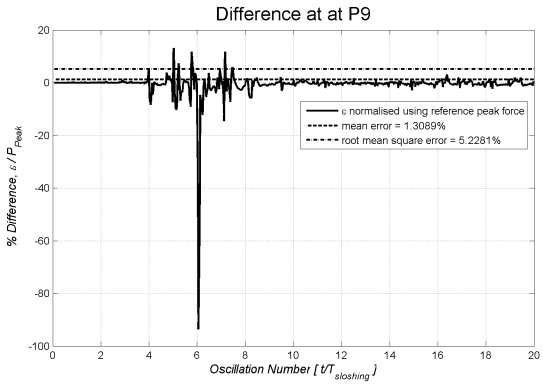

5.11(b): Root Mean Square C_N, $_{rms} \leq 0.10$

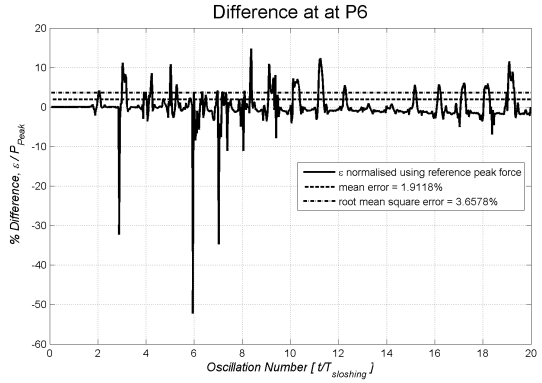

5.11(c): Root Mean Square C_N, $_{rms} \leq 0.30$

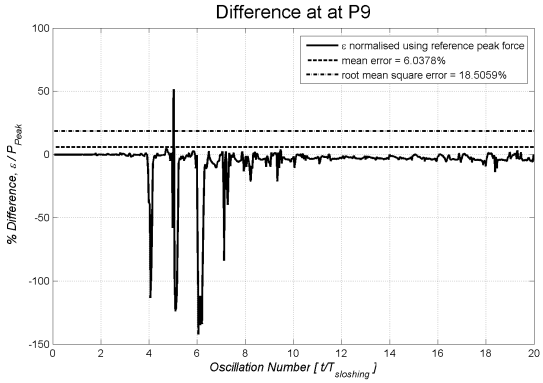

5.11(d): Root Mean Square C_N, $_{rms} \leq 0.30$

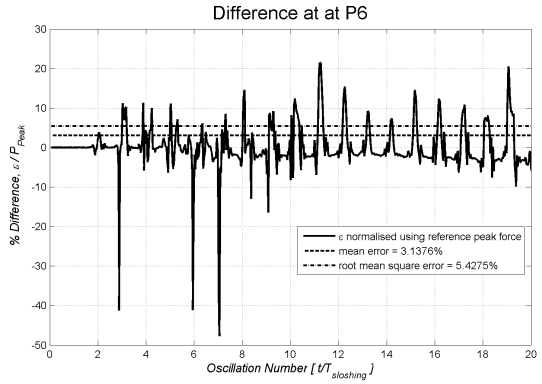

5.11(e): Root Mean Square C_N, $_{rms} \leq 0.50$

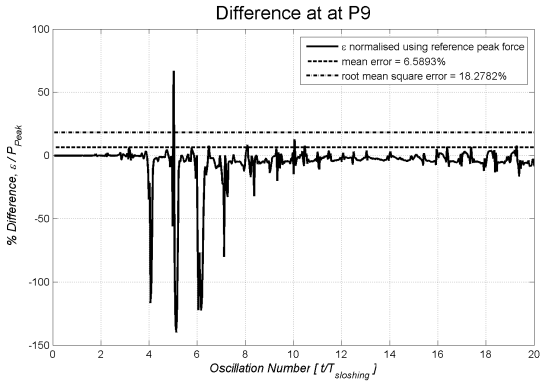

5.11(f): Root Mean Square C_N, $_{rms} \leq 0.50$

Figure 5.11: Pressure differences at P6 (left column) and P9 (right column) with C_N, $_{rms} \leq 0.05$ as reference

Pressure

The pressure histories show convergence with decreasing timestep size, with a constant periodic error observed once the flow has progressed onto the second transient stage. The most significant errors are in the initial transient region encompassing the first ten oscillations. This is confirmed by Hadzic *et al* [57]. While the error at P4 in figure 5.10 appears centered about a zero mean, the errors at P6 and P9, shown in figure 5.11, show that the larger timesteps tend to overestimate the pressure at times by as much as 20 %. Considering the rectified mean and root mean square errors, convergence of the solutions can be observed.

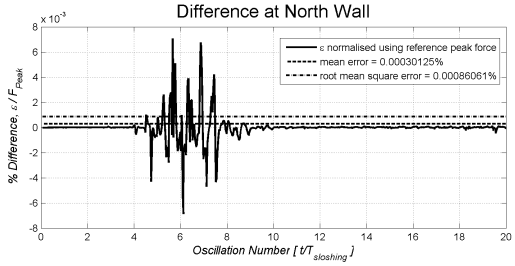

5.12(a): Root Mean Square $C_N,\ _{rms} \leq 0.10$

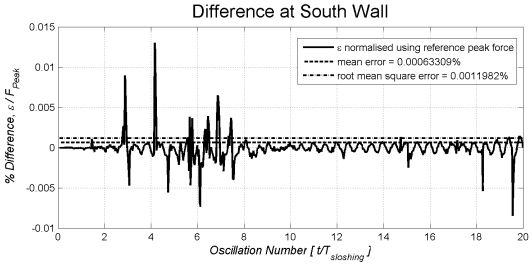

5.12(b): Root Mean Square $C_N,\ _{rms} \leq 0.10$

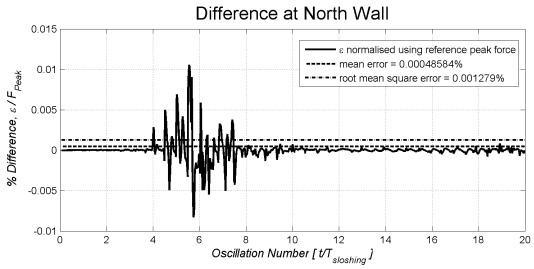

5.12(c): Root Mean Square $C_N,\ _{rms} \leq 0.30$

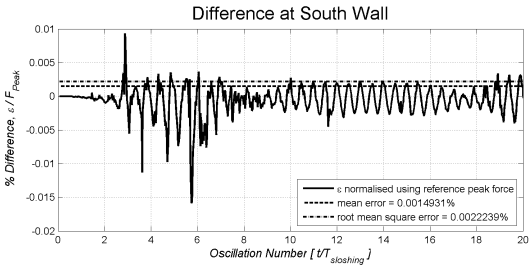

5.12(d): Root Mean Square $C_N,\ _{rms} \leq 0.30$

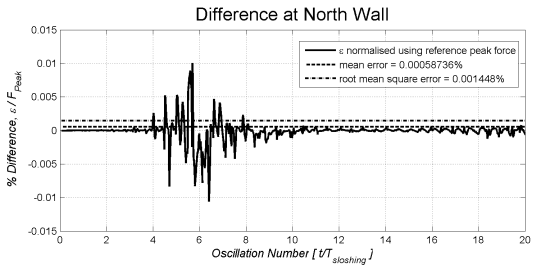

5.12(e): Root Mean Square $C_N,\ _{rms} \leq 0.50$

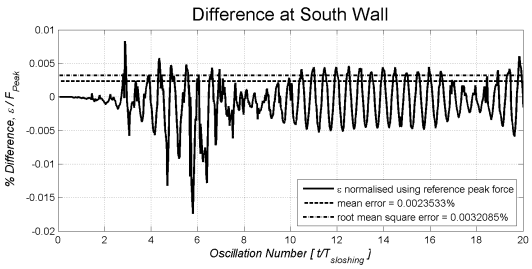

5.12(f): Root Mean Square $C_N,\ _{rms} \leq 0.50$

Figure 5.12: Wall pressure force differences at North (left column) and South (right column) wall with $C_N,\ _{rms} \leq 0.05$ as reference

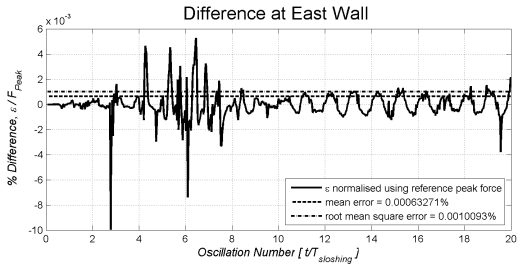

5.13(a): Root Mean Square $C_N,\ _{rms} \leq 0.10$

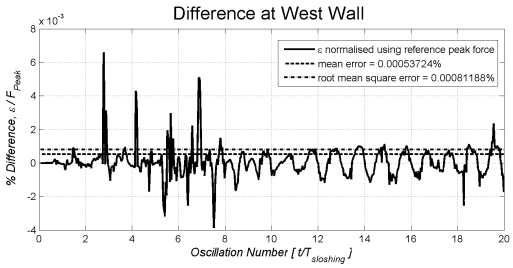

5.13(b): Root Mean Square $C_N,\ _{rms} \leq 0.10$

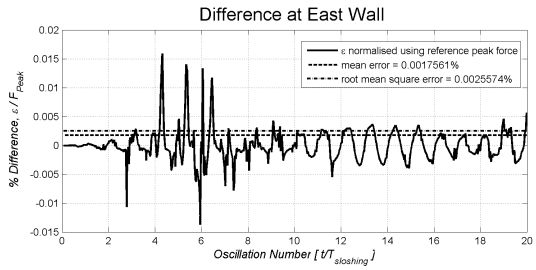

5.13(c): Root Mean Square $C_N,\ _{rms} \leq 0.30$

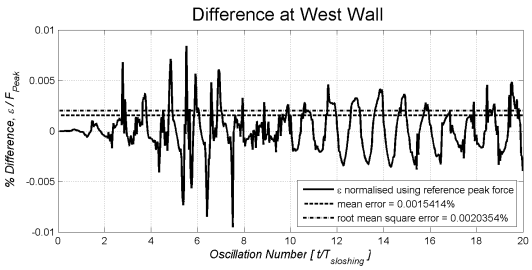

5.13(d): Root Mean Square $C_N,\ _{rms} \leq 0.30$

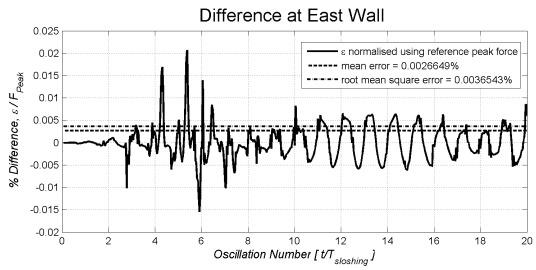

5.13(e): Root Mean Square $C_N,\ _{rms} \leq 0.50$

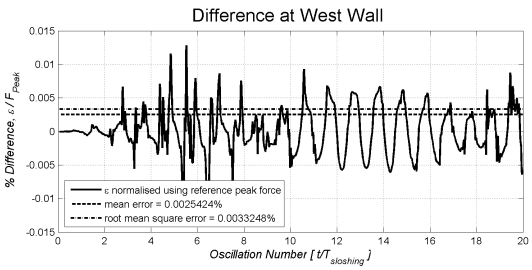

5.13(f): Root Mean Square $C_N,\ _{rms} \leq 0.50$

Figure 5.13: Wall pressure force differences at East (left column) and West (right column) wall with $C_N,\ _{rms} \leq 0.05$ as reference

Force

The force difference plots show similar trend to that observed in the pressure plots. The relative differences in the steady state are considerably smaller. This indicates that the significant pressure differences are observed when the pressure sensor is near the free surface, as is the case with P6 and P9. The most significant differences are again observed in the initial transient phase, with a more constant error once the simulation progresses past oscillation 15. The convergence properties are analogous to those determined from the pressure differences.

Figure 5.14 shows the lateral displacement of the fluid centre of gravity. This is a global indicator of the convergence properties of the flow. All timesteps maintain the periodicity of

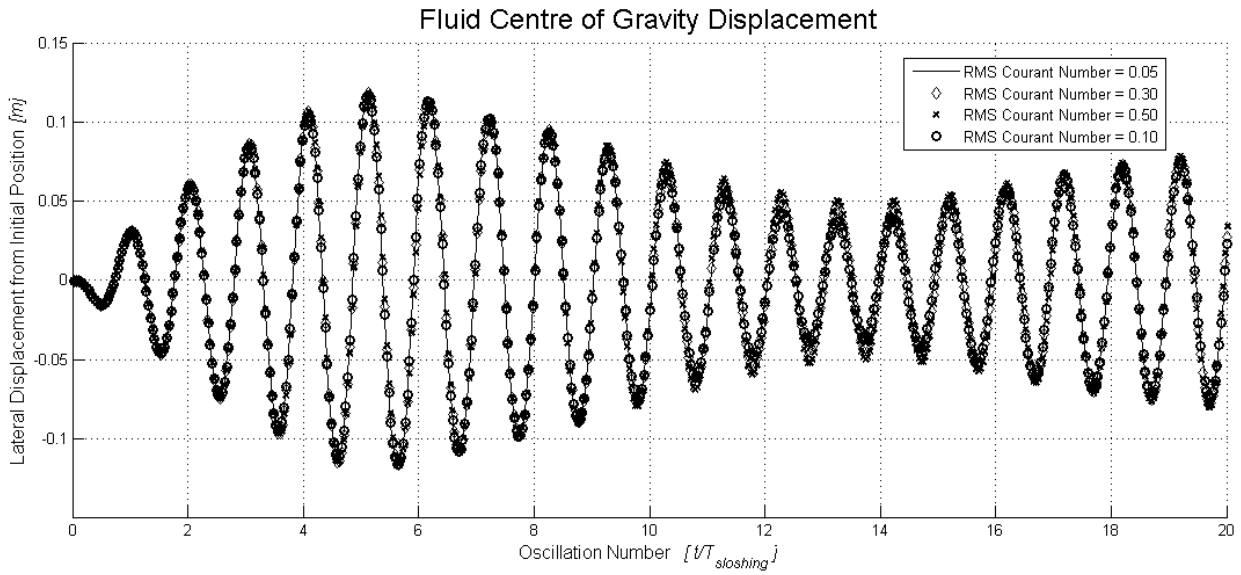

Figure 5.14: Lateral fluid centre of gravity displacement due to sloshing

the flow well. The peak displacement in the initial transient phase during oscillations four to six is coincident for all Courant numbers. However, the solutions using the higher Courant numbers, $C_N = [0.3, 0.5]$, overpredicts the centre of gravity displacement slightly in the second transient phase, especially between oscillations 12 and 16. However, as the flow approaches the steady state, all three centre of gravity plots have converged.

5.4 Recommendations

While there is initial disagreement in the transient phase, the steady state phase shows good agreement. This may be attributable to the more violent flow regime in the initial transient phase. Despite the violent nature of the flow, the second order scheme is sufficiently robust to deal with this. Given the additional computational cost incurred by selecting second over first order discretisation one may question the rationale for doing so. The second order scheme is superior to first order scheme for the following reasons.

- Computational Speed. It is possible to extrapolate an initial guess for each time step, which generally results in considerably quicker convergence of the iteration. The problem analysed on grid 1 took 2 days to run using a first order scheme, while the second order time discretisation finished after only 20 hours. However when simulating flows fields with rapid time-dependent changes, the computational stability is reduced. In some cases, the extrapolating the solutions leads the flow into a 'blind alley' from which it is not possible to recover the solution.

- Conservation Properties. The second order scheme improves conservation of mass and momentum by an order of magnitude compared to the first order scheme. This is especially valuable when simulating extended time scales.

The subsequent variation of the time step size using the root mean square of the Courant number has revealed that the flow is mostly independent of time step. Hadzic *et al* [57] describe the sloshing problem as non-deterministic in the time domain, as there exists a strong correlation between time step size and the onset of wave breaking. However, the fluid centre of gravity plot shows that there is very little difference in the total fluid motion over the range of time steps tested. However, the reduction in required time steps with the highest Courant number $C_{N,\ rms} \leq 0.5$ control was not matched with the corresponding decline in computational cost. In addition, more violent flows investigated tend to be more stable with a smaller time step.

Therefore, the second order scheme is recommended as a default for simulating sloshing flows. The timestep initialisation option available in conjunction with this scheme should only be used when there is certainty that there are no abrupt time-dependent changes, such as wave

Table 5.2: Summary of results analysis for time discretisation study

Model	**Reference**	**Pressure**			**Wall Pressure Force**			
		P4 [%]	P6 [%]	P9 [%]	North [%]	East [%]	South [%]	West [%]
1^{st} order,	2^{nd} order,	5.38	4.80	1.09				
Gird 1	Grid 1	8.79	10.7	4.51				
1^{st} order,	2^{nd} order,	3.36	2.77	0.80	5.23	2.24	0.68	2.16
Grid 2	Grid 2	5.37	7.03	4.10	16.1	3.25	1.00	3.05
$C_N^{rms} \leq 0.1$	$C_N^{rms} \leq 0.05$	0.68	0.88	1.31	$3.01 \cdot 10^{-4}$	$6.33 \cdot 10^{-4}$	$6.33 \cdot 10^{-4}$	$5.37 \cdot 10^{-4}$
	(RMS)	1.12	1.92	5.22	$8.61 \cdot 10^{-4}$	$1.01 \cdot 10^{-3}$	$1.12 \cdot 10^{-3}$	$8.12 \cdot 10^{-4}$
$C_N^{rms} \leq 0.3$	$C_N^{rms} \leq 0.05$	2.01	1.9	6.04	$4.86 \cdot 10^{-4}$	$1.76 \cdot 10^{-3}$	$1.49 \cdot 10^{-3}$	$1.54 \cdot 10^{-3}$
	(RMS)	2.92	3.66	18.5	$1.28 \cdot 10^{-3}$	$2.56 \cdot 10^{-3}$	$2.22 \cdot 10^{-3}$	$2.04 \cdot 10^{-3}$
$C_N^{rms} \leq 0.5$	$C_N^{rms} \leq 0.05$	3.19	3.14	6.60	$5.87 \cdot 10^{-4}$	$2.66 \cdot 10^{-3}$	$2.35 \cdot 10^{-3}$	$2.54 \cdot 10^{-3}$
	(RMS)	4.59	5.43	18.3	$1.45 \cdot 10^{-3}$	$3.65 \cdot 10^{-3}$	$3.21 \cdot 10^{-3}$	$3.32 \cdot 10^{-3}$

breaking, in the flow regime. One example where extrapolation could be used advantageously is given by low amplitude, low frequency sloshing. Sometimes it may be necessary to resort to the first order scheme, but this should only be used when the second order scheme is unstable. However, a better solution to this problem is usually found by improving the grid.

The timestep should be controlled dynamically, as this best reflects the changing nature of the sloshing flow. A criterion of $C_{N,\ rms} \leq 0.3$ should be used as the upper limit. However, there is little rationale for using a timestep smaller than that mandated by a limit of $C_{N,\ rms} \leq 0.1$. For sloshing simulations of a similar nature to the present problem a timestep governed by $C_{N,\ rms} \leq 0.2$ has been found to work satisfactorily for the grid series given in section 4 as well as a boundary-fitted used for the multiphase simulation of an advanced turbulence model in section 6.3.1.

6 Turbulence Fluid Model Comparison

6.1 Background

Considering the discussion pertaining to turbulence modelling in section 3.3, one may appreciate both the reduced computational requirements (no transport equations for turbulence quantities) to solve a laminar flow problem as well as the additional uncertainties introduced when resorting to a turbulence model. However, a laminar flow has a much thinner wall boundary layer and will need many more cells to capture the velocity gradient to the same order of accuracy. The Reynolds number

$$Rn = \frac{VL}{\nu}, \tag{6.1}$$

where a characteristic velocity $V = 4$ m s^{-1}, a characteristic length $L = 1.2$ m and the kinematic viscosity $\nu = 1.18 \cdot 10^{-6}$ m^{2}s^{-1}, is used as the primary indicator of a turbulent flow. Due to the unsteady nature of the sloshing flow, as well as no readily identifiable typical velocity the characteristic values used in equation (2.5) above are obtained from a previously completed run. For the above parameters the Reynolds number $Rn = 4.1 \cdot 10^6$ indicates that the flow is turbulent. However, as a sloshing flow is inherently periodic while equation (2.5) is more appropriate for steady flows, Ibrahim [18], among others, resorts to other non-dimensional parameters. There is no consensus whether a sloshing flow should be modelled as turbulent or laminar. Some authors, including El Moctar [23], Fallon et al [57], Rhee [59] and Standing et al [58] assume the flow to be turbulent, while Price and Chen [56] use a laminar flow model.

Given this uncertainty as well as the potential computational savings, it is useful to investigate the impact of turbulence modelling on the quality of the computational results, computational times and convergence properties. While CFX-10 offers a number of turbulence models, only the $k - \epsilon$ model outlined in section 3.3.2 and the Reynolds stress model outlined in section 3.3.3 are used in this study. The $k - \epsilon$ model has been used in a number of sloshing simulations, while the Reynolds stress model represents a more sophisticated, albeit computationally expensive approach. Results are given for each case and then compared to identify the most suitable model.

6.2 Laminar Flow

6.2.1 Results

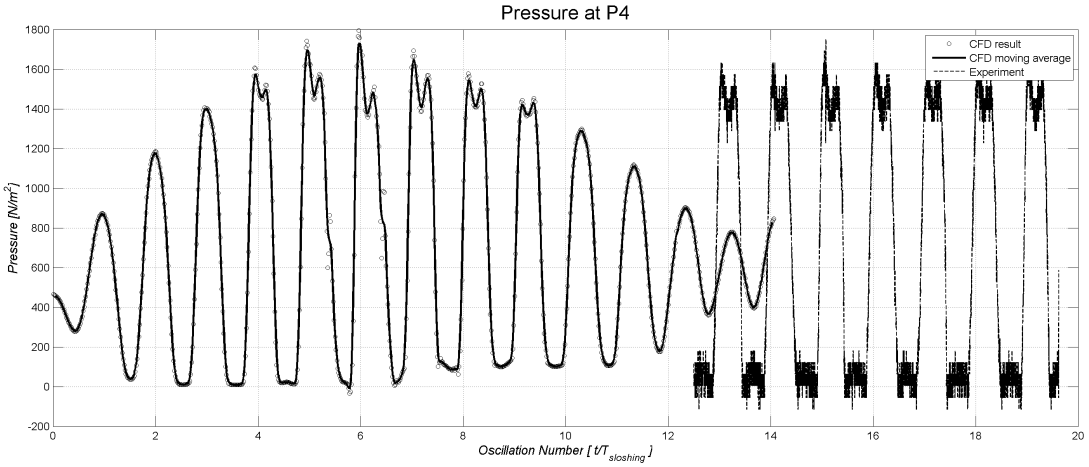

6.1(a): Pressure at P4

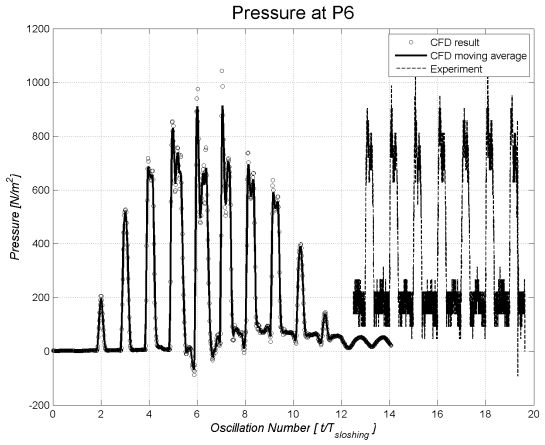

6.1(b): Pressure at P6

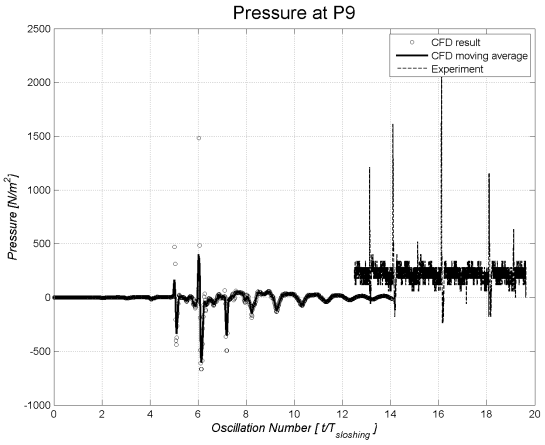

6.1(c): Pressure at P9

Figure 6.1: Pressures at P4, P6 and P9 using a laminar fluid model on grid 1

Pressure

The pressure pattern in the transient region, shown in figure 6.1, corresponds to the sloshing flow striking the top wall, as in most other CFX runs. However, the pressure changes are more abrupt. The significant differences appear once the pressure history enters the second transient phase after oscillation 10. Here, the pressures are slightly more than 50% of the initial pressure peaks in figure 6.1(a), the other pressure sensors P6 and P9 show an even

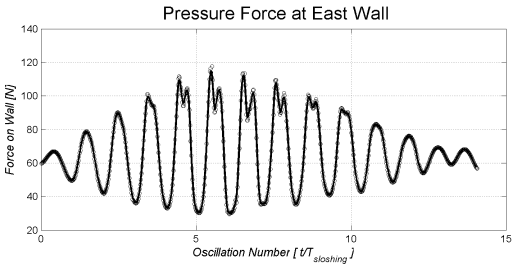

6.2(a): Force at East Wall

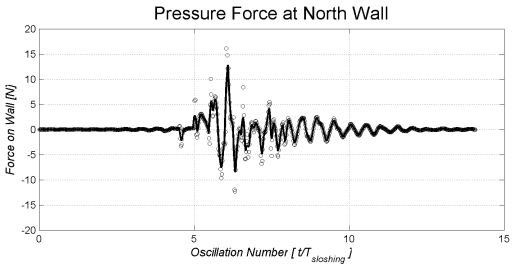

6.2(b): Force at North Wall

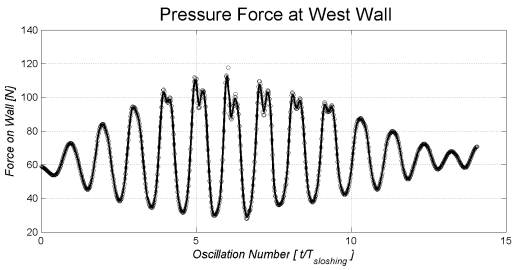

6.2(c): Force at West Wall

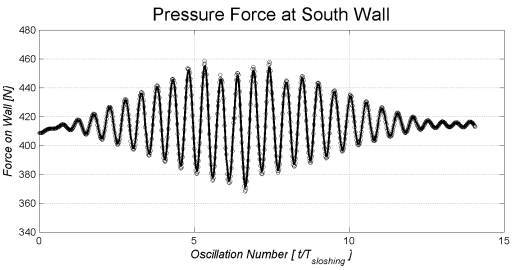

6.2(d): Force at South Wall

Figure 6.2: Force on tank walls using a laminar fluid model on grid 1

greater difference.

Force

The force in figures 6.2(a) to 6.2(d) show similar behaviour. The force plot for the South wall in figure 6.2(d) is particularly troublesome, as the force oscillates within a small fraction of the static component - this does not correlate well with the transient phase!

6.2.2 Grid Convergence

Figure 6.3 examines the effect of doubling the number of grid points on the pressure history. There is a considerable difference in the transient case as the pressure is much smaller when approaching the steady state. This trend continues for the pressure plots in figures 6.3(b) and 6.3(c). The force acting on East and West walls differs by nearly 15% in the latter stages of figures 6.4(a) and 6.4(c) between grids 1 and 2.

The difference between the pressure and force histories between the two grids is nearly double the difference for the $k - \epsilon$ turbulence model. This implies that the convergence properties of the laminar model require a finer grid to reduce the grid dependence of the results

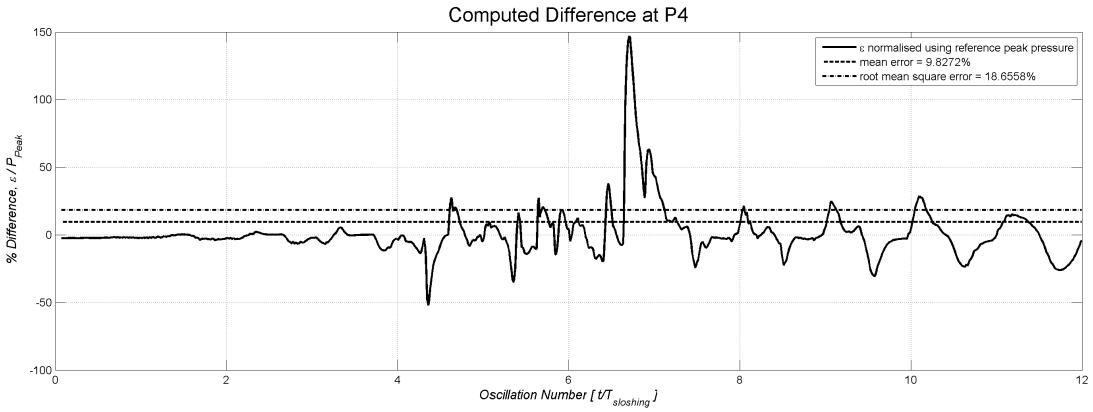

6.3(a): Pressure Difference at P4

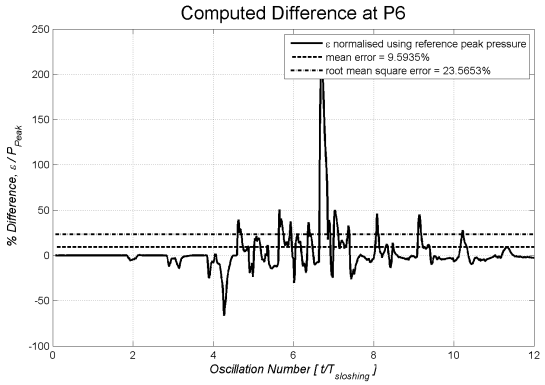

6.3(b): Pressure Difference at P6

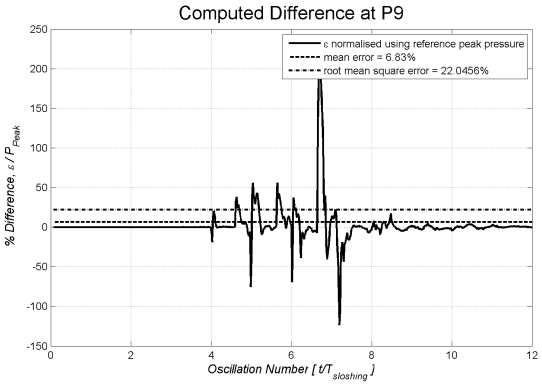

6.3(c): Pressure Difference at P9

Figure 6.3: Pressure Differences between grids 1 and 2 at P4, P6 and P9 using a laminar fluid model

and reach a grid-independent solution. However, the computational times are considerably shorter as no transport equations have to be solved for the turbulence model.

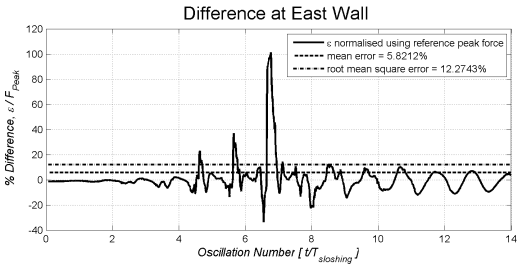

6.4(a): % Difference at East Wall

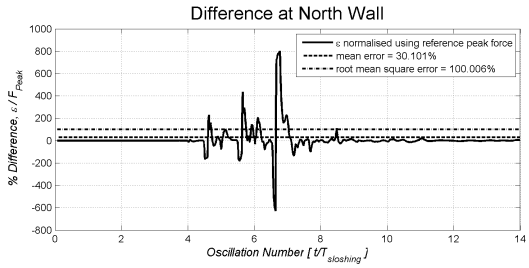

6.4(b): % Difference at North Wall

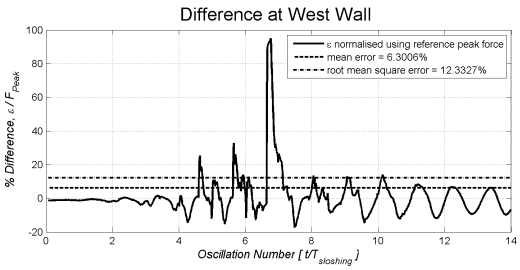

6.4(c): % Difference at West Wall

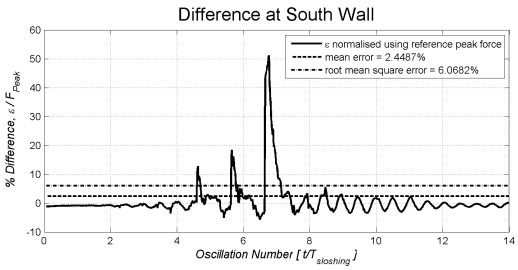

6.4(d): % Difference at South Wall

Figure 6.4: Force Differences between grids 1 and 2 using a laminar fluid model

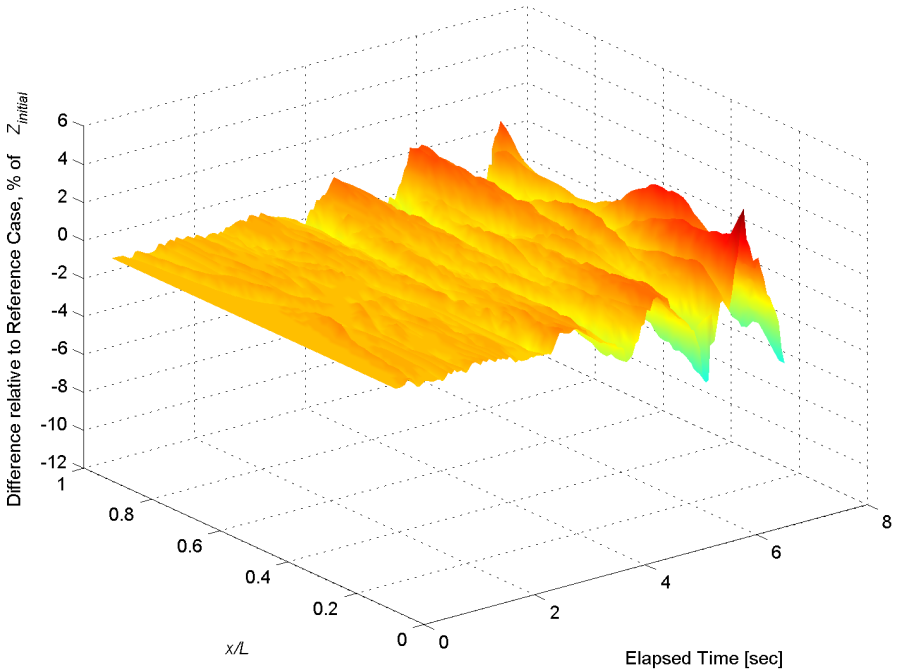

Figure 6.5: Difference of free surface on grid 1 relative to grid 2

6.3 Turbulent Flow Results

The faithful representation of a turbulent boundary layer in CFD depends not only on the choice of turbulence model but also on the location of the first near-wall grid point. This is usually expressed as

$$y^+ = \frac{\rho \Delta y u_\tau}{\mu}, \tag{6.2}$$

where ρ and μ are fluid density and dynamic viscosity respectively, Δy the distance from the wall and u_τ the friction velocity defined by

$$u_\tau = \left(\frac{\tau_w}{\rho} \right)^{1/2} \tag{6.3}$$

with τ_w the wall shear stress. Usually the ideal location of the first near-wall grid point is defined by a value of $20 \leq y^+ \leq 100$ for high Reynolds number flows while low Reynolds number flows are best resolved to $y^+ \leq 1$ [65]. This is useful for steady state simulations but the cyclical nature of a sloshing flow makes the satisfaction of the above criteria impossible without resorting to grid deformation.

The main reason for mandating a fine grid for low Reynolds number flows are modelling errors introduced by the wall functions[4]. Fortunately CFX offers 'scalable wall functions' which allow more flexibility in the boundary layer grid by selecting the appropriate boundary layer region automatically. This improves the stability of the turbulence models as well.

While it is recognised that y^+ is an important computational parameter it is not used to compare the simulations with turbulence models.

1. The most automated wall function selection procedure available in CFX-10 was chosen to adapt the wall function according to the changing nature of the flow.

2. y^+ varies spatially and is time dependent as well, requiring a plotting strategy similar to pressure and free surface location. Hence only a snapshot within space or time can be produced to give a meaningful representation of the evolution of y^+.

[4] A turbulent boundary layer is usually split into a linear and logarithmic region with different and often contradictory modelling requirements. The background is explained by Pope [54] and will not be reproduced in this report.

3. The two turbulence models used, the $k-\epsilon$ and Speziale, Sarkar and Gatsi (SSG) models are based on completely different first principles. Hence the causes of differences in the attained values of y^+ cannot be attributed so as to draw meaningful conclusions.

6.3.1 SSG Grid Independence

This section gives the pressure histories for the $k-\epsilon$ and SSG Reynolds stress models. As the Reynolds stress model required a different grid, both the $k-\epsilon$ and Reynolds stress models are given on this grid. It contains 9605 elements, with an node distribution orthogonal to the wall in the 35 mm surrounding the wall. The first node is 0.3 mm from the wall and the orthogonal layer consists of 20 nodes perpendicular to the wall. A regular structure is applied in all other regions. Comparisons between the $k-\epsilon$ and the laminar flow results are made using the original grid 2 described in section 4.2. Despite the use of an orthogonal grid for the comparison of the $k-\epsilon$ and SSG turbulence models, it is nonetheless instructive to compare the results obtained with both grids.

Figure 6.6 shows the differences between the orthogonal grid and grids 2 and 3 used in the grid independence study. As before, the differences are most significant during the initial transient phase. As the solution tends to the steady state, the difference is reduced. Comparing the errors for the o-grid and grid 2 (left column of figure 6.6) and grid 3 (right column in figure 6.6), the error periods are shorter and the mean error decreases. The magnitude of the mean error, defined by equation (4.10) is similar to the differences observed in the grid independence study. The difference at P4, the difference of 2.5% is higher than the 1.4% difference between girds 2 and 3. A similar trend is observed for P6 and P9. Therefore, one may conclude that the results obtained with the o-grid and standard grid used in the grid independence study in section 4 are sufficiently similar, alleviating the need for a further grid independence study.

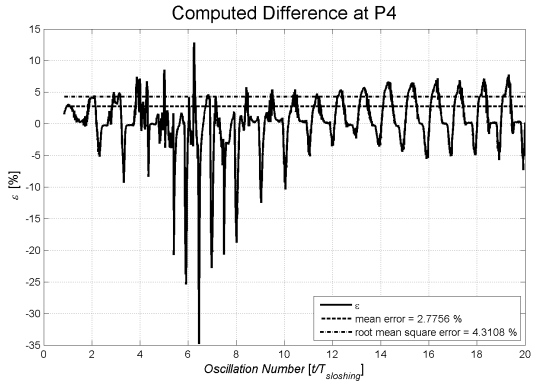

6.6(a): Difference at P4

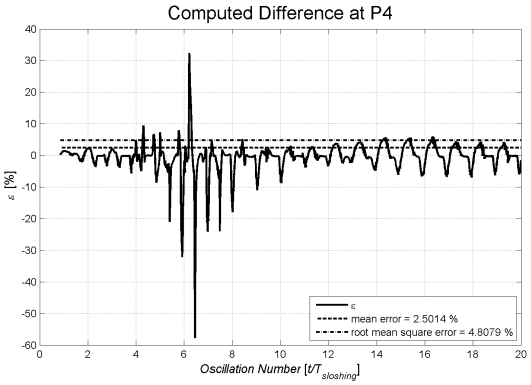

6.6(b): Difference at P4

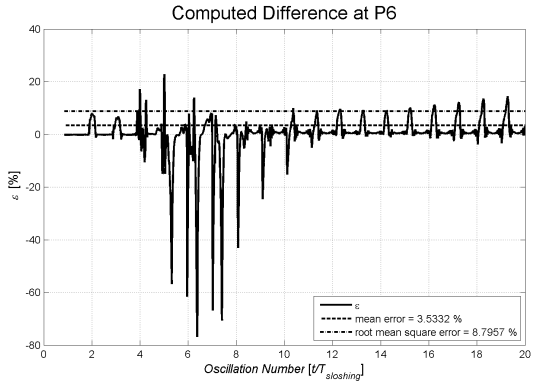

6.6(c): Difference at P6

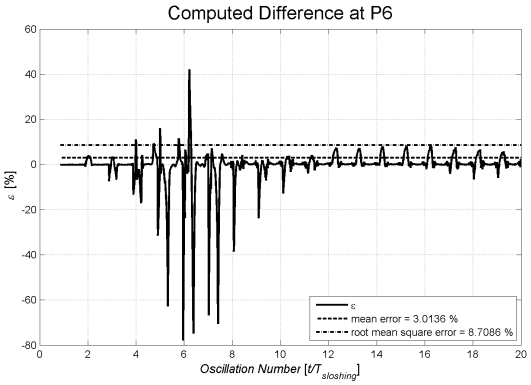

6.6(d): Difference at P6

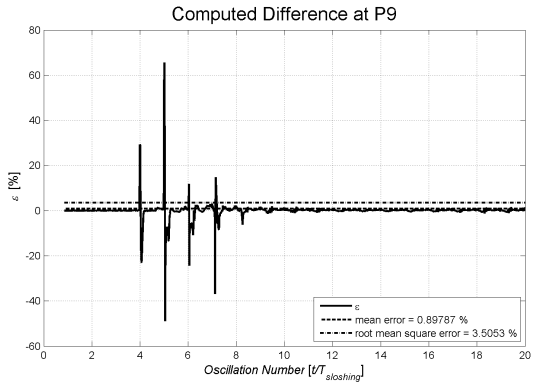

6.6(e): Difference at P9

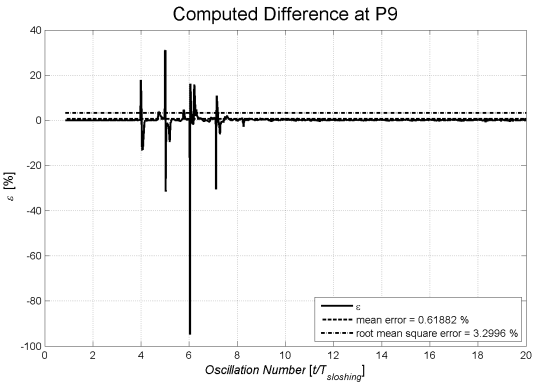

6.6(f): Difference at P9

Figure 6.6: Pressure differences between o-grid v grid 2 (left column) and grid 3 (right column)

6.3.2 $k - \epsilon$ Results

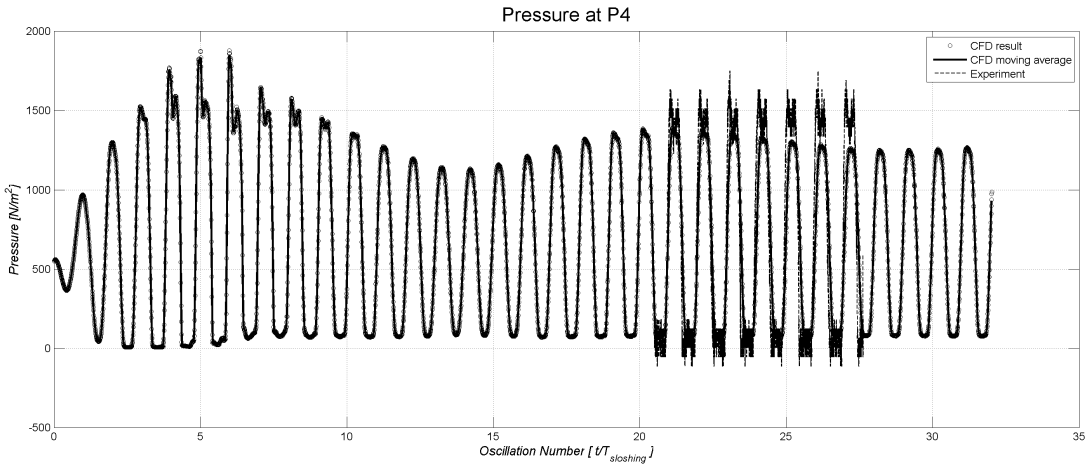

6.7(a): Pressure at P4

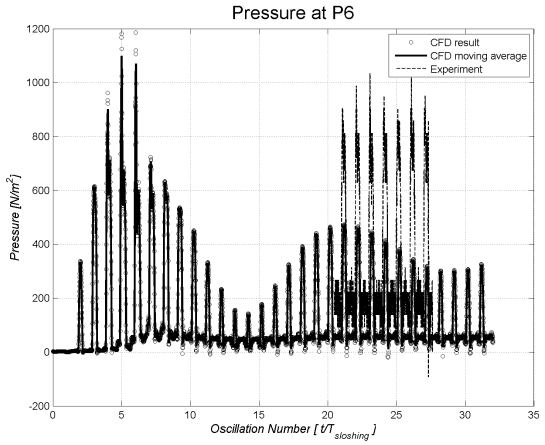

6.7(b): Pressure at P6

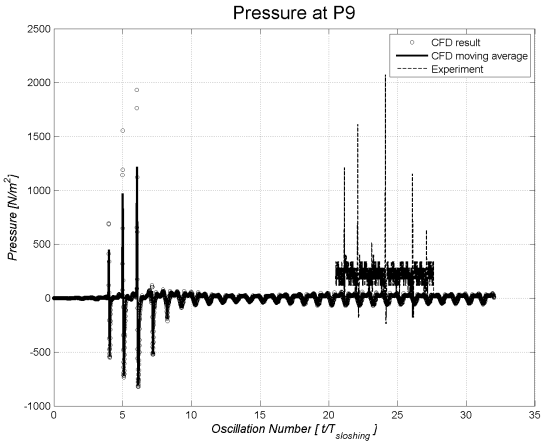

6.7(c): Pressure at P9

Figure 6.7: Pressure history using a $k - \epsilon$ model on an orthogonal grid

The pressure results depicted in figure 6.7 are similar to the pressure results obtained in the grid independence study with the comparable grid 2 in figure 4.5. The two transient sloshing phases are well defined, with a steady state sloshing phase after 20 oscillations. Unfortunately the computational results still do not relate well to those obtained from experiment as shown in figure 6.7(b) and 6.7(c) for P6 and P9 respectively. One may conclude the change in grid structure did not influence the results and either grid could be used as a basis for comparison.

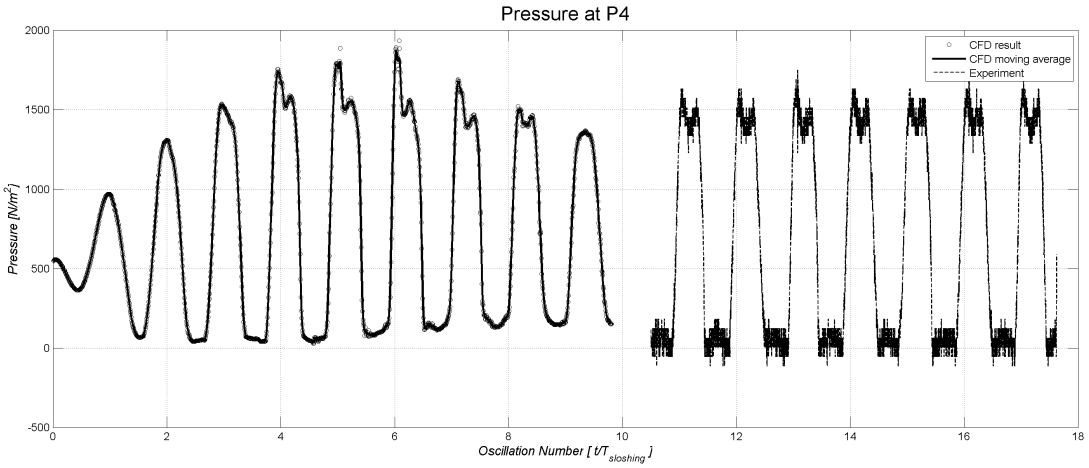

6.8(a): Pressure at P4

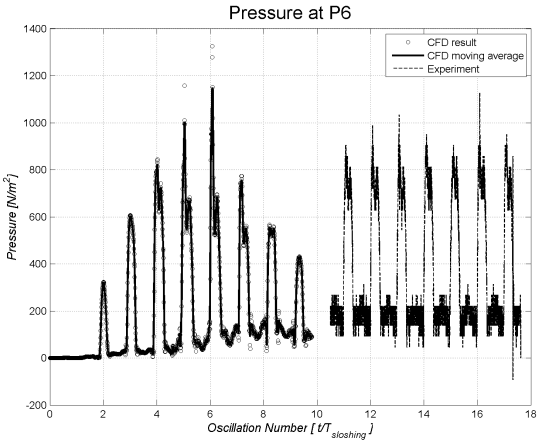

6.8(b): Pressure at P6

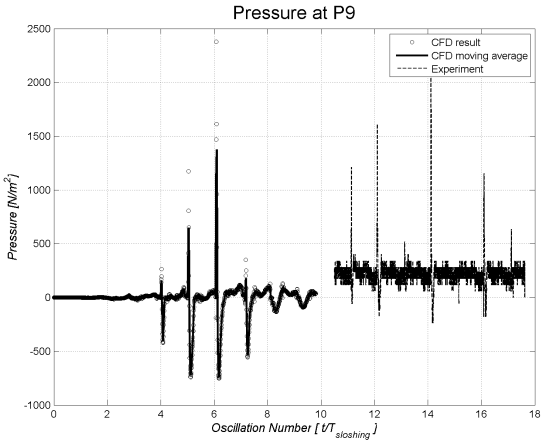

6.8(c): Pressure at P9

Figure 6.8: Pressure History using the SSG Reynolds stress model

6.3.3 Reynolds Stress Model Results

The Reynolds stress model was computationally far more demanding than the $k-\epsilon$ model for reasons explained in section 3.3.3. A computational time of 107.7 hrs was required for the first 6.9 sec of data compared to 15.8 hrs when using the $k-\epsilon$ model. This near order of magnitude increase makes the SSG Reynolds stress model difficult to justify. Only the first 10 sloshing oscillations are available, however as this first transient phase tends to be the computationally most difficult it is judged a sufficient basis of comparison. The pressure results measured at P4, P6 and P9 are not as smooth as those obtained with the $k-\epsilon$ model. The impact peaks at P9 depicted in figure 6.8(c) are considerably higher.

The Reynolds stress model was very sensitive to the grid and timestep choice and convergence was difficult to achieve throughout the simulation. Thus a better quality grid compared to the $k-\epsilon$ turbulence model is required. The ideal timestep control was identified using a trial and error approach. The most stable Courant number criterion was found to be C_N, $_{rms} \leq 0.2$ with a maximum of no more than ten coefficient iterations during the most violent flow phases. Even small deviations from these control parameters resulted in the simulation terminating.

6.4 Comparison and Analysis

6.4.1 Laminar v $k-\epsilon$ Turbulence Model

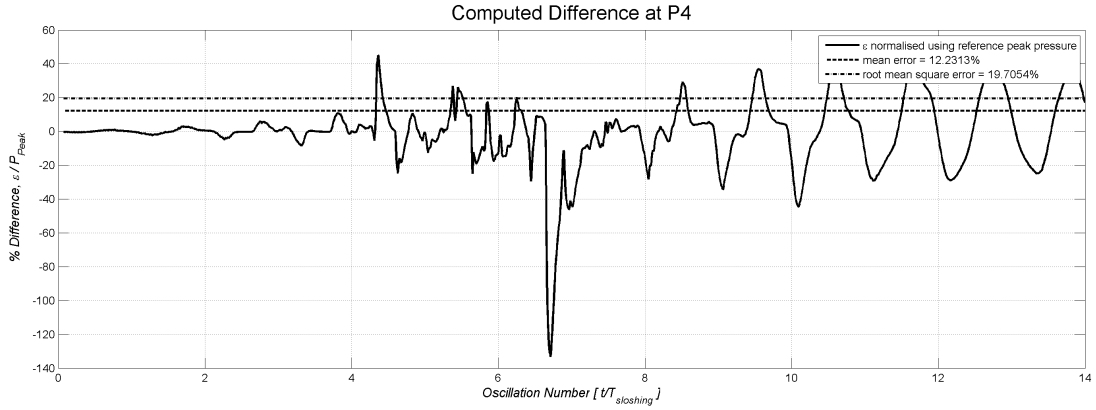

6.9(a): Pressure Difference at P4

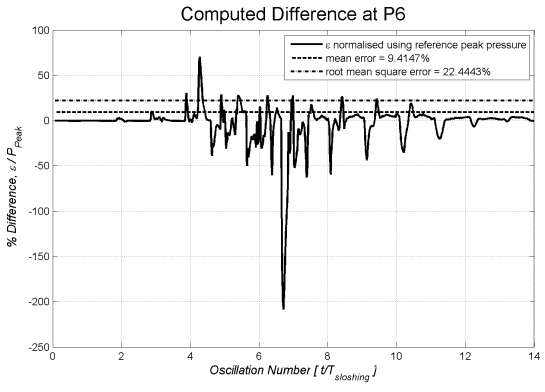

6.9(b): Pressure Difference at P6

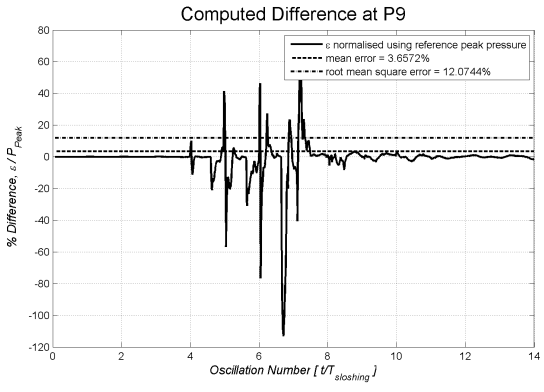

6.9(c): Pressure Difference at P9

Figure 6.9: Pressure Differences between laminar and turbulent fluid model at P4, P6 and P9 using an incompressible fluid model on grid 2

As expected from the discussion in section 6.2.2, the agreement at P4 in the transient region is reasonably good. However, once the flow starts to progress into the steady state phase, the disagreement between the two flows becomes more significant, culminating in a periodic difference of 20% amplitude, as delineated in figures 6.10(a) and 6.10(c). The higher pressure monitoring points P6 and P9 show significant differences in the transient phase.

The pressure force difference at the south wall is less significant, but the low percentage may well be attributable to the higher peak pressure. Given the poor grid convergence exhibited by the laminar fluid model as well as the difference between laminar and turbulent results once the flow starts to progress toward the steady state, it appears the laminar model is not suitable for this sloshing problem. This agrees with the physical understanding of the fact that the flow mixing process will act as a strong source of turbulence.

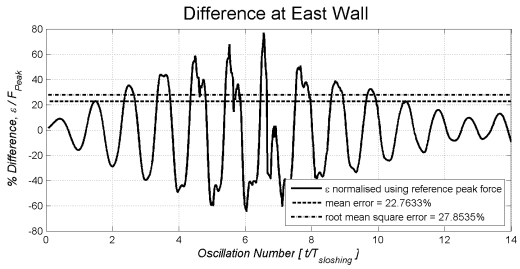

6.10(a): % Difference at East Wall

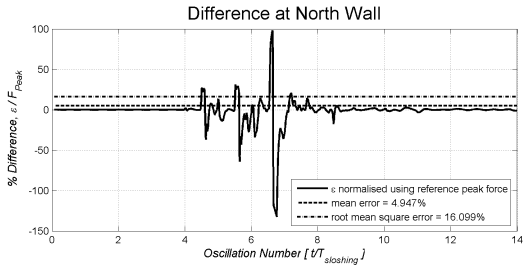

6.10(b): % Difference at North Wall

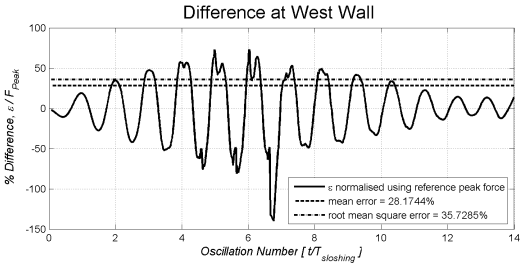

6.10(c): % Difference at West Wall

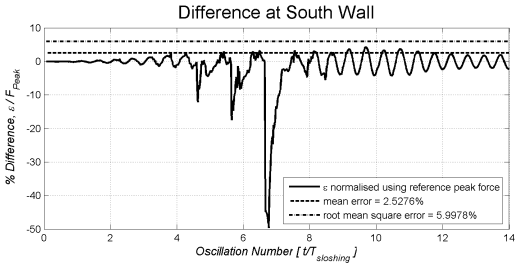

6.10(d): % Difference at South Wall

Figure 6.10: Pressure force difference between laminar and turbulent fluid model

6.4.2 $k - \epsilon$ v SSG Reynolds Stress Turbulence Model

This section considers two sets of results. First the pressures obtained with a single velocity field are used for comparing the performance of the two turbulence models. Then the same comparison is carried out using two separately calculated velocity fields for water and air,

that is multiphase flow. In both cases the grid is identical and all computational parameters are kept constant. The $k - \epsilon$ model is used as the benchmark.

Single Phase Solution

When using the single velocity field there is significant disagreement between the two turbulence models. The Reynolds stress model appears to underestimate the pressure at the sloshing peak. The discrepancies amount up to 40% at P4, indicated in figure 6.11(a). The differences at P6 and P9 given in figures 6.11(b) and 6.11(c) respectively is even more significant. Especially at P9, where the water impact is severe, the disagreement between results is in excess of 100%. Note that the error between the models does not decay as the simulation moves past the initial transient phase, this is illustrated in figure 6.11(a).

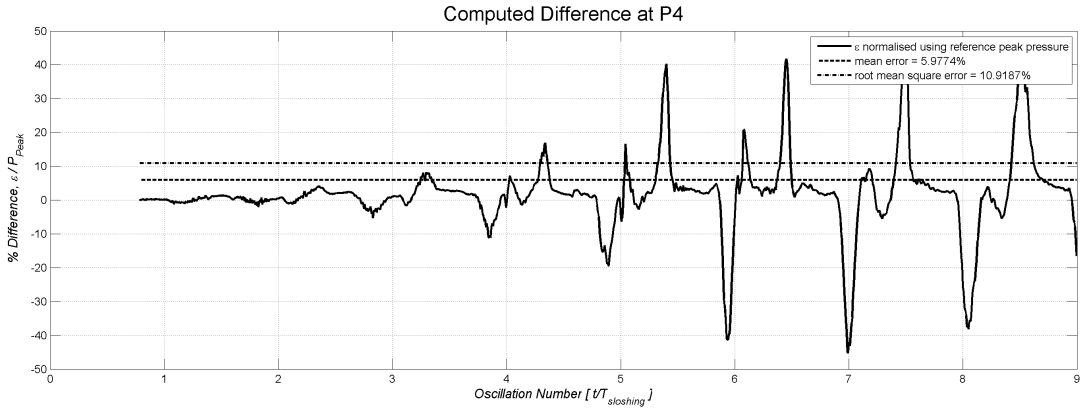

6.11(a): Pressure Difference at P4

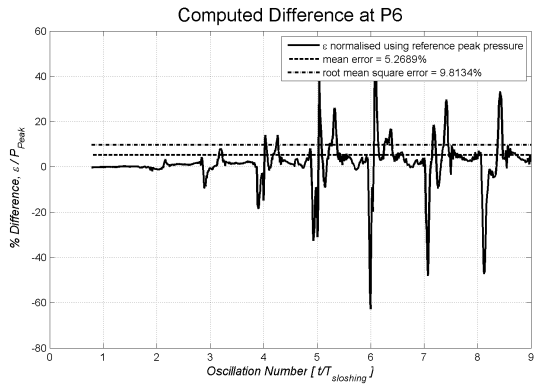

6.11(b): Pressure Difference at P6

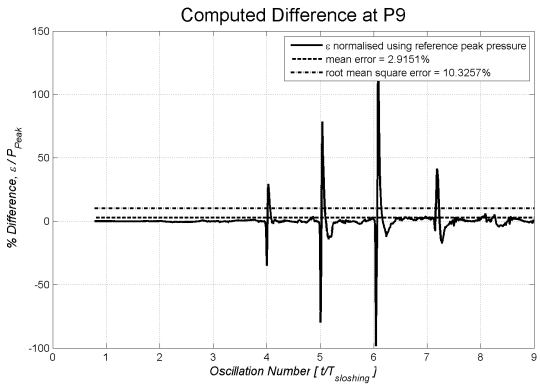

6.11(c): Pressure Difference at P9

Figure 6.11: Pressure Differences between $k - \epsilon$ and Reynolds Stress Model using a single phase model

Multi Phase Solution

As shown in figure 6.12, the difference in pressure history is now significantly less, the mean error is reduced by approximately 70% and the error decays as the flow moves out of the initial transient region. The peaks in pressure difference are reduced significantly as well, although the SSG model produces a lower pressure at both P4 in figure 6.12(a) and P6 in figure 6.12(b). However, at P9 the peak impact pressure calculated with the SSG model is significantly higher.

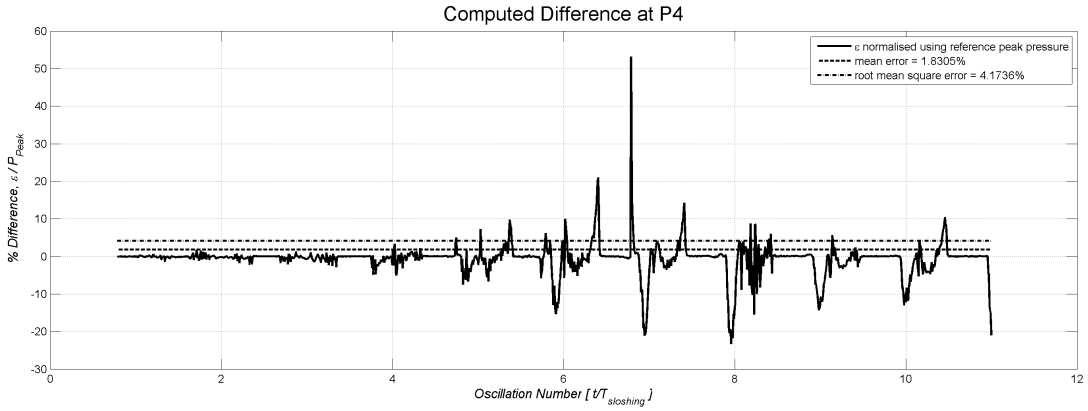

6.12(a): Pressure Difference at P4

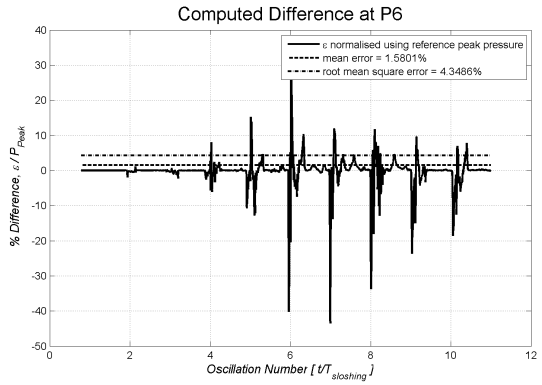

6.12(b): Pressure Difference at P6

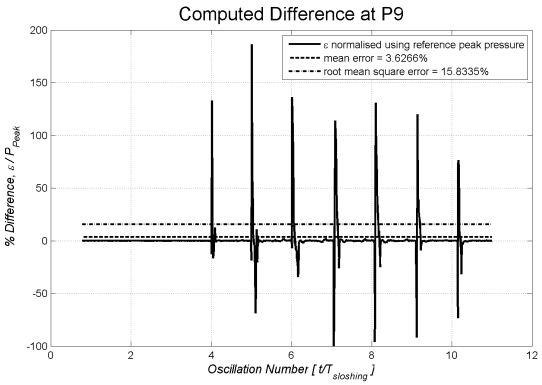

6.12(c): Pressure Difference at P9

Figure 6.12: Pressure Differences between $k - \epsilon$ and Reynolds Stress Model using a multi phase model

6.5 Recommendations

The above results leave little doubt that the sloshing flow should be considered as turbulent for CFD simulations of practical significance. The results given by the laminar flow model do

Table 6.1: Summary of results analysis for turbulence model variations

Model	**Reference**	**Pressure**			**Wall Pressure Force**			
		P4 [%]	P6 [%]	P9 [%]	North [%]	East [%]	South [%]	West [%]
Laminar, Grid 1	Laminar, Grid 2	9.83	9.59	6.83	30.1	5.82	2.45	6.30
	(RMS)	18.7	23.6	22.1	100	12.3	6.07	12.3
o-Grid	SSG Grid 2	2.78	3.53	0.90				
	(RMS)	4.31	8.80	3.51				
o-Grid	SSG Grid 3	2.50	3.01	0.62				
	(RMS)	4.81	8.71	3.30				
Laminar, Grid 2	$k-\epsilon$, Grid 2	12.2	9.41	3.66	4.95	22.8	2.53	28.2
	(RMS)	19.7	22.4	12.1	16.1	27.9	6.00	35.7
SSG	$k-\epsilon$, o-Grid	5.98	5.27	2.92	single phase			
	(RMS)	10.9	9.81	10.3				
SSG	$k-\epsilon$, o-Grid	1.83	1.58	3.63	multiphase			
	(RMS)	4.17	4.35	15.8				

not appear consistent with the physics of the problem as well as the nature of the flow being studied. Therefore it should not be used unless the Reynolds number describing the flow is sufficiently low. However, in that case, simpler fluid models or even pendulum models often appear to be sufficient [66].

The results given in figure 6.12 seem to suggest that a multiphase approach to the sloshing problem produces significantly different results to those of the single phase model. However, the computational costs of the multiphase approach are considerably higher, as twice the number of equations have to be solved for this two-phase problem. Further investigations will be carried out using the multiphase model. Given the properties of natural gas in the insulated tank, the multiphase approach may be unavoidable due to the interphase mass transfer and dynamic interaction between the phases.

Considering the two turbulence models, the SSG model is not practical for further use due to the increased computational requirements as well as the sensitivity of this model to the grid and time step. The $k - \epsilon$ model offers the best trade-off between accuracy of result, consistent physics and computational time. Therefore, it is recommended that this model be used for most sloshing flows.

7 Fluid Model Comparison

7.1 Background

Given the number of different fluid models available as well as no definitive guide available for choosing the correct one, this section seeks to identify the most accurate combination with the smallest computational requirements. The most complex fully compressible fluid model and experimental data are used as benchmark for comparing other results. It is possible to simplify the problem by restricting the simulation to include water only. For the purpose of this study a single pressure and velocity field is used. Separate velocity fields lead to the field of multiphase flow modelling which is beyond the scope of this study.

7.2 Single & Multi-Fluid Simulation

Treating this problem using a single fluid with a preset, usually atmospheric, pressure at the free surface is the earliest and simplest application of the Volume of Fluid method to free surface problems [67]. However, section 2 highlighted the influence of the second phase on the sloshing flow. There is a strong indication that air, the second fluid, must be included as a matter of principle. Fortunately, this issue has been addressed in greater detail by Wemmenhove *et al* [68], where the performance of a single and multi fluid simulation is compared to experimental data. While the flow investigated is a collapsing water column rather than a sloshing flow, the results obtained in this study are highly instructive.

Examining figure 7.1, the severe pressure spikes resulting from the single fluid model are immediately apparent. This is consistent with data presented for the fully incompressible case in section 7.3.4, where the damping effect of air was reduced. For a single fluid this damping effect is eliminated completely and unrealistic pressure peaks appear. Moreover, the initial impact load is underestimated when compared to experimental values to an even greater extent than with the multi fluid model. In addition to the previous argument, most contemporary studies of sloshing using a Navier Stokes CFD code, e.g. Hadzic [57] and Rhee [59] include two fluids in the simulation. Therefore, despite the greater computational effort required, the inclusion of all fluids occupying the physical domain appears to be a prerequisite for obtaining a useful solution. Consequently, the current study will not attempt to confirm

this as the existing evidence is sufficient.

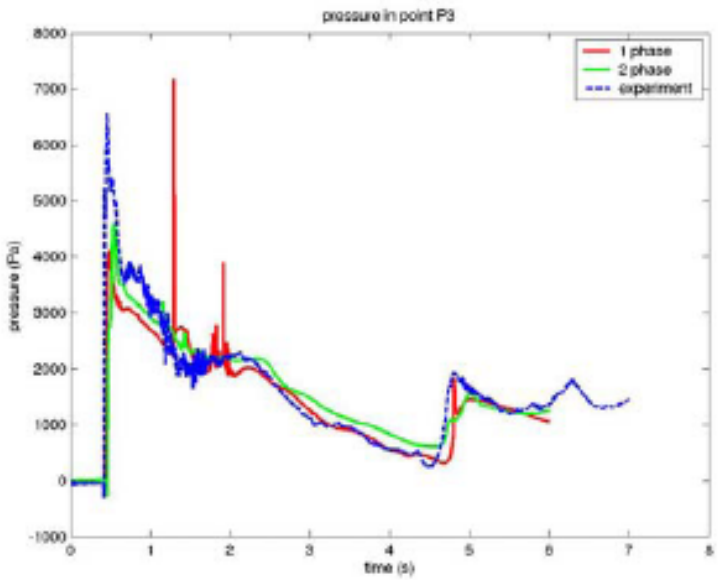

Figure 7.1: Single & multi fluid pressure history for collapsing water column (from Wemmenhove *et al* [68]) Blue: experiment, Red: single fluid, green: multi fluid

7.3 Compressibility Model Results

Having established the need to include both fluids in the sloshing problem, it is now necessary to identify the most suitable model for each fluid. The choice is between incompressible flow, governed by equation (3.1) and compressible flow governed by equation (3.2). Clearly the compressible flow model is computationally more intensive, thus it should be used only where necessary. Recalling the physics of the problem, the most suitable approximation would appear to be the use of an incompressible model for water, while air is treated as a compressible fluid. As will be shown in subsequent cases, some subtle changes to the sloshing simulation have a significant impact on the results. Experimental data is provided on the pressure graphs but it is not explicitly addressed in the discussion. The comparison between computational and experimental results was carried out in the grid independence study 4. All flows are modelled using a $k - \epsilon$ turbulence model. The simulations were carried out on grid 2 specified in section 4. A first order time-marching scheme with dynamic time step control with a root mean square Courant number limit of 0.1, was used to discretise the problem in the time domain.

7.3.1 Incompressible Water & Compressible Air

Pressure

The first result considered is using a compressible model for air and an incompressible model

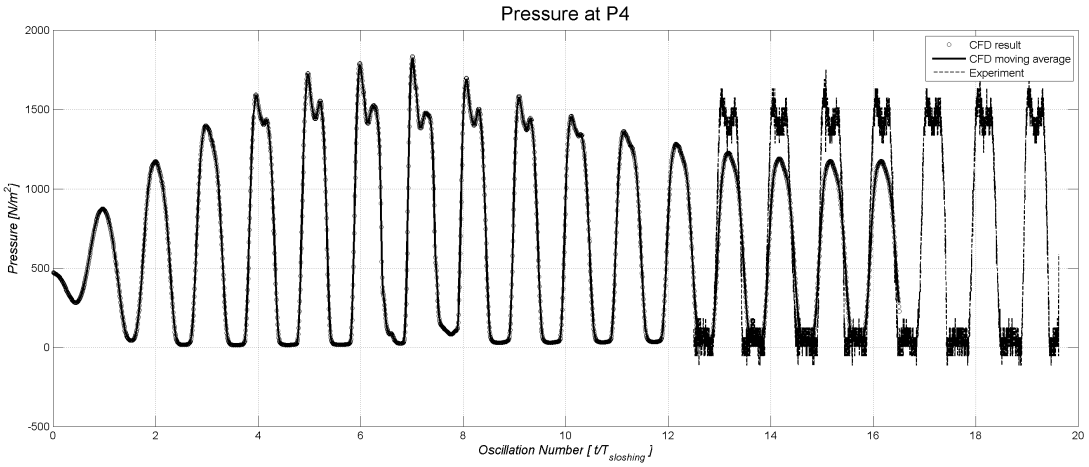

7.2(a): Pressure at P4

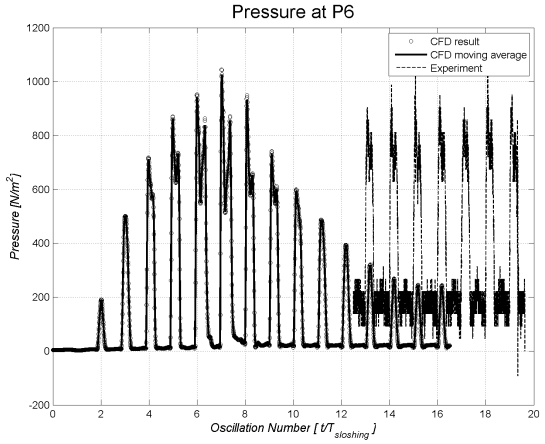

7.2(b): Pressure at P6

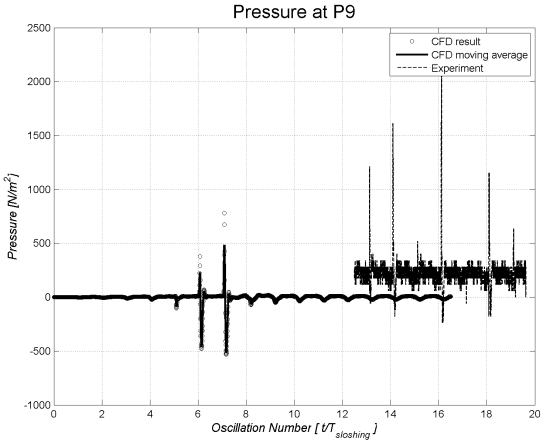

7.2(c): Pressure at P9

Figure 7.2: Pressures at P4, P6 and P9 observed during the CFX simulation using incompressible water and compressible air

for water. This combination is physically most intuitive. Pressure is presented at three locations indicated in figure 3.3; the pressure force is given for all four walls. Finally, the location of the free surface in the time domain is given in figure 7.4.

- Figure 7.2(a) shows the pressure at P4, the shape of the pressure peaks is consistent with the fluid striking the north tank wall in the transient phase. As the flow approaches

the steady state, the water does not reach the North wall, as shown in figure 7.2(c).

- The pressure peaks oscillation 7 and then decays again, consistent with the physics outlined in section 2.
- The pressure at P6, depicted in figure 7.2(b) resembles that of P4 with a lower peak value but larger spikes due to the water impacting the north wall.
- The pressure at P9 given in figure 7.2(c) does not follow the trend of P4 and P6, but one may immediately observe the significant spikes indicating that the fluid has in fact struck the north wall. Shown subsequently, the pressure at P9 is influenced by the choice of fluid model.

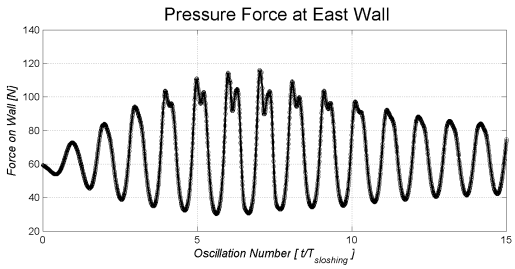

7.3(a): Force at East Wall

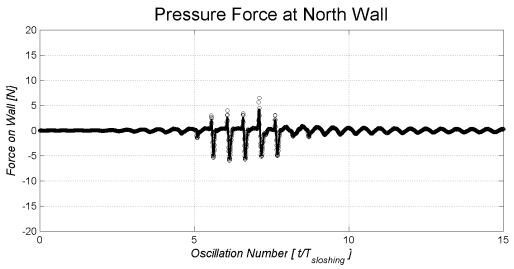

7.3(b): Force at North Wall

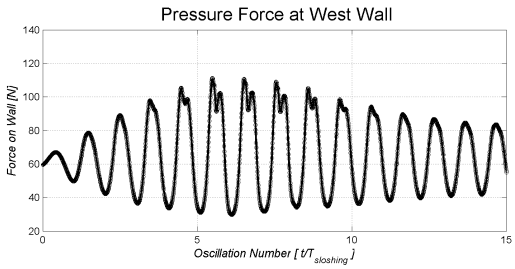

7.3(c): Force at West Wall

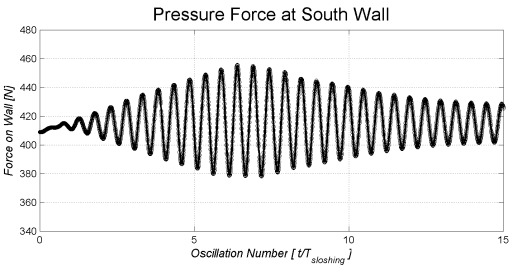

7.3(d): Force at South Wall

Figure 7.3: Pressure force on sloshing container [N] using incompressible water and compressible air

Force

The pressure force histories depicted in figure 7.3 shows an extended period of 15 sloshing oscillations:

- The pressure force at the East and West walls, given in figures 7.3(a) and 7.3(c) respectively, are anti-symmetric as expected.

- The impact shape observed previously in in figure 7.2 can also be observed at the side wall force plots.
- The South wall force, oscillating between 380 N and 460 N compares reasonably to the static pressure force of approximately 420 N
- The first transient phase lasting the first 10 oscillations is well defined in all four force plots
- While the force on the North wall illustrated in figure 7.3(b) is small relative to the others, the peaks are considerably sharper.

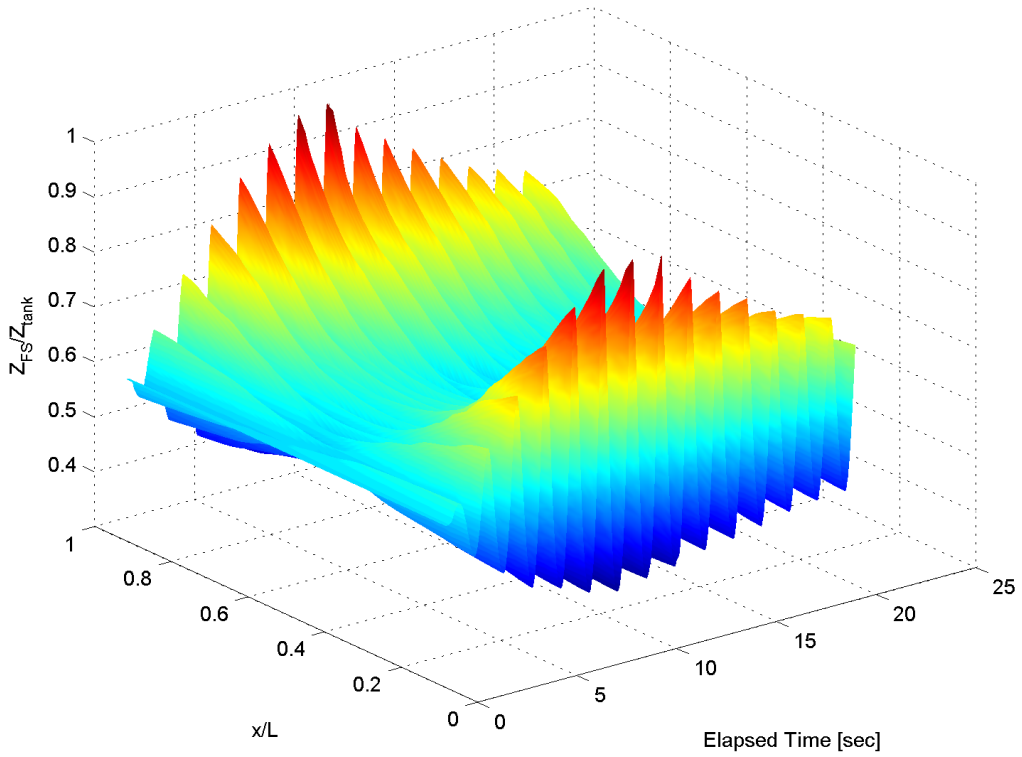

Figure 7.4: Free surface observed during the CFX simulation using incompressible water and compressible air

Free Surface

The position of the free surface is illustrated in figure 7.4, with time introduced as a third

dimension. The free surface elevation shows the initial transient phase in the first 10 oscillations, analogous to the behaviour observed in the pressure and force histories. The free surface location is not shown for all model combinations, but is used for comparison in the subsequent analysis.

7.3.2 Compressible Water & Compressible Air

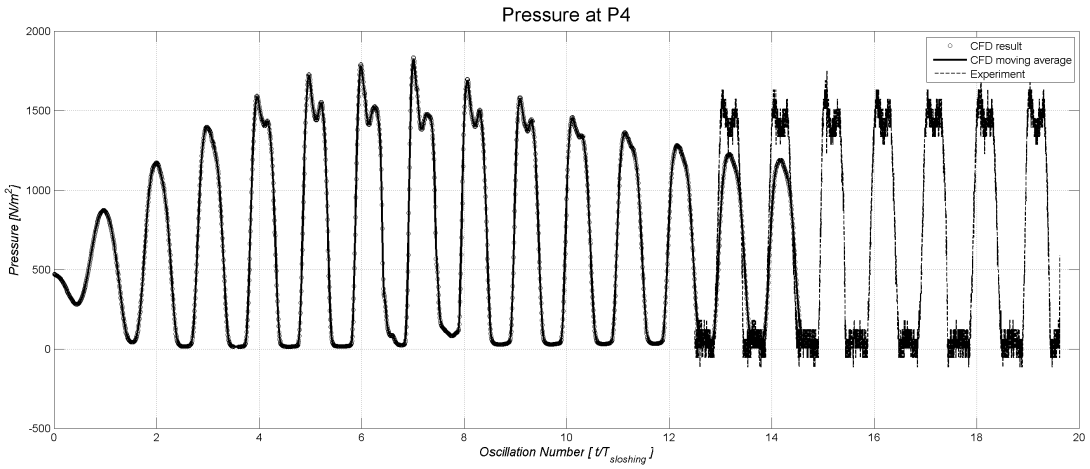

7.5(a): Pressure at P4

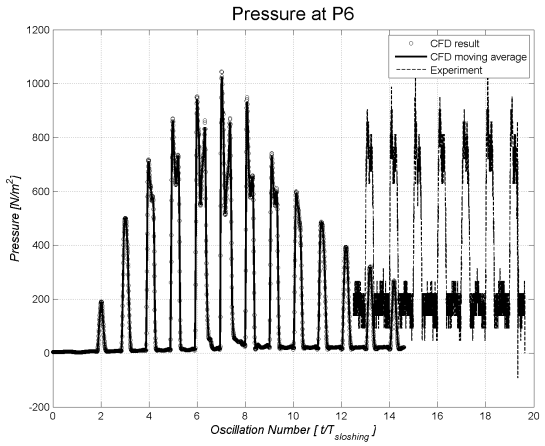

7.5(b): Pressure at P6

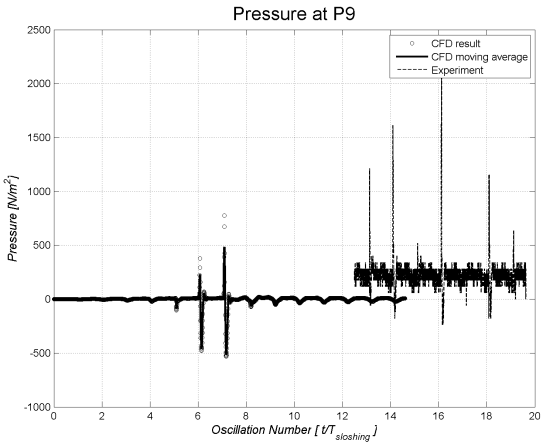

7.5(c): Pressure at P9

Figure 7.5: Pressures at P4, P6 and P9 observed during the CFX simulation using compressible water and compressible air

This section examines the result obtained with a compressible fluid model for both air and water. This case will be used as a basis for comparing all others as it is the most

general. All computational parameters other than the compressibility settings, such as grid and convergence criteria are the same as in the other simulations. The computational cost of using compressibility for both water and air caused an increase in required CPU time by slightly more than 20%. Thus it is well worth studying the potential benefits of including more complex fluid models.

Pressure

- The pressure history at P4 shown in figure 7.5(a) exhibits the characteristic shape of the North wall being hit by water as in the previous figure 7.2(a)
- The plots in figures 7.5(b) and 7.5(c) for P6 and P9 respectively are very similar to those obtained using incompressible water.

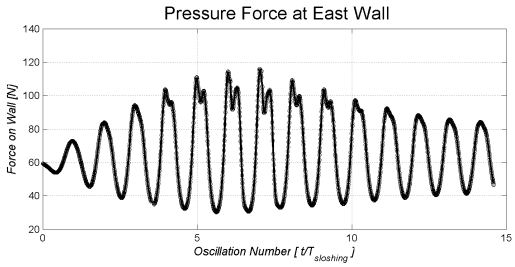

7.6(a): Force at East Wall

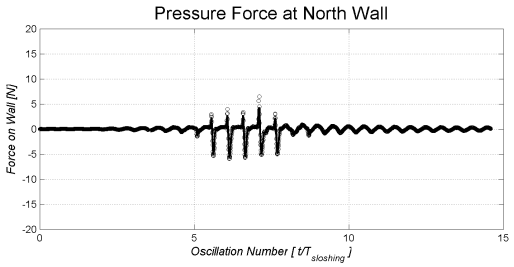

7.6(b): Force at North Wall

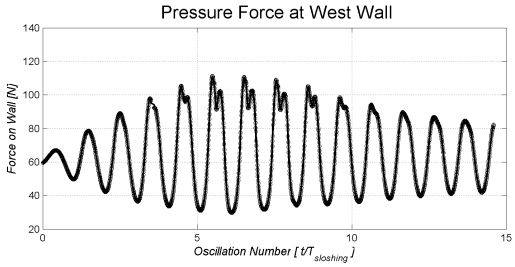

7.6(c): Force at West Wall

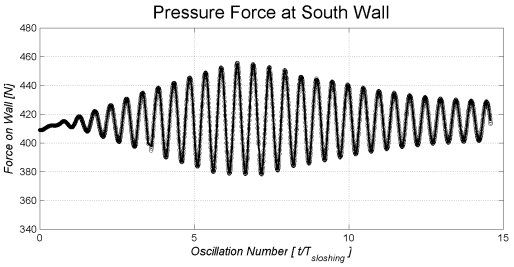

7.6(d): Force at South Wall

Figure 7.6: Pressure force on sloshing container [N] using compressible water and compressible air

Force

The force plots given in figure 7.6 are nearly identical to those in figure 7.3. Again, one may observe the anti-symmetry between figure 7.6(a) and figure 7.6(c), giving the pressure force at the East and West wall respectively. The initial peaks during an oscillation are slightly

higher and more pronounced at the East wall. This was not observed in the previous section 7.3.1.

Free Surface

The free surface plot is similar to the previous case. The free surface peaks appear slightly

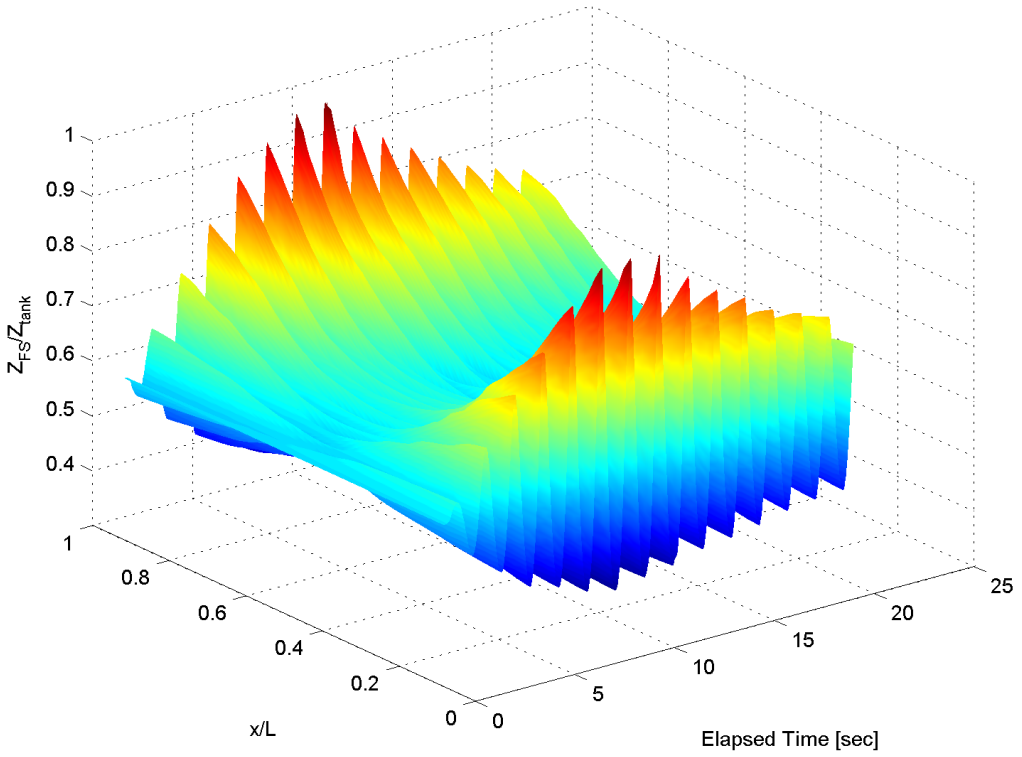

Figure 7.7: Free surface observed during the CFX simulation using compressible water and compressible air

higher at $x/L = 1$, (the East wall), confirming the observations in figure 7.6. It should be emphasised that the differences between the two results are very small, as will be shown later in section 7.4.

7.3.3 Compressible Water & Incompressible Air

This combination is rather counter-intuitive, it is included to confirm the importance of assigning the compressibility model to the physically most appropriate fluid, namely air rather than water. Another motivation is to provide a comprehensive study of all possible options. As there are no readily discernable differences in the free surface configuration, the free surface plot is omitted for this model combination, although it is compared to the free surface obtained from the fully compressible fluid model in section 7.4.3.

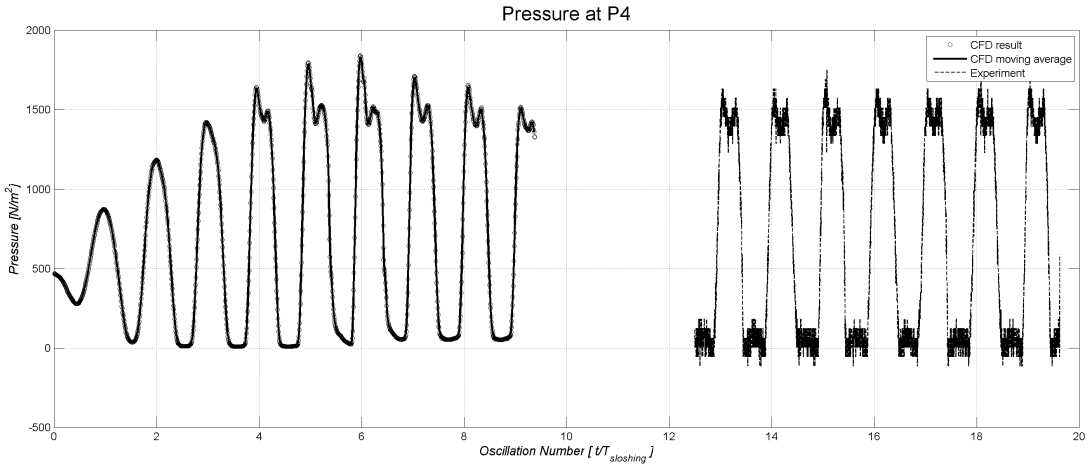

7.8(a): Pressure at P4

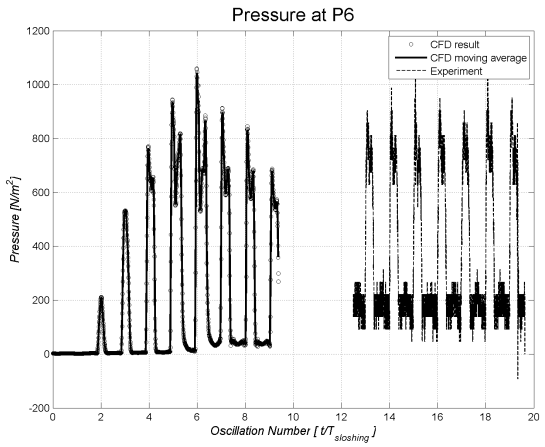

7.8(b): Pressure at P6

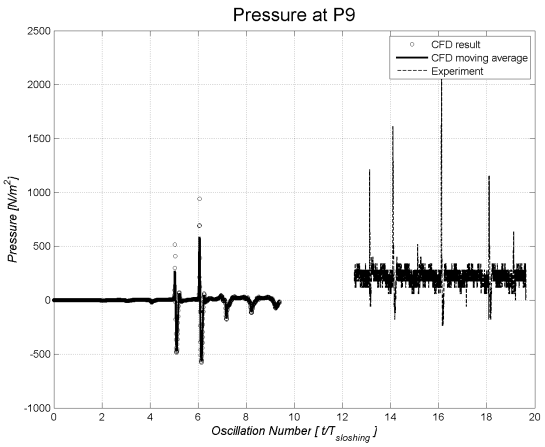

7.8(c): Pressure at P9

Figure 7.8: Pressures at P4, P6 and P9 observed during the CFX simulation using compressible water and incompressible air

Pressure

The pressure histories given in figure 7.8 are generally similar to those obtained using full incompressibility. However one may observe the sharper pressure peaks at P9 in figure 7.8(c). The pressure plot for P6 in figure 7.8(b) is also sharper than in previous runs. This may be attributed to neglecting the compressibility of air which damps the more impulsive motions.

Force

The force acting on the container walls, illustrated in figure 7.9, broadly agrees with full

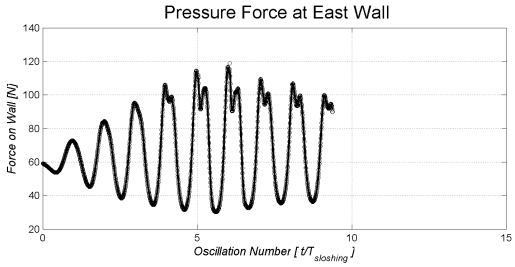

7.9(a): Force at East Wall

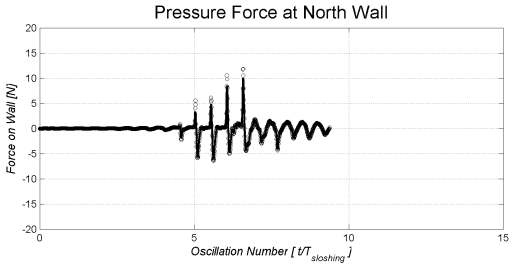

7.9(b): Force at North Wall

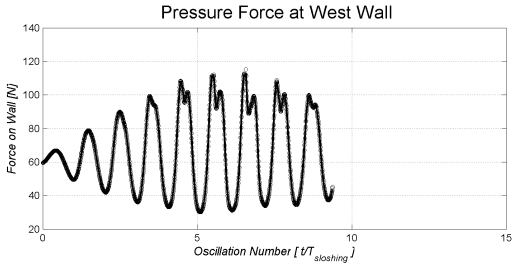

7.9(c): Force at West Wall

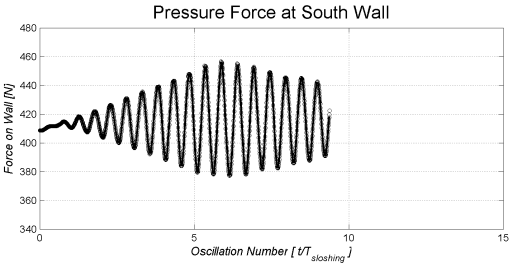

7.9(d): Force at South Wall

Figure 7.9: Pressure force on sloshing container [N] using compressible water and incompressible air

compressibility, but the observations made in the previous paragraph apply again. The force on the north wall given in figure 7.9(b) has considerably higher peaks than when using a compressible fluid model for air.

7.3.4 Incompressible Water & Incompressible Air

This combination is the usual choice of fluid model for most naval architecture applications. It is also the simplest and computationally least expensive as only the incompressible Navier Stokes equations have to be solved, neglecting the energy equation (3.2c) and nonlinear terms

involving density in equation (3.2). Note that the free surface time history is not presented for this combination, comparisons are given in section 7.4.3.

Pressure

Figure 7.10 illustrates the pressures observed using incompressible fluid. Again, the pressure

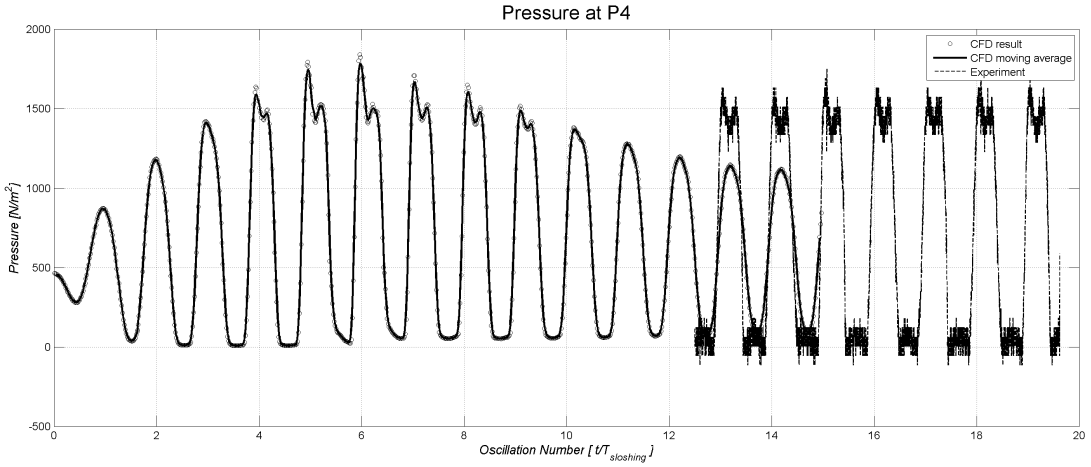

7.10(a): Pressure at P4

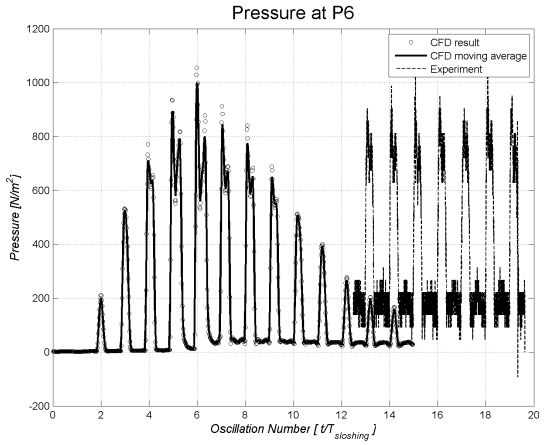

7.10(b): Pressure at P6

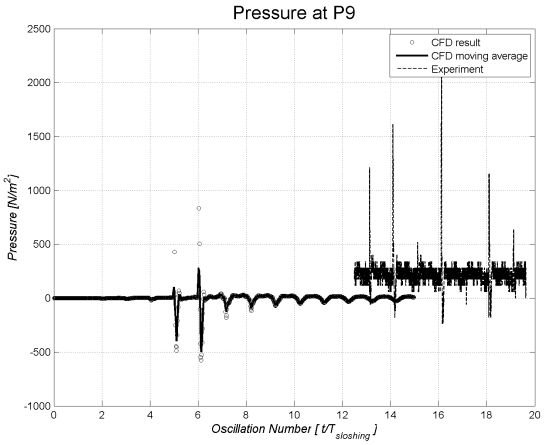

7.10(c): Pressure at P9

Figure 7.10: Pressures at P4, P6 and P9 observed during the CFX simulation using incompressible water and incompressible air

peaks typical of fluid striking the container north wall are clearly visible. However, the pressure peaks at P9 delineated in figure 7.10(c) compare far better to the full compressibility model shown in figure 7.5(c). Other than that, no significant difference are apparent in the transient region.

Force

The force plot for the fully incompressible model extends past the transient region, and one

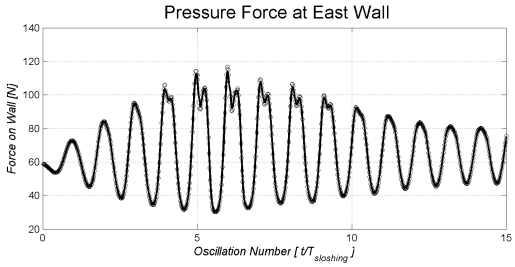

7.11(a): Force at East Wall

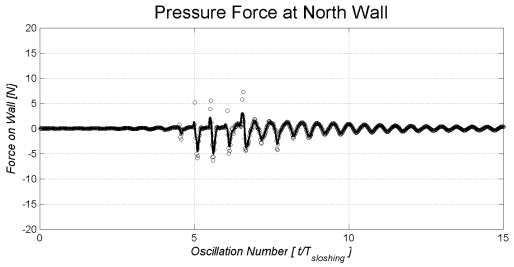

7.11(b): Force at North Wall

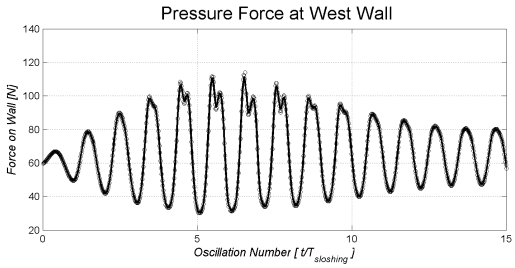

7.11(c): Force at West Wall

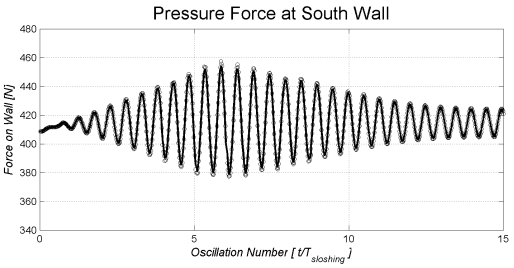

7.11(d): Force at South Wall

Figure 7.11: Pressure force on sloshing container [N] using incompressible water and compressible air

may observe the significantly lower wall force past the initial transient stage in figure 7.11. The side wall force peaks given in figures 7.11(a) and 7.11(c), for the East and West walls respectively are 18% lower than those using a compressible fluid model. This illustrates the significance of using a compressible fluid model.

7.4 Compressibility Model Comparison and Analysis

It is now useful to compare the results and identify the most effective model combination. The most general case, a compressible fluid model for both water and air, is used as a basis for comparison. As in the previous section, pressure at the indicated reference points, wall pressure force and free surface position are used to compare the data. Note that only the first 9 oscillations of the initial transient phase are used to compare compressibility results. Results are normalised using the peak pressure obtained from full compressibility at each location. The error ϵ is defined as

$$\epsilon = \phi_{observed} - \phi_{reference} \tag{7.1}$$

for each data set, where ϵ is the error, $\phi_{observed}$ data from the current run and $\phi_{reference}$ data from the reference run. Typically, ϵ is normalised as

$$\acute{\epsilon} = \frac{\epsilon}{\phi_{reference,\ max}}, \tag{7.2}$$

where $\phi_{reference,\ max}$ is the reference data peak at a particular location. Note that the mean error uses the magnitudes of ϵ_n at each timestep.

7.4.1 Pressure Results

Considering the differences in pressure at P4, shown in figure 7.12, it is apparent that the pressure history obtained using an incompressible model for water and a compressible model for air is nearly identical to the fully compressible solution. Therefore, assigning a compressibility model to water is not required. Modelling the entire problem with the incompressible Navier Stokes equations produces some differences to the fully compressible reference case shown in figure 7.12(b). The mean error of 2.8% is considerably higher than in the previous case. More importantly, the peaks are underestimated by as much as 15%. Setting water to be the compressible fluid and air incompressible results in some disagreement to the reference case, as seen in figure 7.12(c) results in a slightly smaller mean error with a similar variation in pressure peaks of about ±15%.

These trends are confirmed in figure 7.13 giving the pressure differences at P6 and P9. The figures 7.13(a) and 7.13(b) show nearly identical results for the incompressible water model

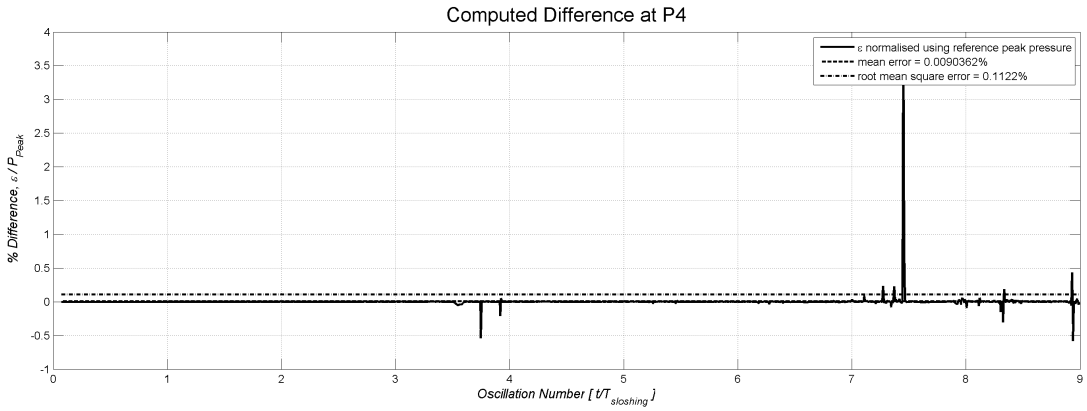

7.12(a): Incompressible Water, Compressible Air

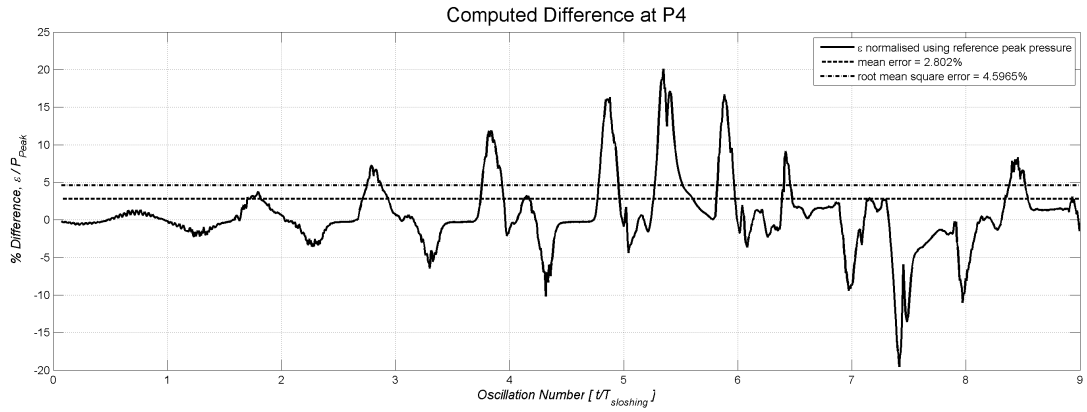

7.12(b): Incompressible Water, Incompressible Air

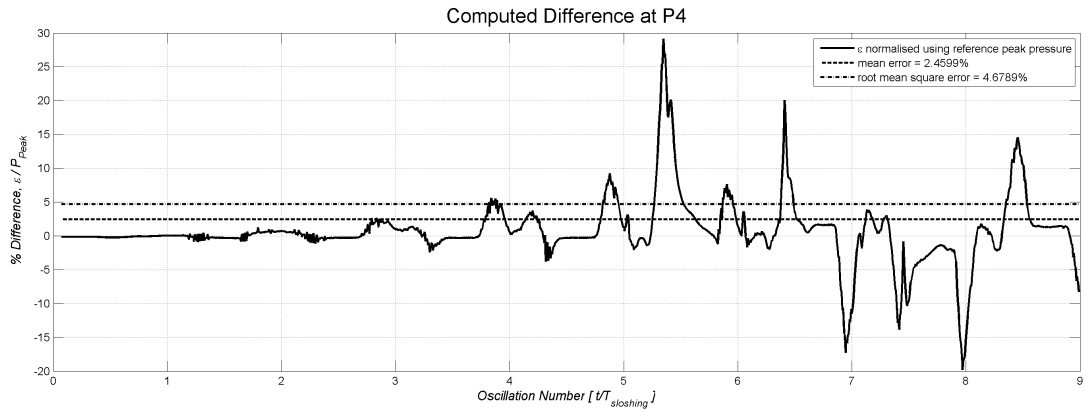

7.12(c): Compressible Water, Incompressible Air

Figure 7.12: Pressure differences at P4

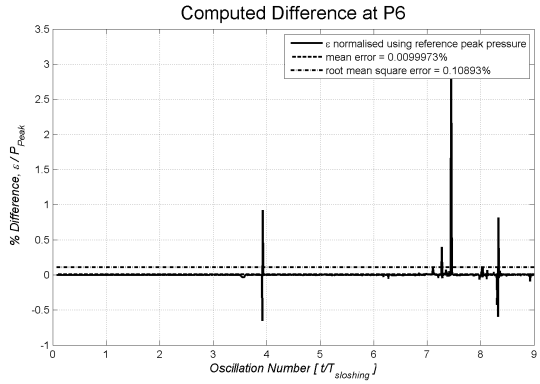

7.13(a): Incompressible Water, Compressible Air

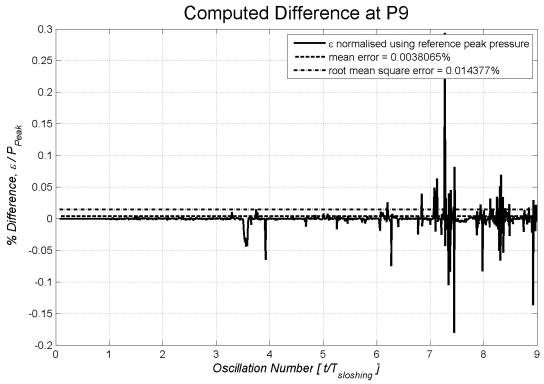

7.13(b): Incompressible Water, Compressible Air

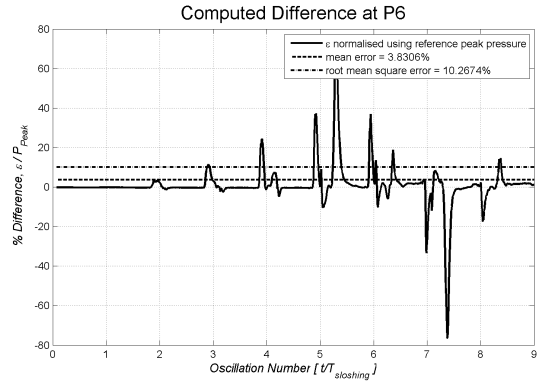

7.13(c): Incompressible Water, Incompressible Air

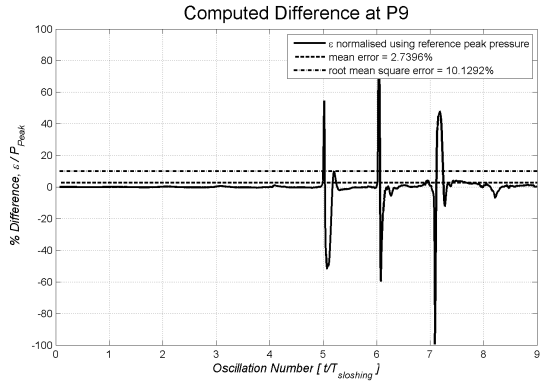

7.13(d): Incompressible Water, Incompressible Air

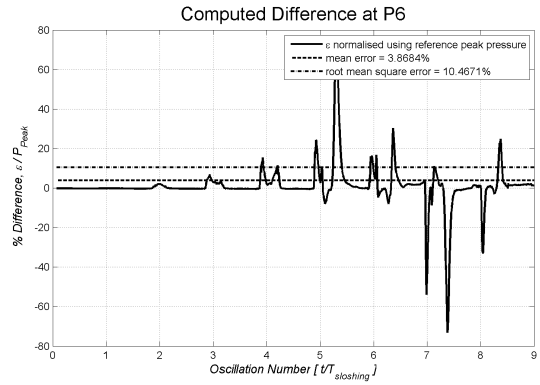

7.13(e): Compressible Water, Incompressible Air

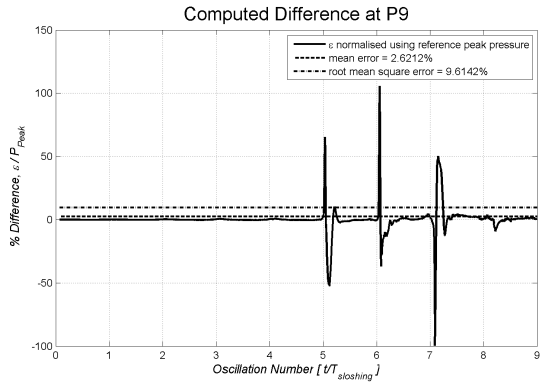

7.13(f): Compressible Water, Incompressible Air

Figure 7.13: Pressure differences at P6 (left column) and P9 (right column)

and compressible air model compared to the benchmark case. The mean errors for the other two cases are about 50% greater than at P4. Errors peak near 60% of the baseline value, indicating that the last two fluid model combinations are not suitable.

7.4.2 Wall Pressure Force

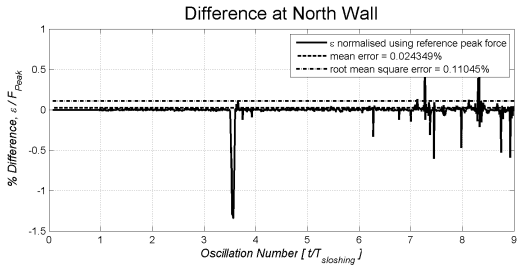

7.14(a): Incompressible Water, Compressible Air

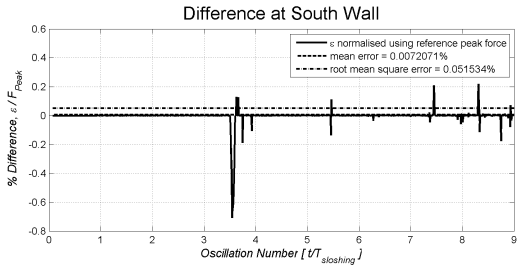

7.14(b): Incompressible Water, Compressible Air

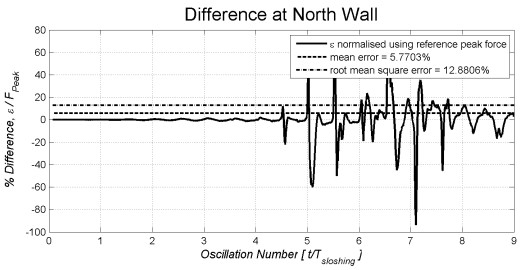

7.14(c): Incompressible Water, Incompressible Air

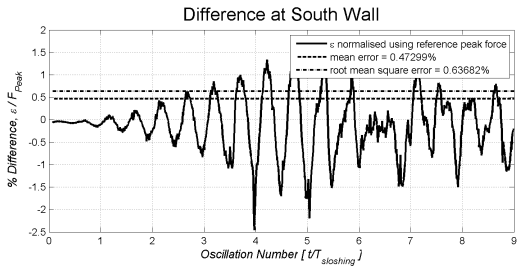

7.14(d): Incompressible Water, Incompressible Air

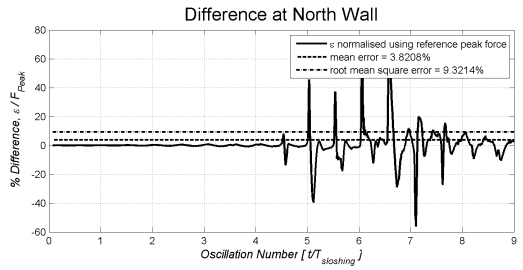

7.14(e): Compressible Water, Incompressible Air

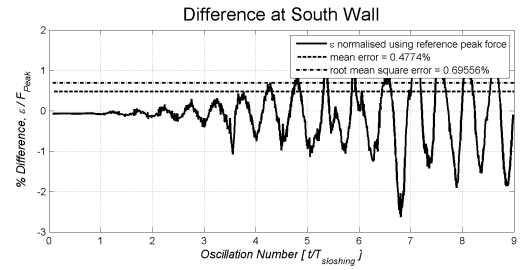

7.14(f): Compressible Water, Incompressible Air

Figure 7.14: Wall pressure force differences at North (left column) and South (right column) wall

The wall pressure forces show an error distribution similar to the pressure points examined above. The results for the incompressible water, compressible air combination match the fully compressible result very well, with a mean error of the order of 10^{-2}%. The errors at the East and West walls, indicated in figure 7.15, are of similar magnitude as the pressure error peaks. There appears to be a high frequency error component rather than a consistent steady state

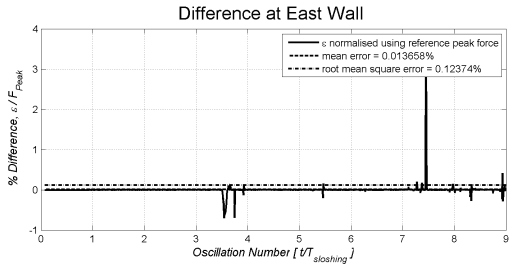

7.15(a): Incompressible Water, Compressible Air

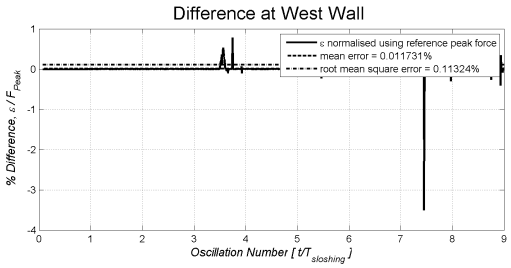

7.15(b): Incompressible Water, Compressible Air

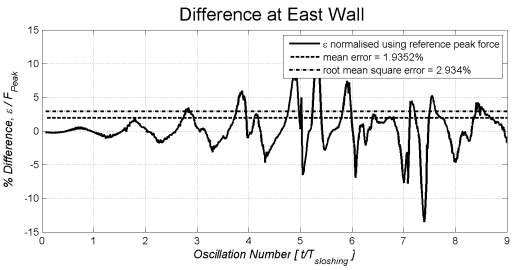

7.15(c): Incompressible Water, Incompressible Air

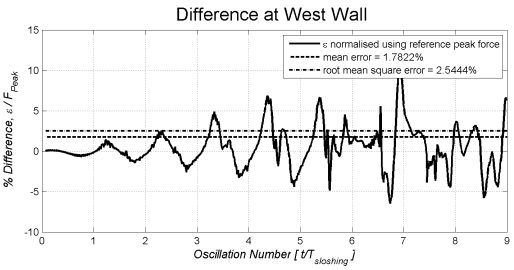

7.15(d): Incompressible Water, Incompressible Air

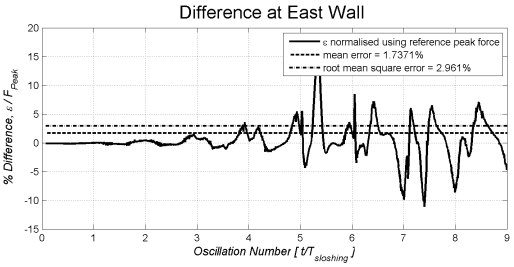

7.15(e): Compressible Water, Incompressible Air

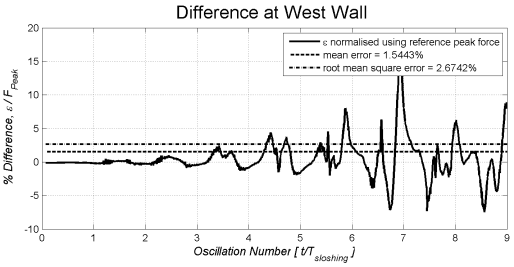

7.15(f): Compressible Water, Incompressible Air

Figure 7.15: Wall pressure force differences at East (left column) and West (right column) wall

error. However, as these errors may influence the further time evolution of the flow, the last two fluid models are not suitable for modelling the current sloshing problem.

7.4.3 Free Surface Elevation

The free surface errors illustrated in figure 7.16 confirm the previous results. The nearly flat surface shown in figure 7.16(a) indicates very good agreement between the chosen fluid models in space as well as time. The free surface positions obtained from the fully incompressible model as well as the compressible water, incompressible air model disagree with the benchmark case as the sloshing motion becomes more violent both spatially and throughout the time domain.

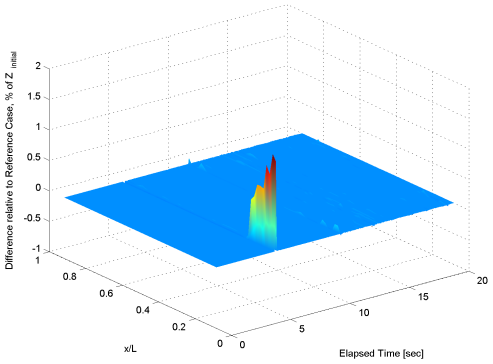

7.16(a): Free surface difference observed using incompressible water and compressible air

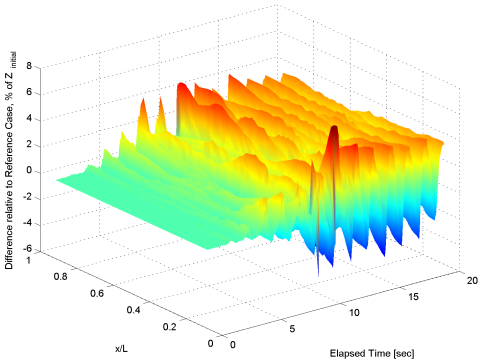

7.16(b): Free surface difference observed using incompressible water and incompressible air

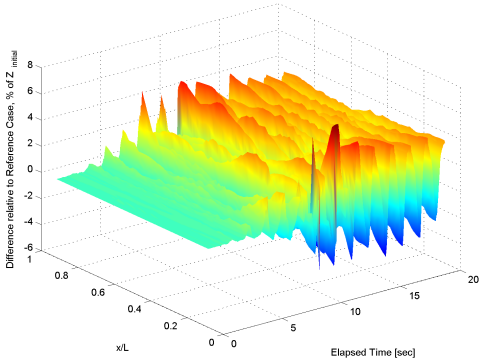

7.16(c): Free surface difference observed using compressible water and incompressible air

Figure 7.16: Difference in free surface relative to compressible water and compressible air

7.5 Recommendations

Having compared the different fluid model combinations it was found that, in line with the physics of the problem, applying a compressible model to air while considering water incompressible provides a solution nearly equivalent to the computationally more costly use of equation (3.2) for both fluids. Using a fully incompressible fluid model, however, does not appear to be sufficiently accurate as pressures tend to be different by as much as $\pm 60\%$.

Similarly, the use of compressible water and incompressible air turned out to be a misrepresentation of the flow physics with significant errors in the obtained pressures. Therefore, the result from this investigation is that when modelling a sloshing problem involving water

Table 7.1: Summary of results analysis for compressibility model variations

Model	**Reference**	**Pressure**			**Wall Pressure Force**			
		P4 [%]	P6 [%]	P9 [%]	North [%]	East [%]	South [%]	West [%]
Incompressible Water,	Fully Compressible	0.01	0.01	0.004	0.02	0.01	0.01	0.01
Compressible Air	(RMS)	0.11	0.11	0.014	0.11	0.12	0.05	0.11
Incompressible Water,	Fully Compressible	2.80	3.83	2.74	5.77	1.94	0.47	1.78
Incompressible Air	(RMS)	4.60	10.3	10.1	12.9	2.93	0.64	2.54
Compressible Water,	Fully Compressible	2.60	3.87	2.62	3.82	1.74	0.48	1.54
Incompressible Air	(RMS)	4.68	10.5	9.61	9.32	2.96	0.70	2.67

and air, the application of the more complex equation (3.2) to air only is sufficient. However, one should emphasise that a similar study may be necessary when completely changing the nature of the fluids to be modelled.

8 Conclusions

8.1 Experimental Correlation

A thorough validation study has been carried out which confirms that the use of a commercial flow solver, if the correct parameters are selected, provides an effective method of investigating lateral sloshing in LNG tanks. The computational results did not completely match the experimental data at the reference points as the pressure peaks in the steady state were often underestimated by the computational solution. This was a lesser problem at P4, where the static pressure contribution dominates. The pressure histories at P6 and P9, where the dynamic pressure contributions are more significant, were underestimated by as much as 50 %.

The periodicity of the pressure history was well maintained however, indicating that the body force approach is suitable for the CFD modelling the sloshing. This provides further confirmation of the conclusions given by Hadzic *et al* [57]. However, as the experimental data was recorded once the sloshing flow had reached a steady state the initial transient CFD solution is not a valid basis for comparison.

8.2 CFD Modelling Guidelines

Grid Study The grid independence study in section 4 was completed to establish the validity of the results irrespective of any grid used. Other motions can now be studied using the selected grids with a reasonable degree of confidence of having used a suitable grid. It must be emphasised that including a third spatial dimension would make the current problem essentially a four dimensional one, implying a prohibitive increase in computational times.

While the possibility of parallel processing exists, it introduces additional difficulties when dealing with free surface problems as the partitions must not be located at the free surface. The near wall resolution was found to be satisfactory with an initial node offset of 1 mm. Further, it was found that the quality of the pressure solution depends on a sufficient number of nodes in the near-wall region. The fluid motion in the bulk of the tank was modelled with sufficient accuracy using the coarse grid 1, however.

Time Marching The most appropriate time marching scheme, in line with the CFX users guide [51] was found to be the second order scheme described in section 5.1. This scheme exhibited better conservation properties as well as considerable savings in required computational time. The timestep was controlled dynamically using the root means square Courant number, this approach was validated by monitoring the surge front progression of a collapsing water column [69] in a preliminary study. Systematic variation of the root mean square Courant number indicated that an upper limit of $C_{N,\ rms} \leq 0.3$ is acceptable. The difference between $C_{N,\ rms} \leq 0.3$ and $C_{N,\ rms} \leq 0.05$ as a timestep control criterion was less significant than the difference between grids. However, for stability reasons $C_{N,\ rms} \leq 0.2$ is recommended.

Laminar or Turbulent Flow? In line with the calculated Reynolds number it was found that the flow is appropriate for turbulence modelling. The pressure histories obtained with a turbulence model showed two transient phases followed by a transition to the steady state. Two turbulence models were used, a $k - \epsilon$ model as it is the most widely used turbulence model in industrial CFD, and the more advanced SSG Reynolds Stress model. The two models are based on different first principles. While the $k - \epsilon$ turbulence model did not affect the numerical robustness of the simulation, the SSG model was far more susceptible to spatial and temporal discretisation.

The results showed that while there are some differences between the turbulence models using a single velocity field, the multiphase solutions for the $k-\epsilon$ and SSG turbulence models match very well, with only minor observable differences. As the SSG turbulence model requires greater computational and operator effort with no discernable improvement in the obtained solution, it is concluded that the $k-\epsilon$ model is the most effective turbulence model for sloshing flows. However, given the continuing turbulence model research, a more suitable turbulence model for sloshing flows may yet be developed.

Fluid Models Section 7, after an exhaustive study of fluid models available determined a suitable combination for further sloshing simulations. Consistent with the physics of the sloshing problem outlined in section 2, the gaseous phase has to be modelled in a way reflecting the importance of compressibility. The liquid phase, meanwhile, showed no difference between

a compressible and incompressible model. Using the speed of sound as an indicator, it is found that water and air compare reasonably well to the properties of natural gas in its liquid and gaseous phases respectively.

The computational results indicate that a compressible flow model for the gaseous phase, air, is required while the water may be modelled as an incompressible fluid. At the experimental scale, some fluid properties affecting the sloshing flow, quantified by the non dimensional parameters in section 2.3.4, do not appear to be scaled correctly. This is a problem readily solved within CFD, as it is possible to specify bespoke fluids satisfying most, if not all, dynamic scaling criteria.

Numerical Precision The use of double numerical precision, as recommended by Anderson [50] and the MARNET best practice guide [48], resulted in considerably quicker convergence of the coefficient iterations and a reduction of numerical noise in the results. In addition, the numerical dissipation of mass and momentum was reduced to insignificant values using this higher precision setting. Despite the higher memory requirements, the computational time was reduced as the individual iterations converged more quickly. Therefore, it is recommended that all CFD simulations of sloshing flows are carried out using a double precision setting. The specification of single precision as the default setting in CFX-10 is by itself somewhat questionable.

8.3 Further Work

Despite this report containing a number of useful findings, some further work is required.

1. The current study investigated sway motion only, but pitch motions are required as well. This may be accomplished using a body force approach, or the turbomachinery function within CFX-10.

2. Finally, the present problem has been investigated using a multiphase fluid model, with better correlation of the pressure histories at the critical monitor points P6 and P9. The results are contained a follow-on report yet to be completed.

The present study has identified the most suitable combinations of models to use within the commercial CFD code CFX for the simulation of sloshing flows. Spatial and temporal independence of the solution was established. However, the obtained steady state pressure history does not agree sufficiently well with the experimental data in regions where the dynamic pressure is important.

Recent studies using a multiphase model, that is solving separate velocity fields for air and water, have provided a result that matches the experimental data in the steady state. The results of the current study were used to set all other parameters required for the simulation. Hence the conclusions of this study may be used for multiphase sloshing flow simulations as well. As the present research programme requires a number of further sloshing simulations, with different tank geometries and scales filled with LNG rather than the present water-air combination, the conclusions of this report will help to identify the combination of computational models giving the most faithful representation of the fluid flow with the smallest possible computational cost.

References

[1] Sir Horace Lamb. *Hydrodynamics*. Cambridge University Press, 1879.

[2] Munehiko Hinatsu. Experiments of two-phase flows for the joint research. In *Proceedings of SRI-TUHH mini-Workshop on Numerical Simulation of Two-Phase Flows*. National Maritime Research Institute & Technische Universität Hamburg-Harburg, NMRI, 2001.

[3] Douglas Mann, editor. *LNG Materials and Fluids*. Cryogenics Division, National Bureau of Standards, 1977.

[4] James T Jensen. LNG and pipeline economics. In *The Geopolitics of Gas Meeting*, 2002.

[5] Roger Ffooks. *Natural Gas by Sea: The Development of a new Technology*. Witherby, 1993.

[6] Lloyd's Register to class world's largest LNG ships. *Oil Online*, 24 April 2006.

[7] Harry Benford and William A Fox, editors. *A Half Century of Maritime Technology*. Society of Naval Architects and Marine Engineers, 1993.

[8] Junshiro Ishimaru, Kiyokazu Kawabata, Hidetoshi Morita, Hidefumi Ikkai, and Yoshihiro Suetake. Building of advanced large sized membrane type LNG carrier. *Mitsubishi Heavy Industries Technical Review*, 41:1–7, 2004.

[9] H Norman Abramson, R L Bass, Odd M Faltinsen, and H A Olsen. Liquid slosh in LNG carriers. In *10th Symposium on Naval Hydrodynamics*, 1974.

[10] The future's a gas. *The Economist*, pages 53–54, 26 August 2004.

[11] Nervous energy. *The Economist*, pages 63–65, 7 January 2006.

[12] Department of Trade and Industry, HM Government. *Energy White Paper. Our Energy Future-Creating a Low Carbon Economy*.

[13] Floyd Norris. Off the charts: Weathering gas price volatility, 10 March 2006.

[14] E W Graham and A M Rodriguez. The characteristics of fuel motion which affect airplane dynamics. *Journal of Applied Mechanics*, September:381–388, 1952.

[15] H Norman Abramson. The dynamic behavior of liquids in moving containers, with applications to space vehicle technology. Technical Report SP-106, National Aeronautics and Space Administration, 1966.

[16] Odd M Faltinsen. A nonlinear theory of sloshing in rectangular tanks. *Journal of Ship Research*, 18:224–241, 1974.

[17] Odd M Faltinsen and Alexander N Timokha. An adaptive multimodal approach to nonlinear sloshing in a rectangular tank. *Journal of Fluid Mechanics*, 432:167–200, 2001.

[18] Raouf A Ibrahim. *Liquid Sloshing Dynamics*. Cambridge University Press, 2005.

[19] Raouf A Ibrahim and V N Pilipchuk. Recent advances in liquid sloshing dynamics. *Applied Mechanics Review*, 54:133–199, 2001.

[20] Stuart Brewer. Research and development new research into LNG tank sloshing. *Classification News*, 1:6–7, 2004. Det Norske Veritas Corporate Publication.

[21] Dolly Robinson. Horizons. Lloyds Register, December 2004. LR Newsletter.

[22] American Bureau of Shipping. Dynamic strength analysis of membrane type LNG containment system due to sloshing impact load. Technical report, American Bureau of Shipping, 2004.

[23] Ould El Moctar. Assessment for tankers. *Shipping World and Shipbuilder*, 204:28–31, 2006.

[24] G Gaillarde, A Ledoux, and M Lynch. Coupling between LNG and vessels motion for partially filled tanks: Effect on seakeeping. In *Royal Institution of Naval Architects: Design and Operation of Gas Carriers*, 2004.

[25] Yonghwan Kim. Coupled analysis of ship motions and sloshing flows. Technical report, American Bureau of Shipping, 2001.

[26] Philip J Aston. Modelling chaotic motion of a sloshing liquid in a horizontally forced axisymmetric container with a forced spherical pendulum. *Vehicle System Dynamics*, 40:121–141, 2004.

[27] X Kang, S Rakheja, and I Stiharu. Effects of tank shape on the roll dynamic response of a partly filled tank vehicle. *Vehicle System Dynamics*, 35:75–102, 2000.

[28] Tapping the gas market. *Marine Engineers Review*, pages 26–28, March 2002.

[29] Odd M Faltinsen, Olav F Rognebakke, and Alexander N Timokha. Resonant three-dimensional nonlinear sloshing in a square-base basin. *Journal of Fluid Mechanics*, 487:1–42, 2003.

[30] Odd M Faltinsen, Olav F Rognebakke, and Alexander N Timokha. Resonant three-dimensional nonlinear sloshing in a square-base basin. part 2. effect of higher modes. *Journal of Fluid Mechanics*, 523:199–218, 2005.

[31] Maurizio Landrini. Strongly nonlinear phenomena in ship hydrodynamics. *Journal of Ship Research*, 50:99–119, 2006.

[32] P A Cox, E B Bowles, and R L Bass. Evaluation of liquid dynamic loads in slack LNG cargo tanks. Technical Report 297, Ship Structure Committee, 1980.

[33] N A Hamlin. Liquid sloshing in cargo tanks. SSC 336, Ship Structure Committee, 1990.

[34] Harald Olsen. What is sloshing? In *Seminar on Liquid Sloshing*. Det Norske Veritas, 1976.

[35] A R J M Lloyd. *Seakeeping: Ship Behaviour in Rough Weather*. Ellis Horwood, Chichester, 1989.

[36] R L Bass, Jr E B Bowles, R W Trundell, J Navickas, J C Peck, N Yoshimura, S Endo, and B F M Pots. Modelling criteria for scaled LNG sloshing experiments. *Transactions of the American Society of Mechanical Engineers*, 107:272–280, 1985.

[37] Odd M. Faltinsen and Alexander N. Timokha. Asymptotic modal approximation of nonlinear resonant sloshing in a rectangular tank with small fluid depth. *Journal of Fluid Mechanics*, 470:319–357, 2002.

[38] Harald Olsen. Local impact pressures in basically prismatic tanks. In *Seminar on Liquid Sloshing*. Det Norske Veritas, 1976.

[39] Odd M Faltinsen and Olav F Rognebakke. Sloshing. In *NAV2000: International Conference on Ship and Ship Research, Venice*, 2000.

[40] Philippe Corrignan. *Analyse Physique des Phenomenes Associes au Ballottement de Liquide dans des Reservoirs (Sloshing)*. PhD thesis, Universite de Nantes, 1994.

[41] Robert L Bass, E B Bowles, and P A Cox. Liquid dynamic loads in LNG cargo tanks. *SNAME Transactions*, 88:103–126, 1980.

[42] Joel Escobedo and G Ali Mansoori. Surface tension prediction for pure fluids. *AIChE Journal*, 42(5):1425–1433, May 1996.

[43] Joseph J Cuneo, George A Gilmore, and Edmund G Tornay. Service experience with 125 000 m LNG vessels of spherical tank design. *SNAME Transactions*, 88:127–150, 1981.

[44] J M Chauvin. Membrane tank LNG carriers. *Revue de l'Institut Francais du Petrole*, 51:691–710, 1996.

[45] Henri Jean-Pierre Morand and Roger Ohayon. *Fluid Structure Interaction*. John Wiley and Sons, 1995.

[46] Odd M Faltinsen. A numerical nonlinear method of sloshing in tanks with 2D flow. *Journal of Ship Research*, 22:193–202, 1978.

[47] C J Lea. Guidance for NSD on the assessment of CFD simulations in safety cases. Technical report, Health and Safety Laboratory, HM Government Health and Safety Executive, 2003.

[48] WS Atkins Consultants. MARNET best practice guidelines for marine applications of computational fluid dynamics. Technical report, MARNET, 2003.

[49] Charles Hirsch. *Numerical Computation of Internal and External Flows. Vol 1: Fundamentals of Numerical Discretisation*. John Wiley and Sons, 1988.

[50] John D Anderson, Jr. *Computational Fluid Dynamics: The Basics with Applications*. McGraw Hill, Inc., 1995.

[51] Ansys Inc. *CFX-10 User's Guide*, 2005.

[52] J H Ferziger and M Peric. *Computational Methods for Fluid Dynamics*. Axel-Springer Verlag, 2002.

[53] H K Versteeg and W Malalasekera. *An Introduction to Computational Fluid Dynamics: The Finite Volume Method*. Prentice Hall, 1995.

[54] Stephen B Pope. *Turbulent Flows*. Cambridge University Press, 2000.

[55] David C Wilcox. *Turbulence Modelling for CFD*. DCW Industries, 1998.

[56] W G Price and Y G Chen. A simulation of free surface waves for incompressible two-phase flows using a curvilinear level set formulation. *International Journal for Numerical Methods in Fluids*, 51:305–330, 2006.

[57] I Hadzic, Frank Mallon, and M Peric. Numerical simulation of sloshing. Technical report, Technische Universität Hamburg-Harburg, 2002.

[58] R G Standing, S Amaratunga, F Lopez-Calleja, S Orme, and R Eichaker. Marine hydrodynamics modelling using CFD. In *CFD 2003: Computational Fluid Dynamics Technology in Ship Hydrodynamics*, 2003.

[59] Shin Hyung Rhee. Unstructured grid based Reynolds-Averaged Navier-Stokes method for liquid tank sloshing. *Transactions of the American Society of Mechanical Engineers*, 127:572–582, 2005.

[60] QNET CFD. Turbulence modelling: Part 2: Limitations of k-epsilon model. In *QNET CFD*, 2002.

[61] Charles G Speziale, Sutanu Sarkar, and Thomas B Gatsi. Modelling the pressure-strain correlation of turbulence: An invariant dynamical systems approach. *Journal of Fluid Mechanics*, 227:245–272, 1991.

[62] Joe F Thompson, Bharat K Soni, and Nigel P Weatherill, editors. *Handbook of Grid Generation*. CRC Press, 1999.

[63] P J Roache. Quantification of uncertainty in computational fluid dynamics. *Annual Review of Fluid Mechanics*, 29:123–160, 1997.

[64] Steven H Strogatz. *Nonlinear Dynamics and Chaos*. Perseus Book Publishing, 1994.

[65] F R Menter. Turbulence modelling for turbomachinery. *QNET - CFD Network Newsletter*, 2:10–13, 2003.

[66] Shahrouz Aliabadi, Andrew Johnson, and Jalal Abedi. Comparison of finite element and pendulum models for simulation of sloshing. *Computers and Fluids*, 32:535–545, 2003.

[67] C W Hirt and B D Nichols. Volume of fluid (VOF) method for the dynamics of free boundaries. *Journal of Computational Physics*, 39:201–225, 1981.

[68] Rik Wemmenhove, Erwin Loots, Roel Luppes, and Arthur E P Veldman. Modelling two-phase flow with offshore applications. In *24th International Conference on Offshore Mechanics and Arctic Engineering*, 2005.

[69] J C Martin and W J Moyce. An experimental study of the collapse of liquid columns on a rigid horizontal plane. *Philosophical Transactions of the Royal Society of London. Series A, Mathematical and Physical Sciences*, 244:312–324, 1952.

Appendices

Appendix A: CFX Screenshots

A CFX-10.0 Screenshots

A.1 Preprocessor

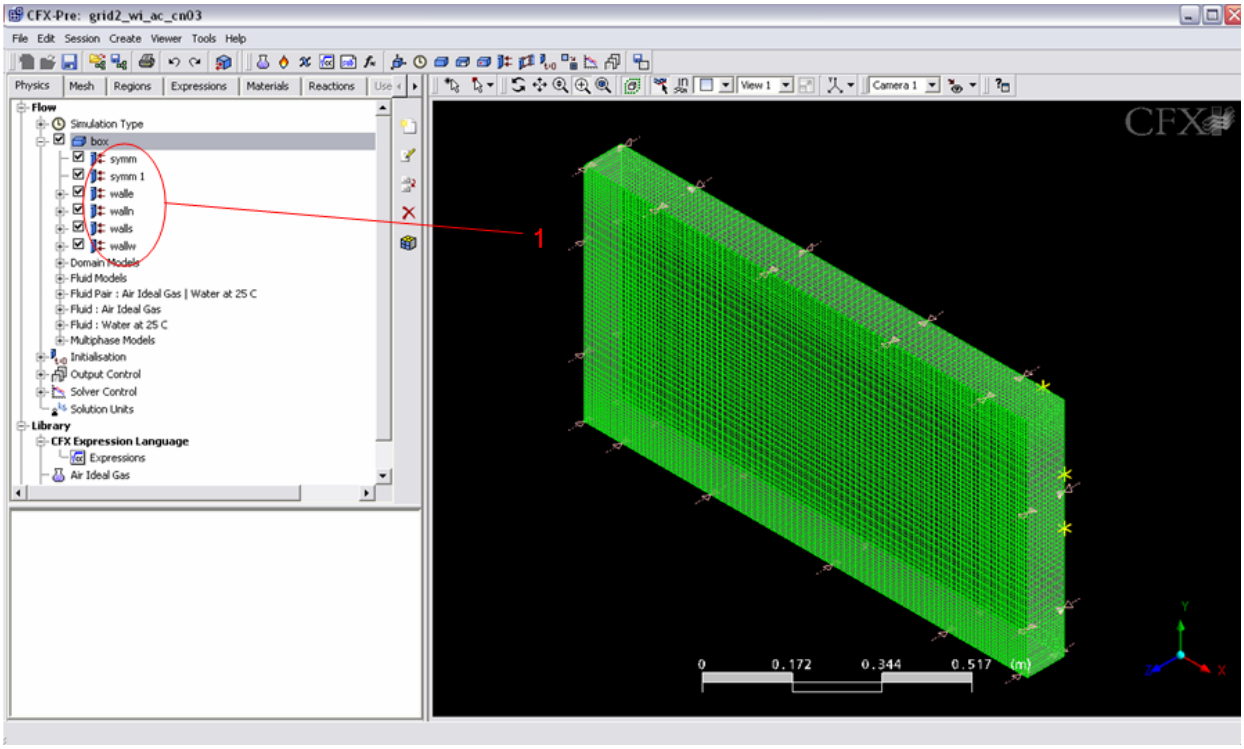

Figure A.1: CFX-10.0 Preprocessor Main Window. (1) indicates the surfaces of the grid loaded form ICEM. The surface names must be identified in ICEM.

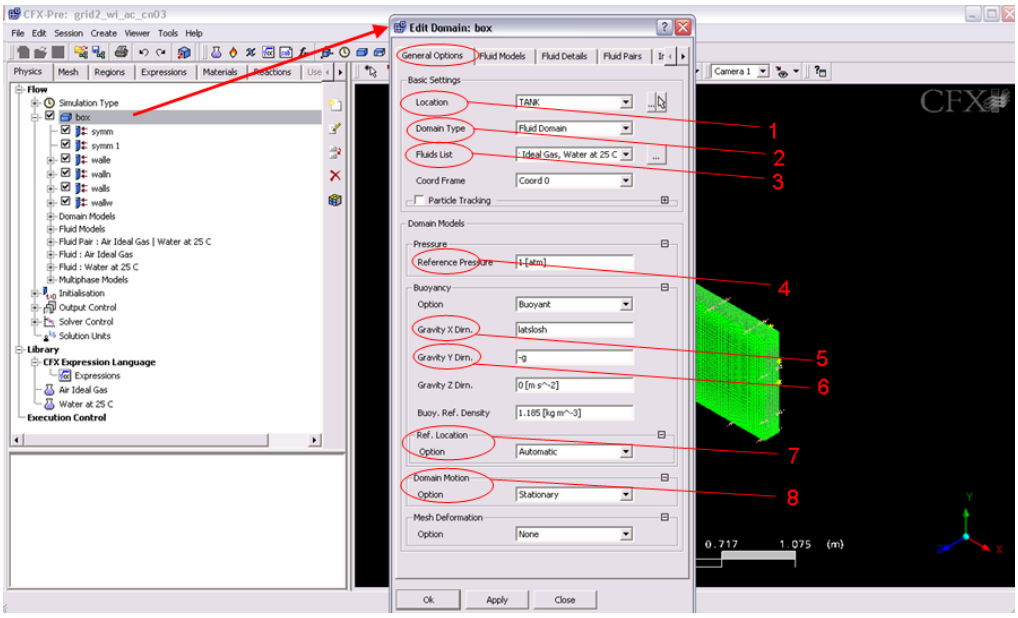

A.2(a): **Flow Physics Setup.** (1) defines the part of the mesh all subsequent definitions are applied to. (2) specifies the type of domain, for typical fluid dynamics problems, 'Fluid Domain' is appropriate. (3) defines all fluids (standard CFX library or custom fluids) to be included in the simulation. (4) sets the reference pressure. (5) defines the acceleration in the x direction: the oscillating body force for sloshing. (6) sets the acceleration in the y direction: gravity. (7) defines a location where the reference pressure is defined. (8) defines the domain motion, which is not required for the current problem but may be used to simulate pitching motion

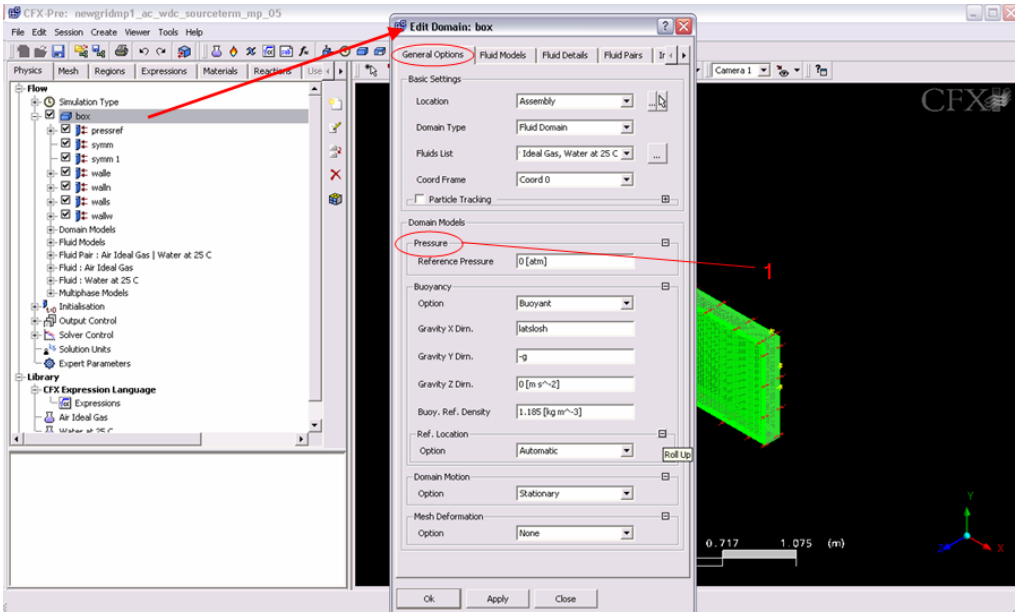

A.2(b): **Flow Physics Setup for Multiphase Flow.** As the pressure is specified using an outlet node the reference pressure, (1) is set to zero.

Figure A.2: CFX-10.0 Preprocessor flow physics setup

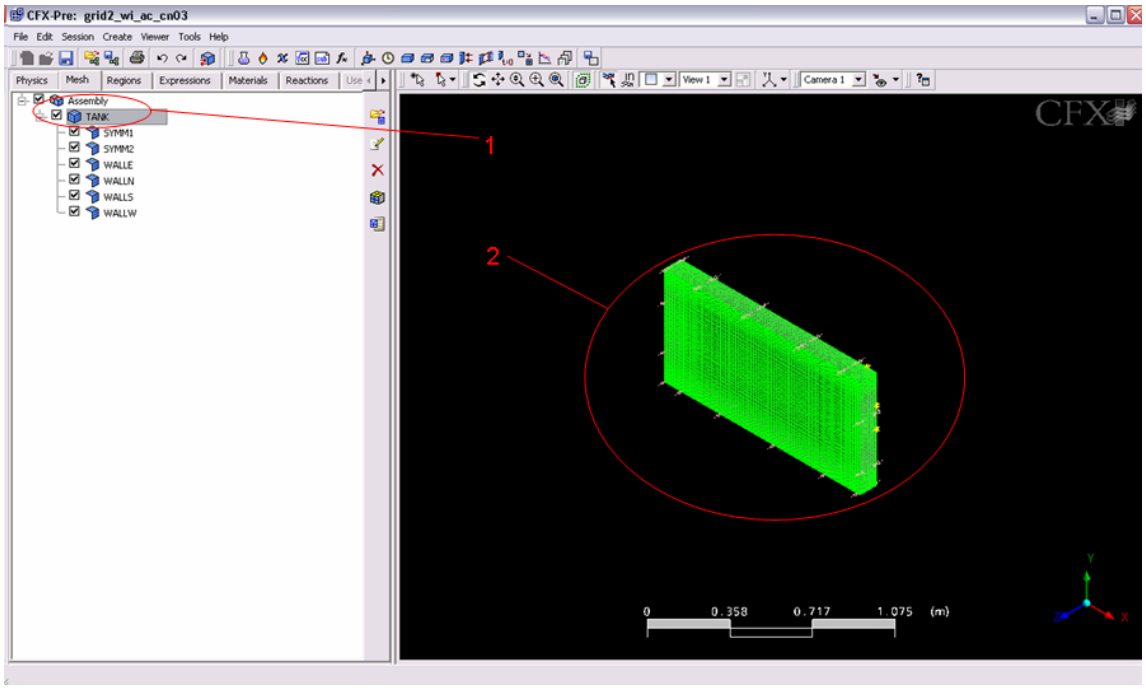

A.3(a): **Mesh Input Function.** (1) the mesh *Tank* is loaded into the preprocessor. (2) view of the mesh as read by CFX

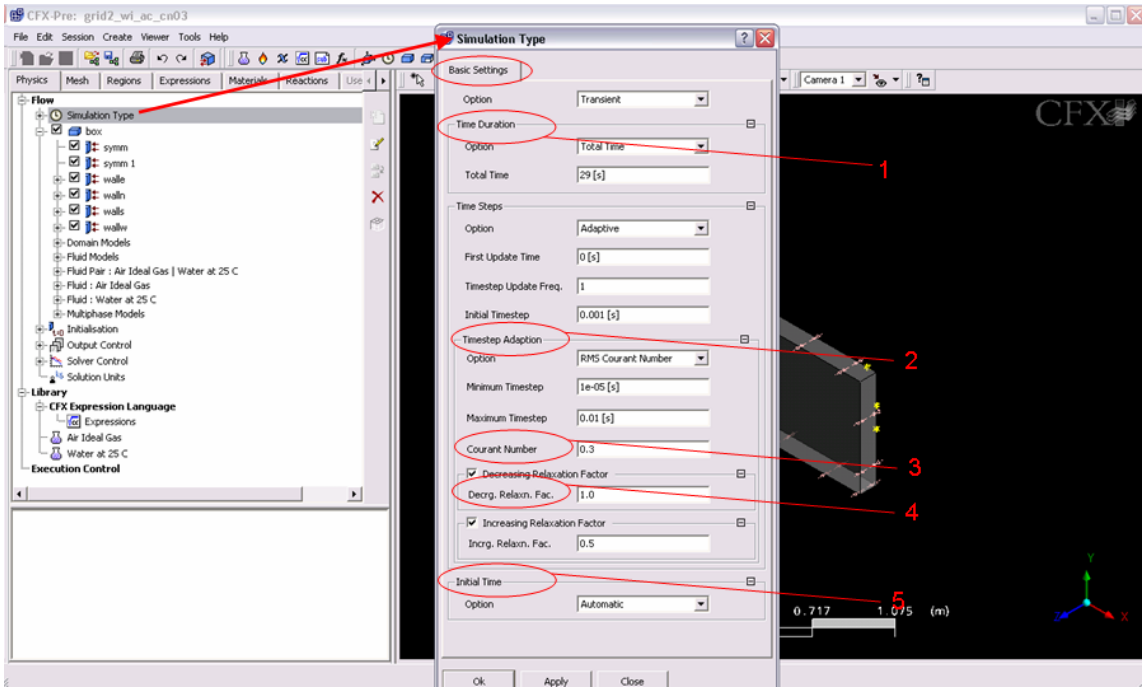

A.3(b): **Simulation Type Definition.** This window defines whether a simulation is transient or steady-state. (1) sets the total simulated time. (2) defines a timestep adaptation scheme (if chosen), in the current case a Courant number, set at (3) is specified. (4) the decreasing and increasing relaxation factors define how quickly the timestep adapts to a changing control parameter. (5) the initial time is set to continue from a previous run, normally a run would start at $t = 0$.

Figure A.3: CFX-10.0 Preprocessor run definition

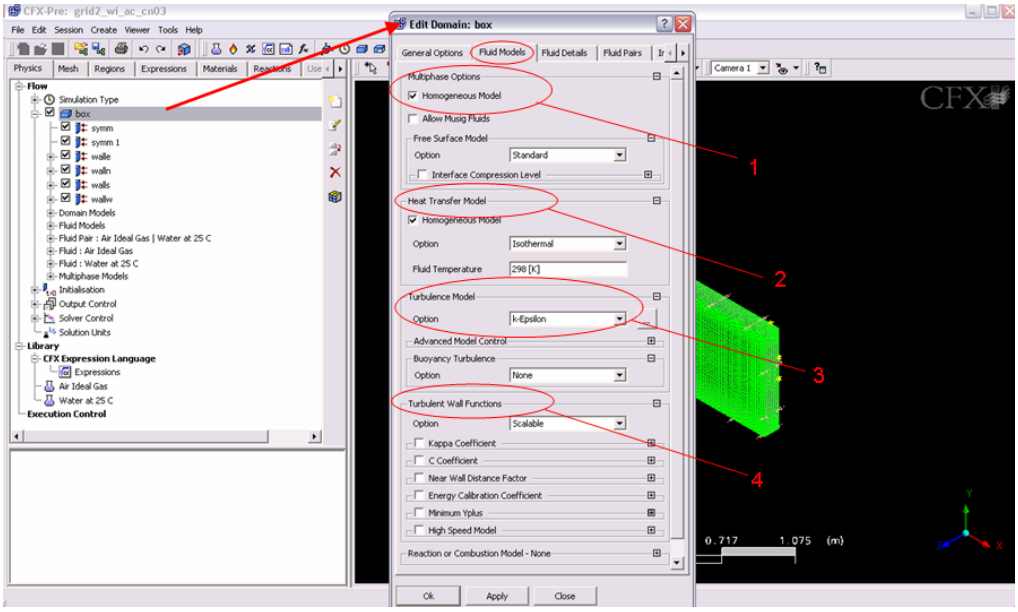

A.4(a): **Fluid Model Definition.** This set of options defines the types of fluids to be included in the simulation. Deselecting the option 'Homogeneous Model' at (1) will result in multiphase simulation if more than one fluid is selected in figure A.2(a). The current case simulates two fluids with a shared velocity field. (2) sets the thermodynamic aspects of the simulation. (3) defines the turbulence model for the simulation, in conjunction with (4) where the scalable wall functions may be edited

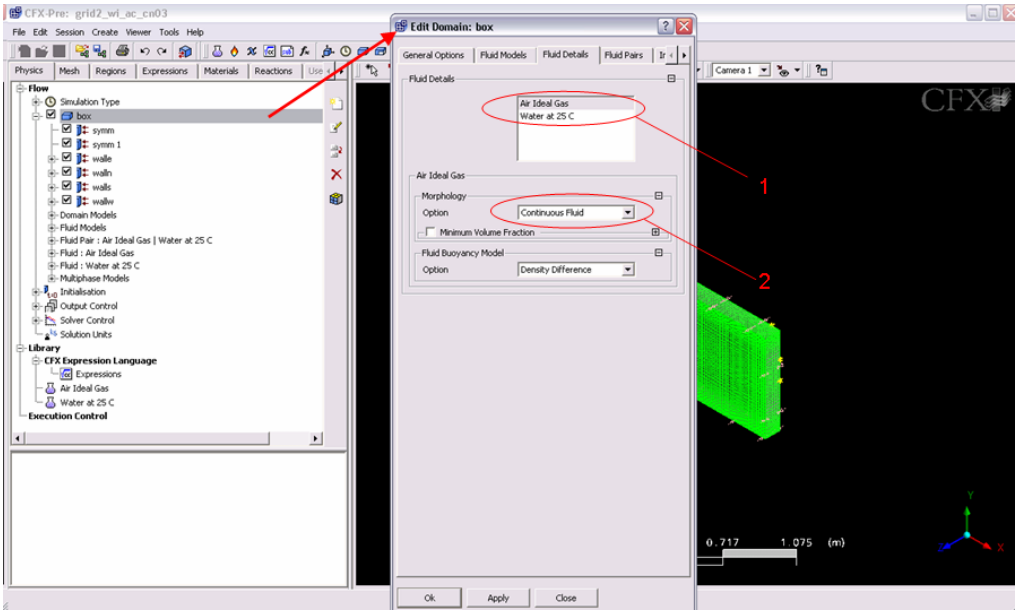

A.4(b): **Fluid Details.** Further fluid properties are defined in this tab. (1)selects the fluid and (2) the type of fluid morphology. It was found that setting water and air as dispersed and continuous fluids respectively improves the computational stability of violent sloshing.

Figure A.4: CFX-10.0 Preprocessor fluid definition

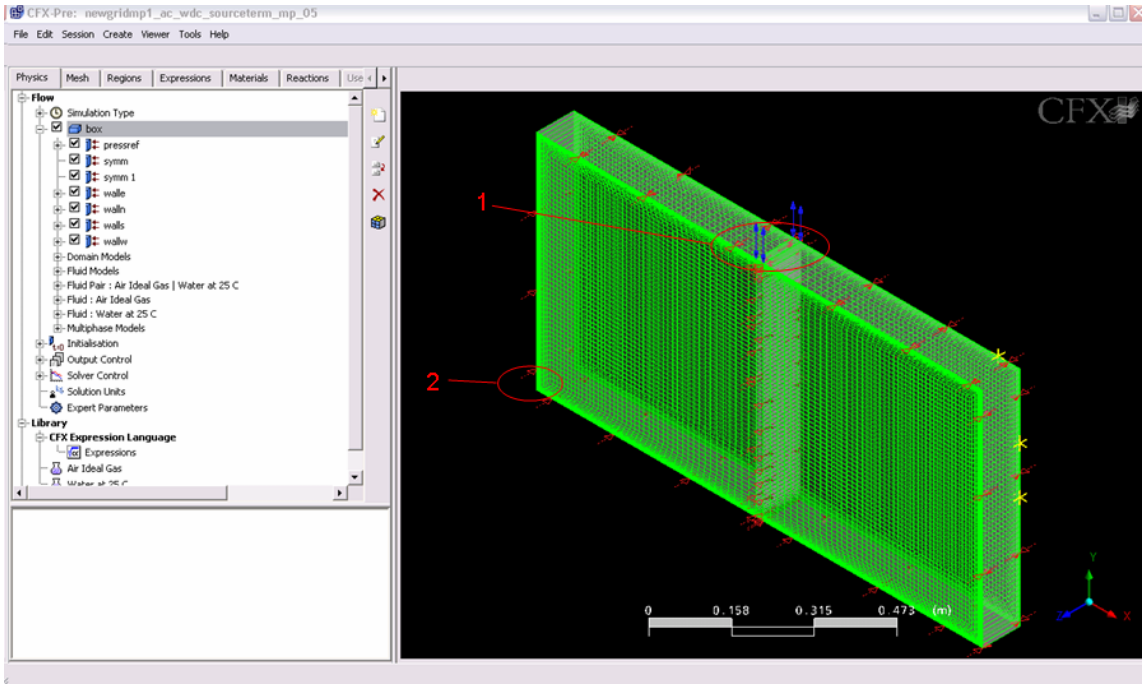

A.5(a): **Multiphase Flow Setup.** Here the window analogous to the single phase flow in figure A.2(a) is shown for multiphase flow. Note the outflow node set at (1) and the grid structure with a greater number of cells near the tank wall in (2)

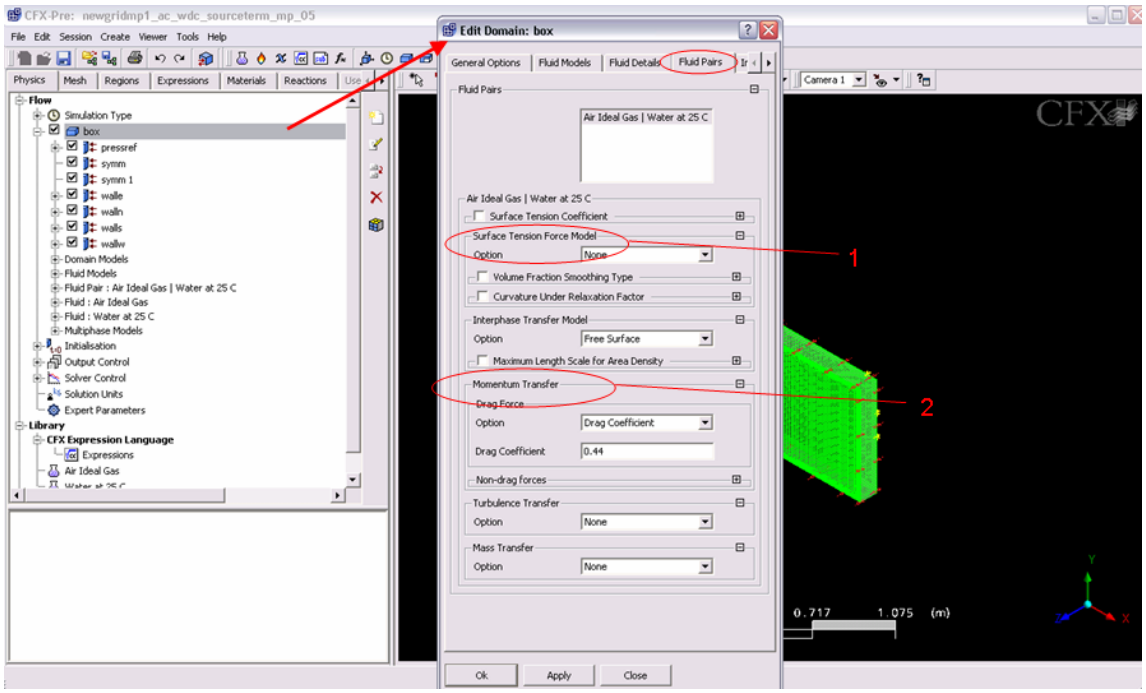

A.5(b): **Fluid Pair Options.** For a multiphase simulation, the 'fluid pairs' window offers significantly more options. Note that at (1) no surface tension model was selected and the momentum transfer option at (2) was found to be the computationally most stable.

Figure A.5: CFX-10.0 Preprocessor multiphase setup

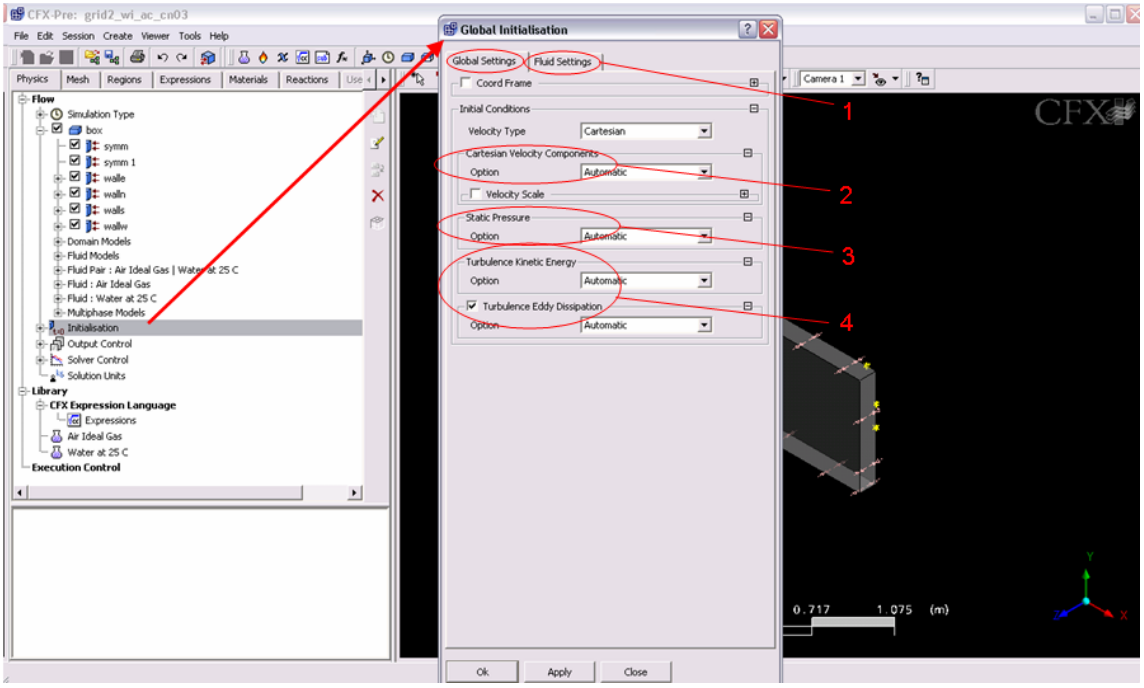

A.6(a): **Flow Initialisation.** The boundary and initial conditions are set in this dialog box. 'Fluid Settings' at (1) sets fluid-specific options - the volume fractions, and velocity fields for a multiphase flow - while all domain-wide settings are defined in 'Global Settings'. (2) specifies the velocity field in cartesian components and (3) the static fluid pressure. (4) offers a bespoke initialisation of the turbulence model if required.

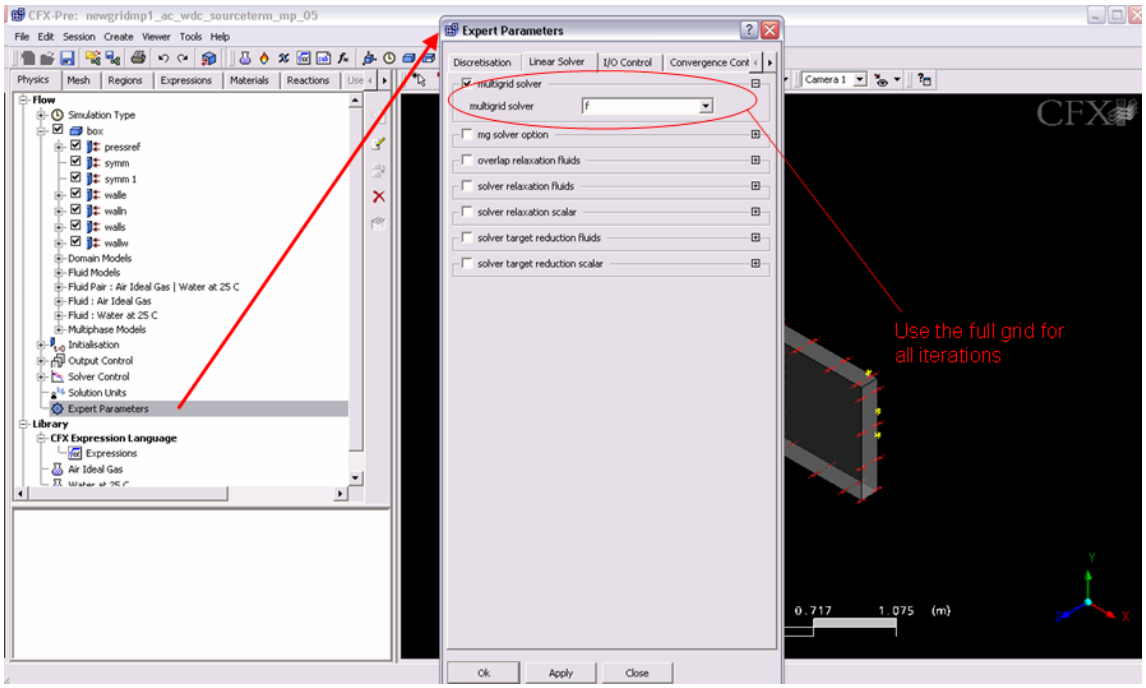

A.6(b): **Expert Parameters.** The only expert parameter altered for sloshing was to turn off the multigrid solver as it negatively affects the stability of the computation.

Figure A.6: CFX-10.0 Preprocessor preparation

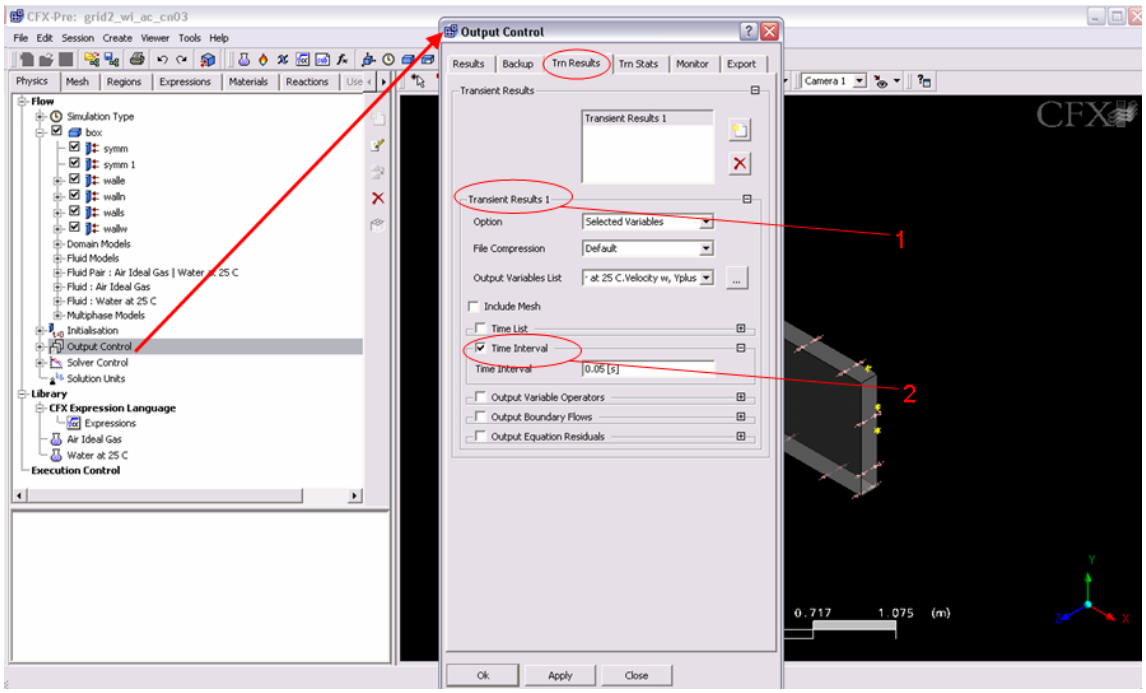

A.7(a): **Output Control.** CFX gives a full result at the end of a run, intermediate results including only variables of interest are defined in 'Trn Results'. the variables to be saved are specified in (1) and the output interval, defined by simulated time or iteration, is set in (2).

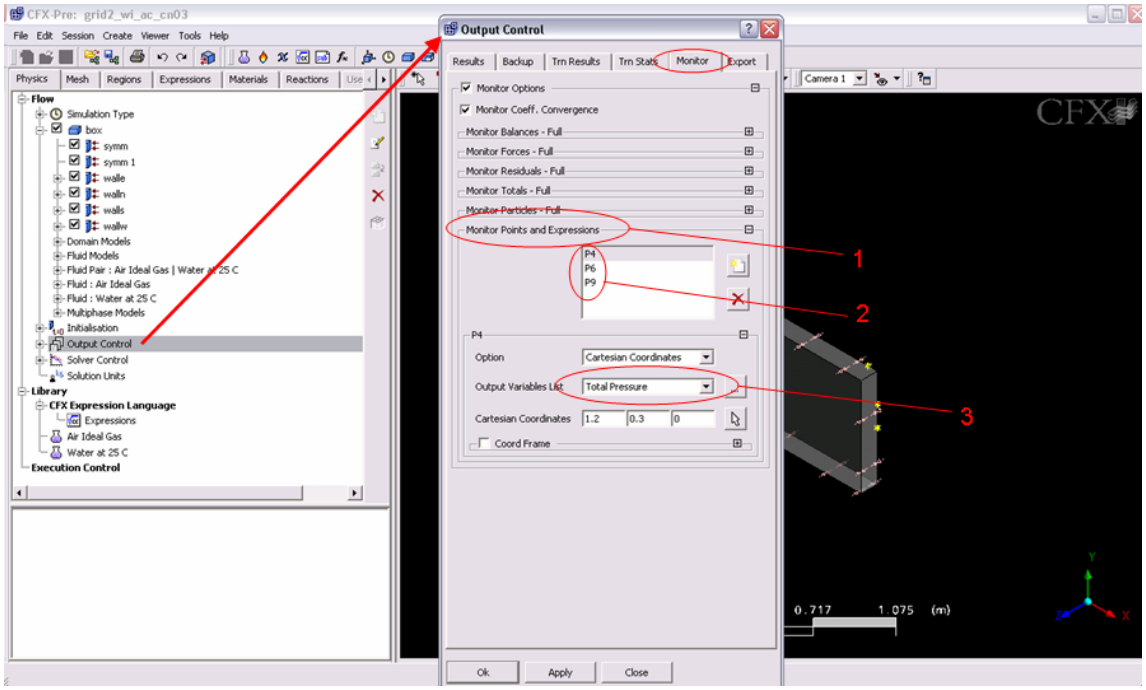

A.7(b): **Monitor Points.** Global and local solution properties can be monitored throughout a run using variables within CFX or custom functions. Heading (1) is the main definition window for monitor points. The user-created monitor points in (2) are then adapted using the menu in (3)

Figure A.7: CFX-10.0 Preprocessor output control

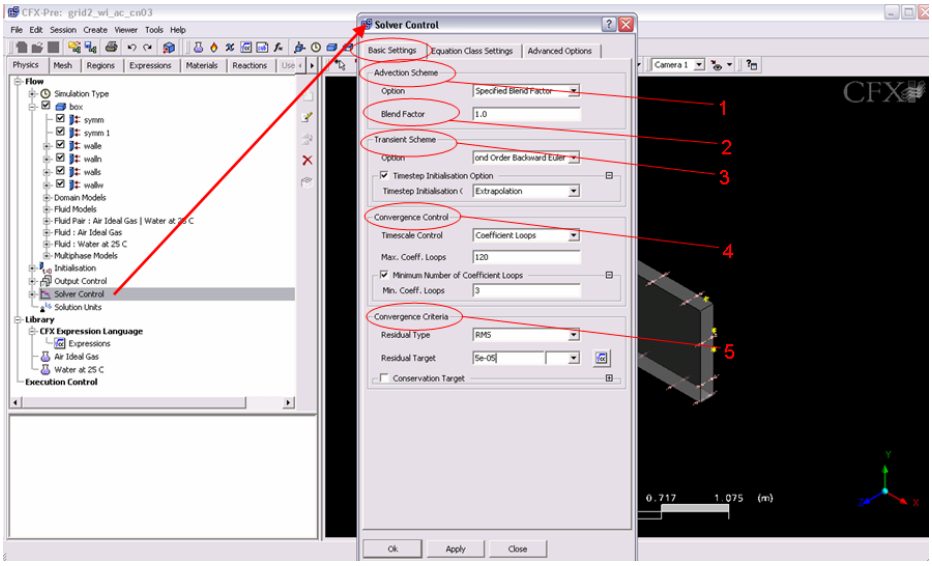

A.8(a): **Solver Control.** The numerical solver control is carried out using the window above. (1) specifies the type of advection scheme or spatial discretisation - first order upwind, high resolution or specified blend factor - as appropriate for the type of simulation, see section 4.1 for a discussion. As the current spatial discretisation scheme is 'Specified Blend Factor', the value is entered at (2). (3) defines the transient scheme, for a discussion of different methods, the reader is referred to section 5. (4) sets the convergence control - maximum time or coefficient loops - as well as a minimum number of iterations to be carried out if the error threshold defined in (5) is met.

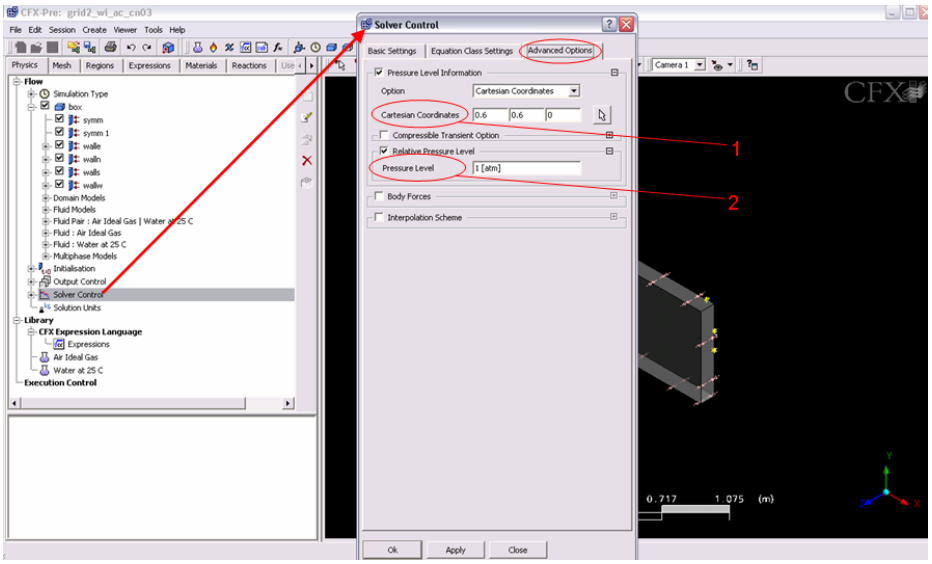

A.8(b): **Advanced Solver Control.** The 'Advanced options' tab is used to specify the reference pressure. (1) defines the location and the pressure is entered in (2). Note that the solver precision - single or double - may be entered using the execution control option at the lower left-hand corner of figure A.8(b) as well as in the solver control window.

Figure A.8: CFX-10.0 Preprocessor execution control

A.2 Solver Monitor

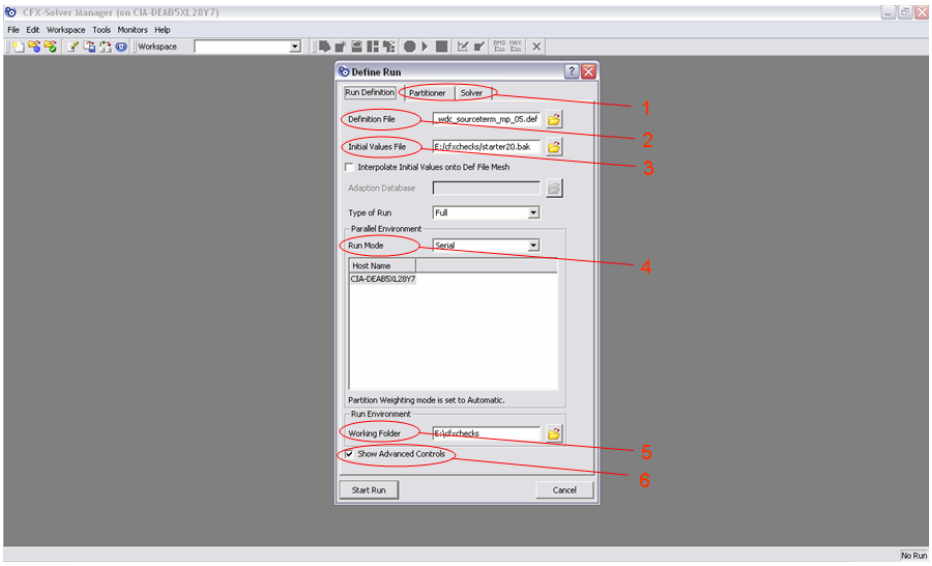

A.9(a): **Solver Definition.** The definition file, obtained from the solver is shown in (2) and the initial values file - if a run is continued, or interpolated onto a finer grid - is shown in (3). (4) shows the run mode, either serial or parallel. The working directory is defined in (5). The 'Advanced Options' box in (6) needs to be checked to display the further option tabs shown at (1).

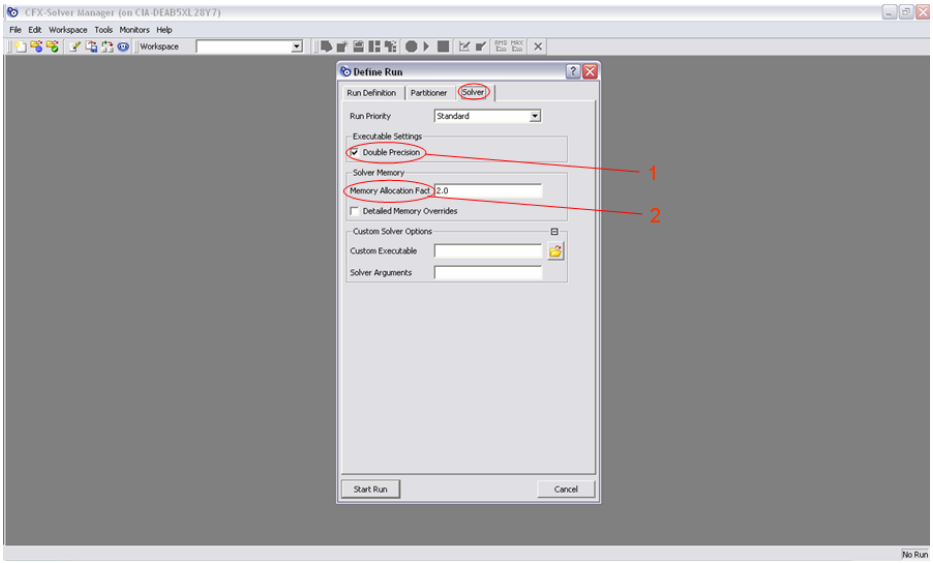

A.9(b): **Advanced Solver Definition.** This tab is useful as the solver precision - single or double - is specified at (1). Note that CFX uses single precision as the default setting. The memory allocation factor, defined in (2) may be required to be greater than the default value of 1.0 when simulating a large number of time steps.

Figure A.9: CFX-10.0 Solver manager initialisation screenshots

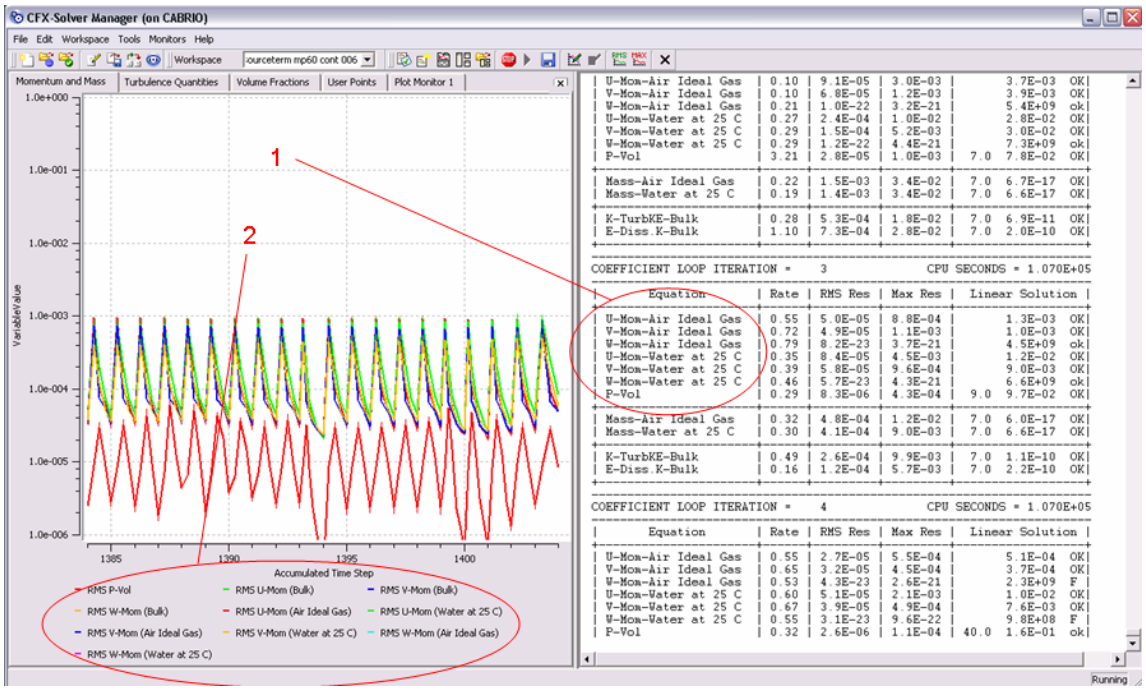

A.10(a): **Run in Progress.** (1) shows the numerical results of each iteration, the information is saved to an output file as well. The solver performance is also shown in graphical format where the residuals are indicated in (2). This function is available for all variables solved in the simulation.

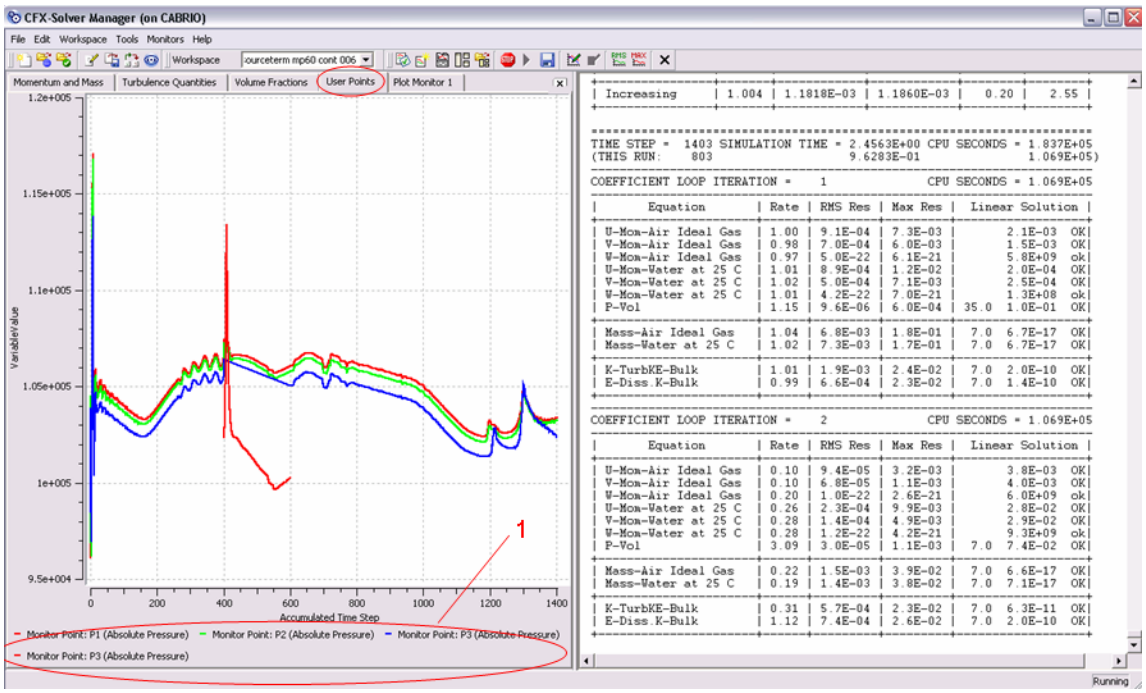

A.10(b): **Monitor Points.** The monitor points are shown as well when selecting the appropriate tab. (1) indicates the colour coding, note that the monitor points may be shown in terms of elapsed simulation time rather than time step.

Figure A.10: CFX-10.0 Solver manager screenshots

A.3 Postprocessor

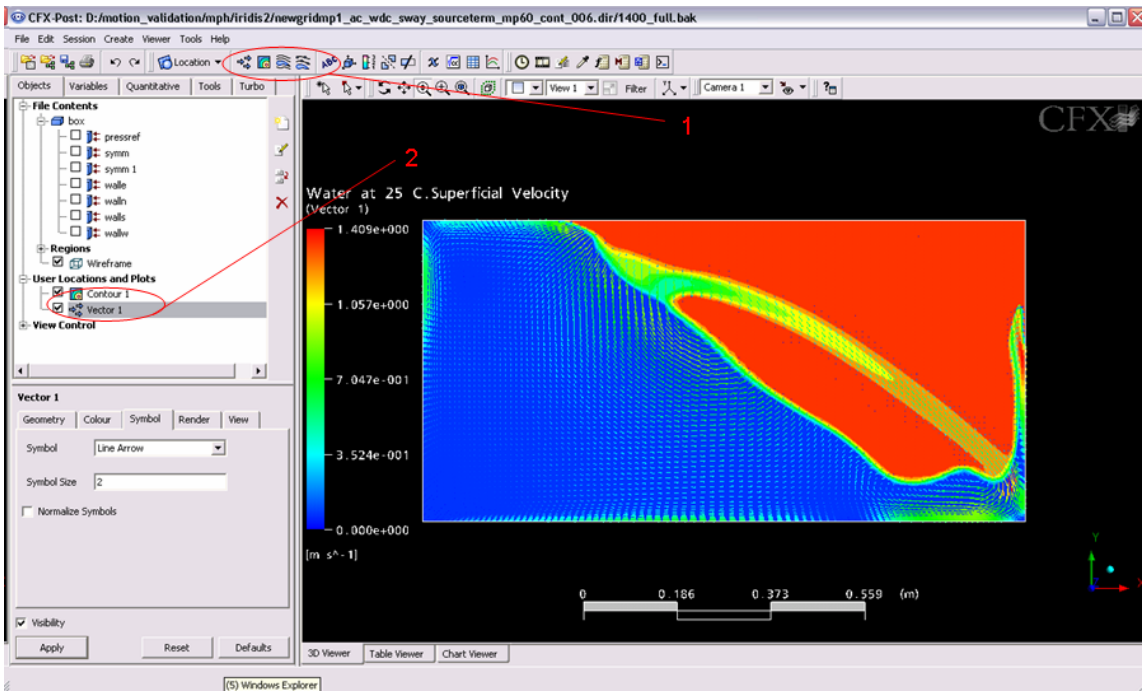

Figure A.11: CFX-10.0 Postprocessor screenshots. The postprocessor offers a multitude of plotting options, the most useful are indicated by (1). Once a plot has been created it is shown in (2). Transient runs are best analysed using the probe tool and CFX power syntax explained in the CFX Users Guide [51].